

Alma Mater Studiorum – Università di Bologna

DOTTORATO DI RICERCA IN

Ingegneria Biomedica, Elettrica e dei Sistemi

Ciclo 33°

Settore Concorsuale: 09/E4

Settore Scientifico Disciplinare: ING-INF/07

TITOLO TESI

Design and Implementation of New Measurement Models and
Procedures for Characterization and Diagnosis of Electrical Assets

Presentata da: Abbas Ghaderi

Coordinatore Dottorato

Prof. Michele Monaci

Supervisore

Prof. Lorenzo Peretto

Esame finale anno 2021

Abstract

The measurement is an essential procedure in power networks for both network stability, and diagnosis purposes. This work is an effort to confront the challenges in power networks using metrological approach. In this work three different research projects are carried out on Medium Voltage underground cable joints diagnosis, inductive Current Transformers modeling, and frequency modeling of the Low power Voltage Transformer as an example of measurement units in power networks. For the cable joints, the causes and effects of Loss Factor has been analyzed, while for the inductive current transformers a measurement model is developed for prediction of the ratio and phase error. Moreover, a frequency modeling approach has been introduced and tested on low power voltage transformers. The performance of the model on prediction of the low power voltage transformer output has been simulated and validated by experimental tests performed in the lab.

Keywords: Measurement Setup, Power Network, Cable Joint, Current Transformer, Low Power Voltage Transformer

Contents

1	Introduction	1
2	Power systems and measurement	3
2.1	Instrument Transformers in Power Systems.....	5
2.1.1	Inductive CTs and VTs in power networks	6
2.1.2	Low Power Instrument Transformers	8
2.2	Measurement for diagnosis in power systems	10
3	Definitions in Metrology	11
3.1	Metrology and Measurement.....	11
3.2	Uncertainty in Measurement	13
3.3	Calibration	13
3.4	Calibration Hierarchy	14
3.5	Verification.....	14
3.6	Validation	15
3.7	Metrological Traceability	15
3.8	Calibration Process	15
3.8.1	Instrument Transformers Calibration	16
3.8.2	Instrument Transformer Calibration using Calibrator Devices	17
3.8.3	Measurement setup calibration	18
4	Measurement for MV Cable Joints Diagnosis.....	19
4.1	Test Setup Design, and Calibration for Tan Delta Measurements on MV Cable Joints	20
4.1.1	Cable joint description.....	20
4.1.2	Test Setup Design.....	21
4.1.3	Sample Preparation.....	23
4.1.4	Tan Delta Measurement Technique.....	24
4.1.5	Tan Delta Measurement Results.....	28
4.1.6	Conclusions	29
4.2	Effects of Temperature on MV Cable Joints Tan Delta Measurements	29
4.2.1	Sample Preparation.....	29
4.2.2	Measurement Procedure	30
4.2.3	Measurement Results.....	31
4.2.4	Conclusions	34

4.3	Effects of Mechanical Pressure on the Tangent Delta of MV Cable Joints	35
4.3.1	Test Setup Description.....	35
4.3.2	Test procedure	36
4.3.3	Test Results	38
4.3.4	Conclusions	39
4.4	Test Bed Characterization for the Interfacial Pressure vs. Thermal cycle Measurements in MV Cable Joints	40
4.4.1	Measurement Setup	41
4.4.2	Description of the Experimental Tests	46
4.4.3	Results and Discussion	47
4.4.4	Conclusion.....	51
5	Measurement Model for Inductive Current Transformers.....	53
5.1	Inductive Current Transformer Core Parameters Behaviour vs. Temperature Under Different Working Conditions.....	53
5.1.1	Test Setup	54
5.1.2	Experimental Tests Procedure	55
5.1.3	Tests Results	58
5.1.4	Conclusions	61
5.2	Procedure for Inductive Current Transformers error prediction at Different Operating Conditions.....	61
5.2.1	Test Setup	62
5.2.2	Experimental Tests and Analysis.....	63
5.2.3	Experimental tests and accuracy prediction results	66
5.2.4	Conclusions	70
6	Low-Power Voltage Transformer Smart Frequency Modeling and Output Prediction up to 2.5 kHz, Using Sinc-Response Approach.....	71
6.1	LPVT Model.....	72
6.2	IR Test Method vs. SR Test Method	74
6.2.1	IR Test Method.....	74
6.2.2	SR Test Method	75
6.3	Sinc Signal Design	76
6.3.1	Sinc Function Fourier-Transform Analysis	77
6.3.2	Sinc Function Characteristic.....	78
6.3.3	Sinc Function Fourier Series Coefficients.....	79
6.4	Experimental Test Setup.....	80
6.5	Experimental Tests	81
6.5.1	SR Test Procedure	81

6.5.2	SF Test Procedure.....	82
6.5.3	DW Test Procedure	82
6.5.4	Output Prediction and Validation	82
6.6	Results	85
6.6.1	SR Experimental Test Results	85
6.6.2	Transfer Functions.....	87
6.6.3	SF Experimental Test Results.....	89
6.6.4	DW Experimental Test Results	90
6.6.5	Output Prediction and Validation	91
6.7	Conclusion.....	94
7	Conclusions	95
8	References	97

LIST OF FIGURES

FIGURE 2-1. FROM LEFT TO RIGHT: MV INDUCTIVE CURRENT TRANSFORMER FOR INDOOR APPLICATION, HV OIL-PAPER INSULATION INDUCTIVE CURRENT TRANSFORMER FOR OUTDOOR APPLICATION, HV COMBINED CURRENT AND VOLTAGE TRANSFORMER	7
FIGURE 2-2. FROM LEFT TO RIGHT: MV INDUCTIVE VOLTAGE TRANSFORMER FOR INDOOR APPLICATION, HV OIL-PAPER INSULATION VOLTAGE TRANSFORMER FOR OUTDOOR APPLICATION, HV CAPACITIVE VOLTAGE TRANSFORMER	8
FIGURE 2-3. FROM LEFT TO RIGHT: SPLIT CORE ROGOWSKI COIL LPCT, UNIFORM CORE ROGOWSKI COIL LPCT, MV COMBINED LPIT FOR INDOOR APPLICATION, MV COMBINED LPIT FOR OUTDOOR APPLICATION.....	9
FIGURE 2-4. FROM LEFT TO RIGHT: MV CAPACITIVE LPVT FOR OUTDOOR APPLICATION, MV CAPACITIVE LPVT FOR INDOOR APPLICATION, MV RESISTIVE LPVT	10
FIGURE 3-1. IT CALIBRATION TEST SETUP USING A TRACEABLE REFERENCE IT TO BE COMPARED WITH THE IT UNDER CALIBRATION.....	17
FIGURE 3-2. IT CALIBRATION TEST SETUP USING A TRACEABLE REFERENCE SIGNAL CALIBRATOR AND WITHOUT REFERENCE IT AND COMPARATOR	18
FIGURE 4-1. CABLE JOINT CROSS SECTION DESCRIPTION (COURTESY OF REPL ITALY).....	20
FIGURE 4-2. AUTOMATIC MEASUREMENT SETUP FOR THE TAN DELTA MEASUREMENT.....	22
FIGURE 4-3. EQUIVALENT ELECTRIC CIRCUIT OF THE PROPOSED SETUP.....	22
FIGURE 4-4. PICTURE OF THE CABLE JOINT UNDER TEST BEFORE AND AFTER ITS PREPARATION WITH ALUMINIUM FOILS	23
FIGURE 4-5. PICTURE FROM THE CABLE: 1, THE LONGEST INSULATOR PATH CONSIDERED, 2 AND 3 THE MINIMUM INSULATOR PATH USED FOR SURFACE DISCHARGE TEST	24
FIGURE 4-6. RIGHT: EQUIVALENT CIRCUIT OF A CABLE JOINT LEFT: DISSIPATION ANGLE REPRESENTED IN THE PHASORS PLANE	24
FIGURE 4-7. TAN DELTA MEASUREMENT ALGORITHM	27
FIGURE 4-8. VOLTAGE AND CURRENT PHASORS ACQUIRED FOR THE TAN DELTA MEASUREMENT.....	28
FIGURE 4-9. TAN DELTA VS. TEMPERATURE MEASUREMENT RESULTS FOR THE IN-FIELD CABLE JOINT.....	32
FIGURE 4-10. TAN DELTA VS. TEMPERATURE MEASUREMENT RESULTS FOR THE TG 100 CABLE JOINT.....	33
FIGURE 4-11. TAN DELTA VS. TEMPERATURE MEASUREMENT RESULTS FOR THE TG 150 CABLE JOINT.....	33
FIGURE 4-12. TAN DELTA VS. TEMPERATURE MEASUREMENT RESULTS FOR THE 3 CABLE JOINTS UNDER TEST AT 60 °C.....	34
FIGURE 4-13. PICTURE OF THE HOSE CLAMP USED TO APPLY PRESSURE TO THE CABLE JOINT UNDER TEST	36
FIGURE 4-14. PICTURE OF THE SIMULATED CABLE JOINT USING FINITE-ELEMENT SOFTWARE	37

FIGURE 4-15. ELECTRIC POTENTIAL DISTRIBUTION AND ELECTRIC FIELD COMPONENTS OF A SIMULATED CABLE JOINT.....	37
FIGURE 4-16. SCHEMATIC REPRESENTATION OF THE PRESSURE APPLICATION AND MEASUREMENT.....	38
FIGURE 4-17. TAN DELTA MEASUREMENT RESULTS FOR ALL THE THREE PRESSURE TESTS	39
FIGURE 4-18. CAUSE AND EFFECT LOOP FOR THE RELATION BETWEEN TAN DELTA, TEMPERATURE, AND INTERFACIAL PRESSURE IN CABLE JOINTS.....	40
FIGURE 4-19. SCHEMATIC OF THE MEASUREMENT SETUP AND PRESSURE SENSORS POSITIONING.....	42
FIGURE 4-20. CABLE JOINT STRUCTURE WITH PARTICULAR ATTENTION TO THE PARTS OF INTEREST.....	43
FIGURE 4-21. PICTURE OF THE ADOPTED PRESSURE SENSOR	45
FIGURE 4-22. TEMPERATURE VS. DURATION OF THE TESTS ON THE CUTS	47
FIGURE 4-23. POSITIONING OF THE TWO SENSORS INSIDE THE CUT AND OF THE CUT ITSELF.....	49
FIGURE 4-24. PRESSURE MEASUREMENT RESULTS FOR CUT A, SENSORS <i>A1</i> AND <i>A2</i>	49
FIGURE 4-25. PRESSURE MEASUREMENT RESULTS FOR CUT B, SENSORS <i>B1</i> AND <i>B2</i>	49
FIGURE 4-26. CAUSE AND EFFECT LOOP FOR THE RELATION BETWEEN TAN DELTA, TEMPERATURE, AND INTERFACIAL PRESSURE IN CABLE JOINTS.....	52
FIGURE 5-1. CIRCUIT DIAGRAM OF THE MEASUREMENT SETUP ADOPTED FOR THE TESTS.....	55
FIGURE 5-2. CIRCUIT DIAGRAM OF THE MEASUREMENT SETUP ADOPTED FOR THE SHORT CIRCUIT TESTS	56
FIGURE 5-3. CIRCUIT DIAGRAM OF THE MEASUREMENT SETUP ADOPTED FOR THE OPEN CIRCUIT TESTS	57
FIGURE 5-4. CIRCUIT DIAGRAM OF THE CT EQUIVALENT CIRCUIT CONSIDERED.....	58
FIGURE 5-5. SHUNT PARAMETERS REPRESENTATION VS. TEMPERATURE VS. APPLIED VOLTAGE	61
FIGURE 5-6. MEASUREMENT SETUP ADOPTED FOR THE RATED CONDITIONS TESTS	63
FIGURE 5-7. PART OF THE CT EQUIVALENT CIRCUIT DETAILING THE SHUNT PARAMETERS AND THE BURDEN.....	64
FIGURE 5-8. COMPLETE MODEL OF THE CT ADOPTED IN THE WORK.....	64
FIGURE 5-9. FUNCTIONS e_T AND e_C FOR THE RATIO ERROR PREDICTION.....	69
FIGURE 5-10. FUNCTIONS f_T AND f_C FOR THE PHASE DISPLACEMENT PREDICTION	69
FIGURE 6-1. LOW-POWER VOLTAGE TRANSFORMERS (LPVT) ELECTRIC EQUIVALENT CIRCUIT.....	73
FIGURE 6-2. DESIGNED NORMALIZED SINC SIGNAL. (A) TIME DOMAIN; (B) DISCRETE FOURIER TRANSFORM (DFT) MAGNITUDE	76
FIGURE 6-3. SAMPLING PRINCIPLE OF AN ARBITRARY SIGNAL.....	78
FIGURE 6-4. EXPERIMENTAL TEST SETUP SCHEME	80
FIGURE 6-5. (A) DFT MAGNITUDE OF THE INPUT SINC SIGNAL; (B) DFT MAGNITUDE OF THE SINC-RESPONSE SIGNAL; (C) RATIO BETWEEN DFT MAGNITUDE OF INPUT SINC AND SINC-RESPONSE SIGNAL	84

FIGURE 6-6. REFERENCE INPUT SINC SIGNAL APPLIED TO THE LPVT UNDER TEST, MEASURED BY REFERENCE RESISTIVE–CAPACITIVE VOLTAGE DIVIDER AND THE INPUT SINC SIGNAL MEASURED BY THE LPVT UNDER TEST (LPVT SINC-RESPONSE TRANSFERRED TO THE PRIMARY SIDE).....86

FIGURE 6-7. RATIO ERROR TREND VS. FREQUENCY86

FIGURE 6-8. PHASE DISPLACEMENT TREND VS. FREQUENCY87

FIGURE 6-9. TIME DOMAIN UNFILTERED VERSION OF THE LPVT SAMPLED DATA TRANSFER FUNCTION. (A) ALL 10,000 SAMPLES; (B) FIRST 9 SAMPLES; (C) ONLY THE FIRST SAMPLE REMOVED; (D) SAMPLES FROM THE 2ND TO THE 50TH88

FIGURE 6-10. TIME DOMAIN FILTERED VERSION OF THE LPVT SAMPLED DATA TRANSFER FUNCTION. (A) ALL 10,000 SAMPLES; (B) FIRST 9 SAMPLES; (C) ONLY THE FIRST SAMPLE REMOVED; (D) SAMPLES FROM THE 2ND TO THE 50TH89

FIGURE 6-11. SYNTHESIZED SINUSOIDAL INPUT SIGNAL AND THE MEASURED SIGNAL PREDICTION BY SIMULATION. (A) PREDICTION FOR 50 HZ; (B) PREDICTION FOR 500 HZ; (C) PREDICTION FOR 1 KHZ.....92

FIGURE 6-12. SYNTHESIZED DISTORTED INPUT SIGNAL AND THE MEASURED SIGNAL PREDICTION BY SIMULATION. (A) PREDICTION FOR 1ST + 3RD HARMONICS; (B) PREDICTION FOR 1ST + 5TH HARMONICS; (C) PREDICTION FOR 1ST + 7TH HARMONICS; (D) PREDICTION FOR 1ST + 3RD + 5TH + 7TH HARMONICS.93

LIST OF TABLES

TABLE 2-1. LIMITS OF RATIO ERROR AND PHASE DISPLACEMENT FOR MEASURING CURRENT TRANSFORMERS.....	6
TABLE 2-2. LIMITS OF VOLTAGE ERROR AND PHASE DISPLACEMENT FOR MEASURING VOLTAGE TRANSFORMERS	6
TABLE 4-1. DETAILED RESISTORS SPECIFICATION.....	22
TABLE 4-2. RESULTS OF THE RESISTOR CHARACTERIZATION	25
TABLE 4-3. THE TAN DELTA MEASUREMENT RESULTS FOR 7 DIFFERENT CABLE JOINTS IN TERMS GLASS TRANSITION TEMPERATURE.....	28
TABLE 4-4. CHAUVIN ARNOUX 863 DIGITAL THERMOCOUPLE SPECIFICATIONS	31
TABLE 4-5. TAN DELTA VS. TEMPERATURE MEASUREMENT RESULTS	32
TABLE 4-6. TAN DELTA VARIATION BETWEEN MINIMUM AND MAXIMUM TEMPERATURE APPLIED TO THE CABLE JOINTS.....	33
TABLE 4-7. PRESSURE SENSORS MAIN SPECIFICATIONS.....	36
TABLE 4-8. TAN DELTA RESULTS DURING THE PRESSURE TEST FOR THE CABLE JOINTS UNDER TEST	38
TABLE 4-9. PRESSURE SENSOR MAIN SPECIFICATIONS	45
TABLE 4-10. LIST OF ALL PRESSURE MEASUREMENT RESULTS FOR THE 2 CUTs	48
TABLE 5-1. NI-9239 MAIN FEATURES.....	54
TABLE 5-2. FLUKE 6105A MAIN FEATURES	55
TABLE 5-3. COMPONENTS CHARACTERIZATION RESULTS	55
TABLE 5-4. RATED CONDITIONS TEST RESULTS	58
TABLE 5-5. SHORT CIRCUIT TEST RESULTS FOR DIFFERENT LOAD CURRENTS.....	59
TABLE 5-6. CT SERIES PARAMETERS COMPUTATION RESULTS, FOR DIFFERENT LOADS AND TWO TEMPERATURES	59
TABLE 5-7. OPEN CIRCUIT TEST RESULTS FOR DIFFERENT LOAD CURRENTS.....	60
TABLE 5-8. CT SHUNT PARAMETERS COMPUTATION RESULTS, FOR DIFFERENT LOADS AND TWO TEMPERATURES	60
TABLE 5-9. FLUKE TRANSCONDUCTANCE 52120A MAIN CHARACTERISTICS	63
TABLE 5-10. CT SHUNT PARAMETERS FOR DIFFERENT LOADS AND TEMPERATURES	66
TABLE 5-11. RATIO ERROR AND PHASE DISPLACEMENT RESULTS AND THE DECOMPOSITION AT 24 °C.....	66
TABLE 5-12. RATIO ERROR AND PHASE DISPLACEMENT RESULTS AND THE DECOMPOSITION AT 40 °C.....	67
TABLE 5-13. RATIO ERROR AND PHASE DISPLACEMENT RESULTS AND THE DECOMPOSITION AT 50 °C.....	67
TABLE 5-14. RATIO ERROR AND PHASE DISPLACEMENT RESULTS AND DECOMPOSITION AT 65 °C.....	67
TABLE 5-15. QUASI-IDEAL TRANSFORMER RATIO AND PHASE DISPLACEMENT FOR TEMPERATURES 24 °C AND 40 °C.....	67

TABLE 5-16. QUASI-IDEAL TRANSFORMER RATIO AND PHASE DISPLACEMENT FOR TEMPERATURES 50 °C AND 65 °C.....	67
TABLE 5-17. DYNAMIC COEFFICIENTS AND THEIR FUNCTIONS	69
TABLE 6-1. TREK POWER AMPLIFIER FEATURES.....	81
TABLE 6-2. EXPERIMENTAL SR TEST RESULTS IN TERMS OF ϵ AND $\Delta\phi$	85
TABLE 6-3. EXPERIMENTAL SF TEST RESULTS	90
TABLE 6-4. EXPERIMENTAL DW TEST RESULTS.....	90
TABLE 6-5. SF PREDICTION RESULTS AND COMPARISON WITH SR EXPERIMENTAL TEST RESULTS.....	92
TABLE 6-6. DW PREDICTION RESULTS.	94

Acronyms

MV	Medium Voltage
IT	Instrument Transformer
CT	Current Transformer
VT	Voltage Transformer
LPIT	Low Power Instrument Transformer
LPCT	Low Power Current Transformer
LPVT	Low Power Voltage Transformer
SE	State Estimation
EMS	Energy Management System
PMU	Phasor Measurement Units
CIT	Combined Instrument Transformer
CVT	Capacitive Voltage Transformer
HV	High Voltage
DG	Distributed Generation
PD	Partial Discharge
DUT	Device Under Test
VIM	International Vocabulary of Metrology
GUM	Guide to the Expression of Uncertainty in Measurement
ADC	Analog to Digital Converter
THD	Total Harmonic Distortion
DSO	Distribution System Operator
DAQ	Data Acquisition Board
T_G	Glass Transition Temperature
CUT	Cable joint Under Test
DN	Distribution Network
TUT	Transformer Under Test
SC	Short Circuit
FT	Fourier Transform
OC	Open Circuit
RC	Rated Condition
AC	Accuracy Class
IR	Impulse Response
SR	Sinc Response
DFT	Discrete Fourier Transform
DTFT	Discrete Time Fourier Transform
FS	Fourier Series
SF	Single Frequency
DW	Distorted Waveform
IS	Input Sinc
LTI	Linear Time Invariant

1 Introduction

The metrology processes are ongoing in our everyday life and have a more professional role in engineering and industries as well. For the engineering purposes, measurement instruments are used widely. The mass-produced devices which are used as measurement instruments, are already designed, and implemented for specific tasks. The user can use them without being concerned about the measurement processes which are handled inside the instrument. As the measurement instruments are developed for specific tasks and challenges in different fields of engineering, it is always probable to require a measurement unit which has not been developed before as a mass-produced unit. In this case, the prototype measurement setup needs to be developed and implemented. Moreover, sometimes the economical convenience is the reason to design and develop the prototype measurement setup in the lab for specific purposes. In case of design and implementation of measurement setup prototypes, it is not a plug and play instrument as mass produced measurement instrument. In this case the knowledge of metrology is required to accurate development of such setup. Here is the importance of measurement field of study in deeper sense.

This work is an attempt to use metrology and measurement science to develop measurement test setups for the power networks purposes. In detail, 3 different works are performed on power networks with the metrology point of view: i) test setup has been developed for Medium Voltage (MV) cable joints diagnosis in power network. ii) a measurement model has been developed for inductive Current Transformer (CT) modeling. iii) the test setup is developed with new system identification method (Sinc Response approach) for the Low Power Voltage Transformers frequency modeling.

The theoretical studies, experimental tests, analysis, and the results are part of the 3-year Ph.D. research work which are resulted in 14 scientific paper publication in prestigious journals, conferences, workshops, and scientific symposiums. Regarding the time frame, some research works were continuously ongoing for three years. For example, MV cable joint diagnosis is composed of few different and time-consuming tests that it is required to spend few months for cable joints material relaxation after each set of tests. On the other hand, other projects were planned for specific time period to take advantage of the whole three years.

The present Ph.D. thesis is structured as 8 chapters which are described as following: section 2 introduces the role of measurement in power systems and crucial role of measurement for the power networks stability. The voltage and frequency control and their link to the voltage, current, and phase measurement is highlighted. Furthermore, the concept of State Estimation (SE) is introduced to emphasize the importance of measurement accuracy on estimation of the current and voltage at power network nodes which are not equipped with measurement units.

Section 3 establishes the main definitions in metrology which are used during this research work. Moreover, the concept of calibration is highlighted by definition and introducing the adopted test setups for calibration. Different alternatives are described specifically for calibration of instruments. Furthermore, the calibration and characterization concept of measurement units are extended to the measurement setup. It means that the calibration and characterization of the measurement setup is distinguished compared to the measurement units.

In section 4 the Tan Delta measurement setup is developed for MV cable joint diagnosis. The implemented setup is used to analyze the Tan Delta of underground cable joints vs temperature. In next step, the relation between Tan Delta in cable joints vs interfacial pressure between cable and joint common surface, has been analyzed. At the last step in MV cable joint diagnosis, a test setup is designed and implemented to measure the interfacial pressure in cable joints and analyzing the pressure variation vs. thermal cycles applied to the cable joint.

Section 5 deals with the inductive Current Transformers modeling and core parameters extraction using a designed measurement setup. After the core parameter extraction, their variation vs temperature and their effect on CT accuracy is studied. Afterward, the CT is considered as an RL filter and the measured ratio and phase errors are decomposed to extract the effect of only filtering behavior on the CT accuracy. Using the same data, dynamic calibration coefficients are calculated to compensate the CT ratio and phase error under different temperatures and different loading conditions.

Section 6 concerns a new approach introduced as Sinc Response approach for Low Power Voltage Transformer (LPVT) frequency modeling up to 2.5 kHz. The normalized Sinc signal is designed and analyzed for transfer function extraction and prediction of the LPVT output for any known input signals with frequency harmonics less than 2.5 kHz.

In Section 7 some conclusions are stated, and section 8 presents the main references and published paper during the 3-years research work.

2 Power systems and measurement

The measurement can affect power systems mostly in two different ways. One for the technical necessity for accurate voltage and current measurement by measurement unit calibration and characterization, and the other for a more general requirement for power network components diagnostic methods based on measurement. The technical necessity concerns the power network state variables measurement for load flow studies and power network control for stability reason. The more general requirement concerns the measurements for apparatus diagnosis or performing tests on power system components.

Accurate measurement of electrical quantities in power systems is getting more and more a challenging subject for many reasons. With moving from traditional to modernized power systems and networks new concepts, such as electricity market and Smart Grids introduce more and more challenges to overcome. As well known, electric power is considered as a product to be sold in a competitive market. Hence the exact amount of bought or sold electric power should be known with a necessary and required accuracy.

Moreover, from a technical point of view, the measurement of voltages and currents at each node of the power network is required in order to perform a correct voltage and frequency control, and to assure an optimum power flow. Stability of power system, reactive power compensation and fault detection are also directly dependent on these measurements.

The procedure adopted to manage the network control is to inject the measured quantities into a State Estimators (SE). A SE is an algorithm running in the control room processing system whose output is the estimated value of power network state variables (voltages, currents, and phase) in all the nodes with or without measurement units. A SE allows also to estimate quantities at those nodes of the network which are not equipped with measurement units. A modern Energy Management System (EMS) collects in real-time all remote measured quantities from the nodes and provides the solution of the network as its output for fast and live power flow analysis, control, fault location, etc. State estimation is based on mathematical relations between state variables of the system and measured values. In particular, state variables of a typical power network are the currents and the amplitude of the voltages at each bus along with the phase displacement of voltage phasors with respect to the reference universal time. In such

dynamic systems, there is usually a minimum number of state variables to be measured for attaining the full observability of the whole network.

The most important challenge in state estimation is that the measured information, remotely taken and transmitted to the control unit, must feature high accuracy. Moreover, the communication infrastructure must feature suitable reliability.

In order to overcome the aforementioned challenges, measurements need to be first traceable. This is performed by checking and monitoring the metrological confirmation of the measuring units. The metrological confirmation is a set of operations required to ensure that measuring equipment conforms to the requirements for its intended use. Metrological confirmation generally includes calibration and verification. Measurement units technologically are of different type: simple power meters in a given power network node or modern Phasor Measurement Units (PMU).

As mentioned, stability enhancement and fast and robust control of a power network can be reached by measuring phasors of voltage and current at each node and bus or the network and by comparing the phase displacement of the voltage phasors with respect to a reference universal time. One of the important issues to tackle is that the measurement instrumentation is not present in all nodes of distribution networks. This is mainly due by economic as well as practical reasons. So, the accurate estimation of the state variables is accomplished as soon as the measurements in those nodes equipped with measurement units is performed with high accuracy. There are in literature many methods and algorithms capable to reconstruct the measurements at the nodes not covered by instrumentation. The evaluation of the state variables by means of a partial coverage of measuring devices in the networks can be performed by using probabilistic as well as deterministic approaches. They make use of the measurements in the monitored nodes to estimate the measurements in all blind ones. In general, the main limit of all such approaches is that they suffer consistently by the measurement errors. Such errors arise from the non-complete coverage of measurements in network nodes and from the instrumentation used. The combination of such errors can lead to unreliable and very inaccurate evaluation of state variables and, in turn, to a wrong control of the power flow in the network.

Still today there are uncontrollable differences between estimated values of quantities in nodes not equipped with instrument devices and measurements performed in the same nodes by portable measurement instrumentation used for comparison. The main sources of errors are noise added to measured quantities, instrument errors, time difference between measured values, incorrect information about topology of the network, etc. In literature studies aimed at providing information on the sources of errors and how to deal with them in state estimation can be found [1] [2] [3].

The error detection and identification in measurements is one of the most important attributes of the state estimation process in power systems. Some research can be found in literature also in this area. However, at present, error detection and identification is mainly done under the assumption that only one source of error is affecting the measurement results. To reduce the State Estimator output error, at least we need to provide as accurate as possible measurements in the nodes equipped with the measurement units.

The most widespread measurement units are the Instruments Transformers (IT) which are divided to Current Transformers (CT), and Voltage Transformers (VT) categories to measure the current and voltage, respectively. In case of High voltage measurements, Capacitive Voltage Transforms (CVT) are deployed. The Combined Instrument Transformers (CIT) are equipped with both CT and VT in a single unit. The new generation of instrument transformers are more efficient in their size, weight, and the frequency band. The new generation of instrument transformers known as Low Power Instrument Transformers (LPIT) are designed to measure both current and voltages. Low Power Current transformers (LPIT), and Low Power Voltage Transformers (LPVT) are the terminology referring to the LPITs used for current and voltage measurement, respectively.

The calibration and characterization of instrument transformers to reduce the measurement error is the main role of measurement in power networks. On the other hand, to ensure good performance of power system components such as cable joints and terminations, power transformers, switches, etc., diagnostic methods based on measurement are used. This is the second role of measurement for power networks.

2.1 Instrument Transformers in Power Systems

As referred before, Instrument Transformers are used to perform current and voltage measurements in power network nodes. The ITs are the most widespread measurement units deployed in power networks. In general, the ITs use for two purposes: for protection and for measurement.

The ITs used for protection purpose, are not required to have high measurement accuracy. The the main challenge related to protection ITs concerns detection of voltages and currents much higher than rated ones. The detected high current or voltage, triggers the related protection relays for saving the feeder and avoiding damage to the network. In protection CTs, the saturation of magnetic core is challenging, while in protection VTs insulation and withstand is the challenge which is considered during the design.

The ITs used for measurement purposes are the set of ITs which concern the present work. Measurement ITs should hold their promised accuracy class as they are used for power network control and for billing purposes. The accuracy of ITs is evaluated by reporting the ratio error and phase error or phase displacement as two indicative parameters for ITs performance. The accuracy class of measurement ITs is declared on the nameplate and each accuracy class indicates the allowed ratio and phase error. The standard bodies provide the accuracy classes and related ratio and phase errors for each accuracy class. Table 2-1 and Table 2-2 present the accuracy classes for CTs and VTs, respectively from standards [4], and [5].

Table 2-1. Limits of ratio error and phase displacement for measuring current transformers

Accuracy class	Ratio error [\pm %]						Phase displacement									
	at current [% of rated]						\pm Minutes					\pm Centiradians				
							at current [% of rated]					at current [% of rated]				
	1	5	20	50	100	120	1	5	20	100	120	1	5	20	100	120
0.1	-	0.4	0.2	-	0.1	0.1	-	15	8	5	5	-	0.45	0.24	0.15	0.15
0.2	-	0.75	0.35	-	0.2	0.2	-	30	15	10	10	-	0.9	0.45	0.3	0.3
0.5	-	1.5	0.75	-	0.5	0.5	-	90	45	30	30	-	2.7	1.35	0.9	0.9
1	-	3.0	1.5	-	1.0	1.0	-	180	90	60	60	-	5.4	2.7	1.8	1.8
0.2s	0.75	0.75	0.75	0.75	0.75	0.75	30	30	30	30	30	0.9	0.9	0.9	0.9	0.9
0.5s	1.5	1.5	1.5	1.5	1.5	1.5	90	90	90	90	90	2.7	2.7	2.7	2.7	2.7
3	-	-	-	3	-	3	-	-	-	-	-	-	-	-	-	-
5	-	-	-	5	-	5	-	-	-	-	-	-	-	-	-	-

Table 2-2. Limits of voltage error and phase displacement for measuring voltage transformers

Accuracy class	Ratio error [\pm %]	Phase displacement	
		\pm Minutes	\pm Centiradians
0.1	0.1	5	0.15
0.2	0.2	10	0.3
0.5	0.5	20	0.6
1.0	1.0	40	1.2
3.0	3.0	-	-

2.1.1 Inductive CTs and VTs in power networks

The traditional current and voltage transformers which are the most historical measurement unites used in AC power networks, are based on inductive current and voltage transformation. These type of

ITs are designed for High Voltage (HV), and Medium Voltage (MV) levels for both indoor and outdoor applications. Therefore, they are mostly installed in high voltage and distribution substations.

As they are designed based on magnetic induction, the primary and secondary windings in addition to insulation system makes the size and weight considerable which is suitable to be installed in substations. With smart grids point of view, it is required to have CTs and VTs with smaller size and lighter weight to measure the current and voltage Distributed Generation (DG) nodes. In this case using big and heavy inductive ITs is challenging.

The other challenge to use inductive ITs in smart grid environment for DG measurement is the bandwidth which is related to power quality measurement. By increasing use of power electronic components in power networks (in power converters, electric drives, active rectifier, active filters etc.), and high frequency harmonics injection in the network, measurement units should measure the current and voltages up to 2.5 kHz which is power quality frequency range. Inductive ITs especially inductive CTs are limited in frequency range. The inductive ITs behavior in low frequency range or for DC component measurement is not applicable due to inductive law principles. Moreover, nowadays by growing electrical technologies there are quite wide range of applications with current and voltage frequencies much more different than power networks (50 Hz, and 60 Hz) which are required to be measured (such as electric trains). Figure 2-1 and Figure 2-2 show some types of well-known inductive CTs and combined ITs, and VTs in power networks, respectively.



Figure 2-1. From left to right: MV Inductive Current Transformer for indoor application, HV oil-paper insulation Inductive Current Transformer for outdoor application, HV Combined Current and Voltage Transformer

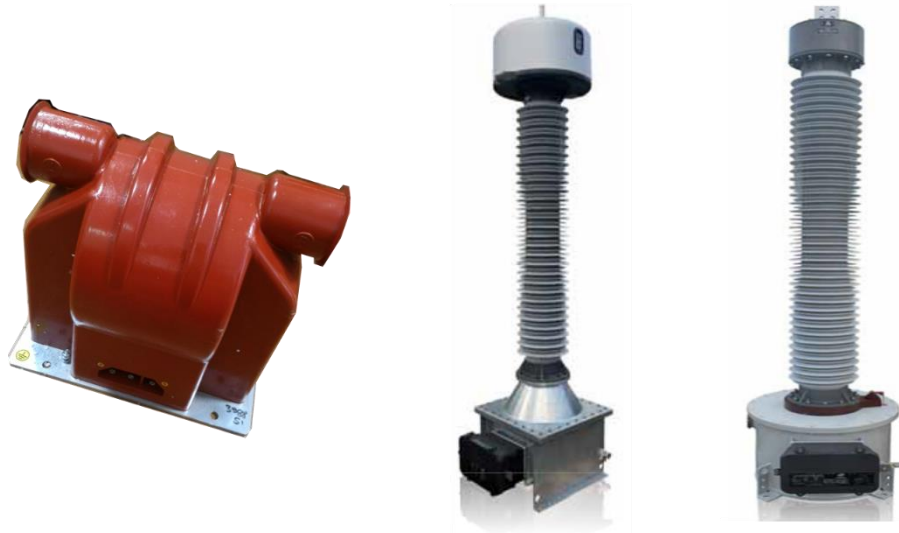


Figure 2-2. From left to right: MV Inductive Voltage Transformer for indoor application, HV oil-paper insulation Voltage Transformer for outdoor application, HV Capacitive Voltage Transformer

Aforementioned facts are the motivation for invention of new instrument transformers with higher weight, smaller size and more bandwidth called Low Power Instrument Transformers (LPIT).

2.1.2 Low Power Instrument Transformers

Low Power Instrument transformers are referred to Low Power Current Transformers (LPCT) and Low Power Voltage Transformers (LPVT) for current and voltage measurement solution, respectively. Unlike the inductive CT and VT, LPCTs and LPVTs are based on different principles.

2.1.2.1 Low Power Current Transformers

As inductive CTs, the LPCTs are based on magnetic induction, but using Rogowski coil magnetic material which has low magnetic permeability and close to air. Using high reluctance magnetic core leads to measuring high current with small output signal in the range of milliamperes. The small output magnitude implies the concept of low power terminology. The output signal can be available in both current and voltage solutions. The LPCTs can be designed with both uniform core and split core magnetic material. During manufacturing process, the magnetic core can be shielded for immunity versus electric or magnetic fields. Figure 2-3 shows some samples of more used LPCTs and combined LPITs.



Figure 2-3. From left to right: split core Rogowski coil LPCT, Uniform core Rogowski coil LPCT, MV Combined LPIT for indoor application, MV Combined LPIT for outdoor application

The LPCTs based on Rogowski coil not only measure accurately a high range of alternating current, but also have a wide frequency range up to few kHz. The different types of LPCTs are also used in application diverse than power network like Partial Discharge (PD) measurement of HV cables for cable diagnostics.

2.1.2.2 Low Power Voltage Transformers

Contrary to inductive VTs which are based on magnetic induction, the LPVTs are based on voltage dividers. The technology can be found based on capacitive, resistive, and resistive capacitive voltage divider. Figure 2-4 represents different types of LPVTs for MV power networks. The resistive LPVTs are easier in terms of implementation but they are vulnerable to electric fields and if it is not well shielded, the ratio and phase error is affected by influence quantities especially electric field. For this reason, capacitive LPVTs are more efficient compared to the other aforementioned types.

On the other hand, capacitive LPVTs are challenging in terms of implementation as the primary capacitance should extruded during the LPVT manufacturing. LPVTs based on capacitive dividers are mainly designed in active and passive configurations. The difference between the two categories concerns the design limitation and the customer preference.



Figure 2-4. From left to right: MV Capacitive LPVT for outdoor application, MV Capacitive LPVT for indoor application, MV Resistive LPVT

Normally, the secondary capacitor is an embedded one, while the primary capacitor is a built-in capacitor obtained from the chassis of the device. For this reason, the built-in primary capacitance may vary from device to device, hence leading to different transformation ratios for different products. To normalize the transformation ratio and phase displacement of each product to the nominal values (after the characterization process) correction factors are provided to the customer by the manufacturer. This type of capacitive LPVTs are the passive ones. It should be noted that in any case the accuracy class is not compromised.

In active LPVTs an active electronic amplifier is added to the passive LPVTs to bring the transformation ratio and phase displacement to the nominal ones so that all final products keep the nominal values declared on the nameplate without introducing extra correction factors.

2.2 Measurement for diagnosis in power systems

In addition to measurement application at power network nodes for control and stability reasons, measurement knowledge is used for diagnosis purposes in power networks. Power networks include a wide range of electric assets, apparatus, and widespread components such as cables, joints, terminations, etc.. The apparatuses such as power transformers, circuit breakers, switchgears, surge arresters, etc. are prone to type tests or routine tests. In order to perform such tests, there is a measurement setup to be designed, calibrated, and implemented. Widespread components such as cables, cable joints, and

terminations should be diagnosed to determine their performance. Moreover, test setups can be designed to characterize and calibrate the measurement units in power network.

Two well-known diagnostic methods for cables, cable joints, and terminations are Partial Discharge (PD) measurement and Tan Delta measurement. The two methods can be applied on different samples in the lab environment for further studies to improve their operation or to indicate the state of insulation health. In any case the measurement setups need to be designed, implemented, and calibrated to perform the studies.

In this work, different test setups are designed and implemented for the purpose of MV cable joints, characterization, calibration of inductive CTs, and LPVTs modeling. It should be noted that there are instruments designed by manufacturers to do some the tests, but using the science of metrology, lets us to design a customized version of the setup, which is cheaper, accurate, and reliable. Tests for diagnostic and characterization purposes are normally done in the lab environment, except for some portable test setups designed for the in-field measurements such as portable standard units for online instrument transformers calibration.

3 Definitions in Metrology

Nowadays, measurement instruments affect our life in different ways. In our daily life we read instruments too many times. For example, reading the speed indicator in the car, reading the car, reading the scale in grocery store, etc.. The everyday used measurement instruments perform measurements and provide us with the measurement results for daily life. In a more specified way, we need to understand what measurement is, and which parameters are defined as tools for performing measurements. In this chapter the purpose is to define the concepts related to metrology which are used in following chapters. To this purpose, it is taken advantage of International Vocabulary of Metrology (VIM) referenced in [6] for the definitions and descriptions.

3.1 Metrology and Measurement

Metrology

Metrology is the science of measurement and its application. Metrology includes all theoretical and practical aspects of measurement, whatever the measurement uncertainty and field of application is. In this regard, the measurement should be defined.

Measurement

Measurement is the process of experimentally obtaining one or more *quantity values* that can reasonably be attributed to a *quantity*. So, a measurement process provides, as a part of the *measurement result*, one or more quantity values that can be attributed to a quantity intended to be measured, that is also called, always according to the VIM [6], *measurand* [7].

To fully understand this definition, we have to refer to the definition of quantity. We can find it again in the VIM.

Quantity

Property of a phenomenon, body, or substance, where the property has a magnitude that can be expressed as a number and a reference.

The VIM states that a reference can be a *measurement unit*, a *measurement procedure*, a *reference material*, or a combination of such.

When physical properties are considered, the reference is generally a measurement unit, whilst, when chemical measurement are considered, the reference is quite often a reference material.

The quantity values provided by the measurement are therefore a number and a reference together expressing the magnitude of a quantity [7].

Is this the measurement result? Or, better, can a measurement result be expressed only by a number and a reference? As we will see later in section 1.5 of this chapter, a measurement procedure cannot provide the “*true*” value of a measurand, due to several factors that we will thoroughly discuss later. This means that a measurement result can only provide a *finite amount of information* about the measurand, and we must know if that amount is enough for the intended use of the measurement result. Otherwise, the measurement result would be meaningless [7].

Therefore, any measurement result has to be provided with an attribute capable of quantifying how close to the measurand’s value the obtained quantity value is. This attribute is called *uncertainty*, and the correct definition of measurement result, as provided by the VIM, is as follows [7].

Measurement result

Set of quantity values being attributed to a measurand together with any other available relevant information.

In a note to this general definition, the VIM states that:

A measurement result is generally expressed as a single *measured quantity value* and a *measurement uncertainty*.

The above general definitions have introduced a number of concepts (*quantity value, reference, relevant information, uncertainty*), that will be covered in the next Sections, and show that a measurement is a definitely more complex procedure than simply reading an instrument.

The science that includes all *theoretical* and *practical* aspects of measurement, regardless to the measurement uncertainty and *field* of application, is called *metrology* and it is already defined in the present section as “the science of measurement and its application” according to VIM [6].

3.2 Uncertainty in Measurement

The knowledge conveyed by the measurement result is aimed at quantifying how complete the information associated with the quantity values provided by the measurement process is [7].

The problem of qualifying the measurement result with a quantitative attribute capable of characterizing the completeness of the information provided about the measurand has been considered since the beginning of metrology and has undergone a significant revision during the last two decades of the twentieth century, when the modern concept of *uncertainty* has been introduced and adopted.

Understanding this concept is not immediate. As noted by the Guide to the Expression of Uncertainty in Measurement (GUM) [8], the word *uncertainty* means doubt, and thus in its broadest sense *uncertainty of measurement* means doubt about the information provided by the result of a measurement. The first question that we have to answer to, if we wish to fully understand the uncertainty concept, is where this doubt originates and why [7].

However, the concept of doubt is hardly quantifiable. Therefore, the use of the term *uncertainty* to quantify how much we should doubt about the obtained measurement result seems somehow contradictory and tautological, since we apparently try to quantify a doubt with a doubt!

Fortunately, this contradiction is only apparent and is due to a lexical problem. Because of the lack of different words for the *general concept* of uncertainty and the specific quantities [7].

3.3 Calibration

Calibration is defined as operation that, under specified conditions, in a first step, establishes a relation between the *quantity values* with *measurement uncertainties* provided by *measurement standards* and corresponding *indications* with associated measurement uncertainties, and in a second step, uses this information to establish a relation for obtaining a *measurement result* from an indication [6].

A calibration may be expressed by a statement, calibration function, *calibration diagram*, *calibration curve*, or calibration table. In some cases, it may consist of an additive or multiplicative *correction* of the indication with associated measurement uncertainty. Calibration should not be confused with *adjustment of a measuring system*, often mistakenly called “self-calibration”, nor with *verification* of calibration. Often, the first step alone in the above definition is perceived as being calibration [6].

3.4 Calibration Hierarchy

By VIM definition [6], calibration hierarchy is a sequence of *calibrations* from a reference to the final *measuring system*, where the outcome of each calibration depends on the outcome of the previous calibration.

Measurement uncertainty necessarily increases along the sequence of calibrations. The elements of a calibration hierarchy are one or more *measurement standards* and measuring systems operated according to *measurement procedures*. For this definition, the ‘reference’ can be a definition of a *measurement unit* through its practical realization, or a measurement procedure, or a measurement standard. A comparison between two measurement standards may be viewed as a calibration if the comparison is used to check and, if necessary, correct the *quantity value* and measurement uncertainty attributed to one of the measurement standards [6].

3.5 Verification

VIM [6] defines the verification as provision of objective evidence that a given item fulfils specified requirements. An example is the confirmation that performance properties or legal requirements of a *measuring system* are achieved.

When applicable, *measurement uncertainty* should be taken into consideration for verification procedure. The item for verification may be a process, measurement procedure, material, compound, or measuring system and the specified requirements may be that a manufacturer's specifications to be met [6].

Verification in legal metrology, in conformity assessment in general, pertains to the examination and marking and/or issuing of a verification certificate for a measuring system. Verification should not be confused with *calibration* and not every verification is a *validation* [6].

3.6 Validation

Validation is the *verification*, where the specified requirements are adequate for an intended use [6]. For example, a *measurement procedure*, ordinarily used for the *measurement* of Tan Delta of a cable sample, may be validated also for measurement of Tan Delta of cable joint.

3.7 Metrological Traceability

Metrological traceability is the property of a *measurement result* whereby the result can be related to a reference through a documented unbroken chain of *calibrations*, each contributing to the *measurement uncertainty*. For this definition, a ‘reference’ can be a definition of a *measurement unit* through its practical realization, or a *measurement procedure* including the measurement unit for a non-ordinal quantity, or a *measurement standard* [6].

Metrological traceability requires an established *calibration hierarchy*. Specification of the reference must include the time at which this reference was used in establishing the calibration hierarchy, along with any other relevant metrological information about the reference, such as when the first calibration in the calibration hierarchy was performed [6].

For *measurements* with more than one *input quantity in the measurement model*, each of the input *quantity values* should itself be metrologically traceable and the calibration hierarchy involved may form a branched structure or a network. The effort involved in establishing metrological traceability for each input quantity value should be commensurate with its relative contribution to the measurement result [6].

Metrological traceability of a measurement result does not ensure that the measurement uncertainty is adequate for a given purpose or that there is an absence of mistakes. A comparison between two measurement standards may be viewed as a calibration if the comparison is used to check and, if necessary, correct the quantity value and measurement uncertainty attributed to one of the measurement standards. The abbreviated term “traceability” is sometimes used to mean ‘metrological traceability’ as well as other concepts, such as ‘sample traceability’ or ‘document traceability’ or ‘instrument traceability’ or ‘material traceability’, where the history (the “trace”) of an item is meant. Therefore, the full term of “metrological traceability” is preferred if there is any risk of confusion [6].

3.8 Calibration Process

The metrological calibration process in the world of measurement technology is the documented comparison of the **measurement device** to be calibrated against a traceable reference device. As it is

highlighted, the metrological calibration concerns a **measurement device**. For some measurement devices such as Instrument Transformers, the accuracy class is one of the most important characteristics of that measurement unit. Therefore, if the purpose is to characterize the accuracy class of an instrument transformer, it can be considered as part of the calibration procedure. This is a source of confusion between ITs calibration and characterization, while most of measurement units unlike the ITs get calibrated and not characterized in terms of their accuracy.

In case of other elements which are not measurement devices, the characterization makes a totally independent sense rather than calibration. For example, in case of a Resistor to be characterized, the **resistance value** is the main characteristic to be found accurately. As it is clear, the resistance value can be measured using a measurement unit or measurement setup with a calculated uncertainty. In the Resistor characterization example, a measurement setup for resistor characterization can be composed of a calibrated voltage source, and a calibrated current meter (or a characterized shunt resistor). Both calibrated voltage source and current meter can be traceable reference devices.

The ratio and phase errors are the main characteristics of Instrument Transformers, the ratio and phase errors should be calculated for both characterization and calibration. Namely, based on calibration definition, the process for ITs calibration or characterization is the same as calibration of a general measurement device. For this reason, even for ITs we refer to the term “calibration” rather than “characterization”.

3.8.1 Instrument Transformers Calibration

The purpose is to provide the possible procedures for ITs calibration in a measurement lab. As mentioned in previous section, by calibration, the ratio and phase error are extracted as main characteristics of the instrument transformers. The ratio and phase error calculation are used multiple times for studies in next chapters and for this reason the instrument transformers calibration process should be studied. Based on the calibration definition, the ITs calibration procedure requires a measurement setup composed of a traceable reference instrument transformer to be compared with the Device Under Test (DUT) which is the instrument transformer to be calibrated. Figure 3-1 represents such calibration setup.

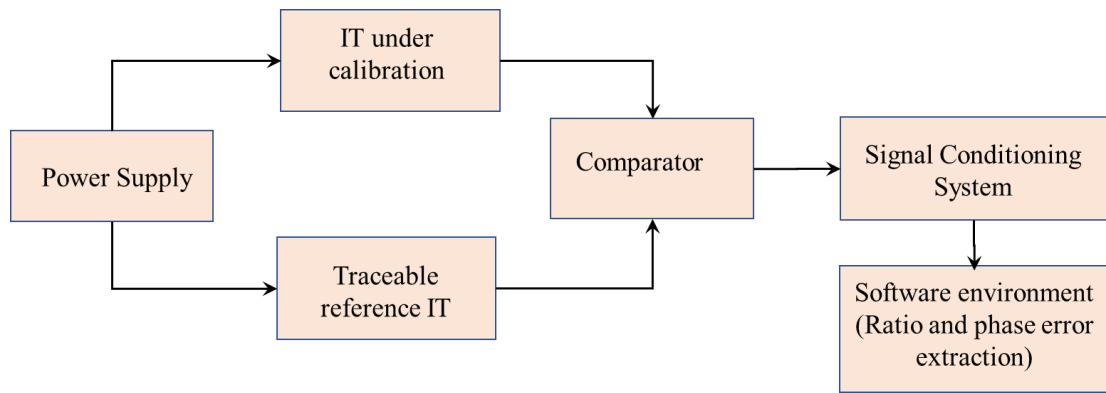


Figure 3-1. IT Calibration test setup using a traceable reference IT to be compared with the IT under calibration

The main components of such calibration setup are: Power supply, traceable reference instrument transformer, comparator, IT under calibration, signal conditioning acquisition system, and a processing unit or a PC to perform the numerical analysis. The signal conditioning system refers to the possible amplifiers or attenuators, Analog to Digital Converter (ADC), and the rest of data acquisition chain. In case of Electronic ITs, sometimes the primary signal needs to be amplified and it is possible to have more amplifiers in the calibration setup. It should be noted that, in addition to traceable reference IT which is the core of the calibration setup, the comparator and all components of signal conditioning chain have to be characterized and calibrated to have a calibrated calibration setup. It is important to mention that the power supply is not required to be calibrated as long as both reference IT and IT under test experience the same signal in primary side. Regarding the power supply, the Total Harmonic Distortion (THD) of the signal must be negligible and it is necessary to perform Discrete Fourier Transform (DFT) analysis to extract the main harmonic.

3.8.2 Instrument Transformer Calibration using Calibrator Devices

The alternative solution for ITs calibration without a traceable IT, is to focus on the power supply side and use a traceable voltage calibrator (in case of VT calibration) or traceable current calibrator (in case of CT calibrator). In this case, the applied voltage or current signals are guaranteed to be accurate and they don't need to be compared with the signal measured by a traceable reference IT. As a result, this setup does not have neither the reference IT, nor the comparator. The test setup is composed of reference standard signal calibrator, IT under test, signal conditioning system, and the PC for numerical

analysis. Figure 3-2 shows a schematic of the calibration test setup with reference calibrator and without both reference instrument transformer and comparator.

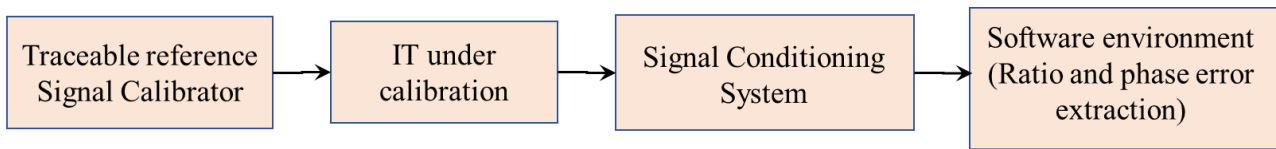


Figure 3-2. IT Calibration test setup using a traceable reference signal calibrator and without reference IT and comparator

3.8.3 Measurement setup calibration

Measurement setup are developed and implemented for perform measurement for different purposes. For example, in next chapters a measurement setup has been designed to measure loss factor (Tan Delta) of cable joint, while a measurement setup can be designed to calibrate or characterized in instrument transformer (calibration test setup). In any case, a guarantee is required to have an accurate and reliable measured value. In other word, the measurement setup has to be calibrated by itself. If we consider a calibration setup, even the calibration setup needs to be calibrated by itself.

By calibration definition, the device under calibration should be compared with a reference one. If the setup is a prototype implemented in laboratory, this task can be done by characterization or calibration of any single component of the measurement setup under calibration. For example, if there is any amplifier in the measurement setup, it should be characterized separately by another setup, or if there is any comparator, it should be calibrated by a separate calibration setup and the error due to the comparator should be compensated. The term “characterization” is used for the amplifier, because it is considered as a component with a specific transformation ratio and not a measurement unit, while the term “calibration” is used for the comparator as it is a measurement unit which measures the difference between two signals.

4 Measurement for MV Cable Joints Diagnosis

The use of underground medium voltage (MV) cables is nowadays widespread among utilities. Its usage allows network operators to avoid all the issues that arise from the deployment of overhead lines and cables. For example, vegetation is one frequent cause of failure for overhead lines. In addition, overhead cables, which seem to protect the power network from that issue, are affected, mainly in the rural areas, by hunters' bullets. They damage, in multiple points, the typical 3 bundled cables which compose the power network. This results in very difficult-to-detect faults position and expensive cables replacements.

For the abovementioned reasons, underground cables are deployed in many countries. However, they are not fault-free. In particular, the majority of faults happen in the critical points of a cable: the terminals and the joints. Other sources of faults could be related to the cable insulation, but they are frequently due to external causes (mechanical actions on the cable) independent of the electrical characteristics. Considering now the main causes of fault, specific monitoring systems must be implemented to understand why they happen. Scientific literature contains a variety of contributes which could be distinguished, firstly, in on-line [9] and off-line [10] monitoring. Clearly, the former is considerably tougher than the latter due to the limitation of maintaining the network powered.

In this section, the attention is focused on one of the critical causes and components of fault in the cable: the joint. It is fundamental either for enlarging or restoring the power networks when a fault happens. However, the high rate of cable joint explosion causes intensive costs for maintenance, increases the outage time, and penalizes the Distribution System Operators (DSOs) as they cannot deliver the promised electric power. These issues for underground cable power networks make it necessary to study the diagnostic methods to prevent cable joints explosion, hence the outage of the power network. To this purpose, different diagnostic techniques have been developed in the literature. For example, partial discharge (PD) measurement is tackled in [11], while the electric field analysis is described in [12] and [13]. Another paramount diagnostic method, which can provide crucial information about the aging of the joints due to different influent quantities, is the Tangent Delta (or Tan Delta, $Tg\delta$) measurement. In [14], [15], [16] high frequency tests have been applied on joints to extract $Tg\delta$, while in-field measurements have been performed in [17] to extract $Tg\delta$ and PD.

In the following, first the test setup has been designed and implemented to measure the Tan Delta related to MV underground cable joints. In the second stage, the Tan Delta variation vs. Temperature has

been tackled. Afterwards, the Tan Delta variation vs. interfacial pressure inside the cable joints has been studied. At the end, to close the cause-and-effect loop, the measurement setup to measure the interfacial pressure inside the cable joint is designed, and interfacial pressure variation vs. temperature is analyzed.

4.1 Test Setup Design, and Calibration for Tan Delta Measurements on MV Cable Joints

In this subsection, a simple test setup to measure Tan Delta of cable joint samples has been designed and calibrated for the purpose of MV underground cable joints diagnosis. The setup is designed and tested under 1 kV applied voltage and 50 Hz frequency.

In the following we will see: description a cable joint in detail, the proposed test setup for the Tan Delta measurement, cable joint preparation in order to being tested with the setup, and then the Tan Delta measurement technique is fully described. The test results are presented afterwards, and finally the conclusions are stated.

4.1.1 Cable joint description

To clarify the aim of this work, a cable joint needs to be fully described. In Figure 4-1 it can be seen all the layers which compose the joint. From the outside to the inside there are:

1. the cold shrink.
2. the metallic mesh, it connects the ground potential between the two portions of cable separated by the joint.
3. the silicon rubber covered by an inner and an outer semi-conductive layer, to uniformize the electric field. Such silicon will be the layer under test for the Tan Delta measurement.
4. The conductor.

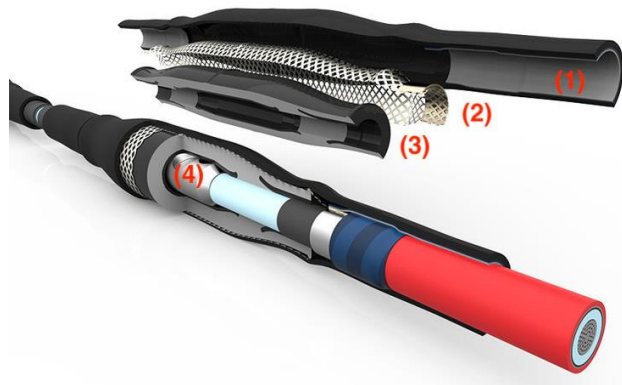


Figure 4-1. Cable joint cross section description (courtesy of REPL Italy)

Cable joints are installed all along the network to extend it or restore it in case of faults. They connect two pieces of cable which could be, in some cases, either of different insulations (e.g. XLPE cables and paper-oil cables) or of different conductor materials (copper or aluminum). The outer part of a joint, the shrink, complete the joint covering everything on its inside, preventing damages and external actions. This part could be built in two different ways, referred as: cold shrink and heat shrink. The former consists in a silicon material placed over a removable plastic core. When removed, the rubber seals around the conductor. The latter, instead, requires a source of heat, for example from a gas torch, to shrink over the joint. Recently, the cold shrinks are substituting the use of heat shrinks. This is because there is no need of direct flames to install them, hence there is a reduced risk for both the user and the joint itself.

Another paramount component of the joint is the dielectric layer (item 3 in Figure 4-1). It is the insulator, hence representable with a capacitor and a resistor in parallel, that cover the junction created from the union of the two portions of cable. The quality of this layer, can be evaluated with the Tan Delta measurement, detailed in the following, which reveal the dielectric degradation.

4.1.2 Test Setup Design

Figure 4-2 shows a schematic representation of the Tan Delta automatic measurement setup. It includes: a programmable power source Agilent 6813B, an isolation transformer, a step-up voltage transformer (0.1 kV/15 kV), a resistive voltage divider, a shunt resistor, a Data Acquisition Board NI9239 (DAq), a personal computer and of course the cable joint under test. The power source is used to provide a 50 Hz-sinusoidal voltage. This way, voltage distortions and frequency changes are avoided, which can lead to an incorrect estimate of the Tan Delta. The power source voltage output, raised through the step-up transformer, feeds the cable joint under test with a voltage limited to 1 kV RMS, for minimizing the risk of joint discharge. The resistive voltage divider is composed by $R_H = 2 \text{ M}\Omega$ and $R_L = 10 \text{ k}\Omega$, on the high and low voltage sides, respectively. It is used to measure the voltage \bar{V}_j at the cable joint terminals, by means of the DAq. The NI9239 Data Acquisition board is used in all my research projects and it features 24-bit ADC resolution, 50 kS/s/ch sample rate, 0.03% gain error, and 0.008% of offset error. The NI9239 Data Acquisition Board uncertainty has been analyzed in section 4.1.4.1.

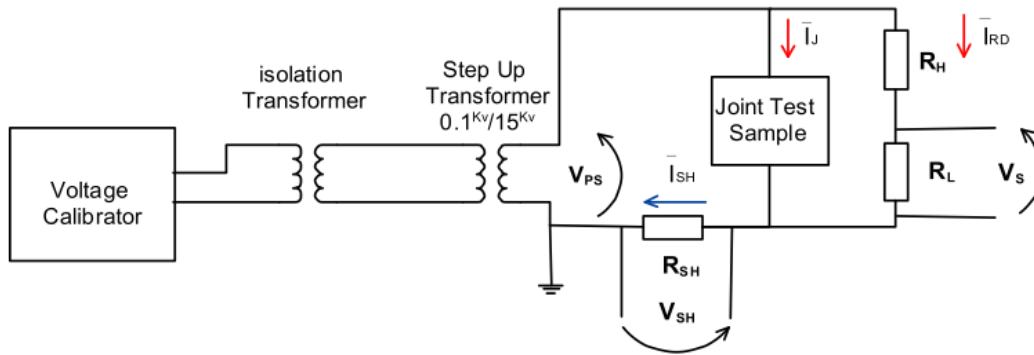


Figure 4-2. Automatic measurement setup for the Tan Delta Measurement

To measure the current provided by the step-up transformer, a shunt resistor $R_{SH} = 10 \text{ k}\Omega$ has been used. Its voltage-drop \bar{V}_{SH} is acquired by the DAq. Table 4-1 lists the specifications of R_{SH} , R_H and R_L . The equivalent circuit of the proposed setup is shown in Figure 4-3. C_J and R_J represent the equivalent capacitance and resistance of the joint under test, respectively. Under working conditions, the power dissipated by the resistors is significantly lower than their rated one, except for R_H , where rated and dissipated power are comparable (0.75 W and 0.55 W). However, due to its very lower thermal drift (5 ppm/°C) this does not affect the accuracy.

Table 4-1. Detailed Resistors Specification

Resistor	Resistance	Accuracy	Power	Temperature drift
R_H	2 M Ω	0.01 %	0.75 W	5 ppm/°C
R_L, R_{SH}	10 k Ω	0.005 %	0.6 W	0.2 ppm/°C

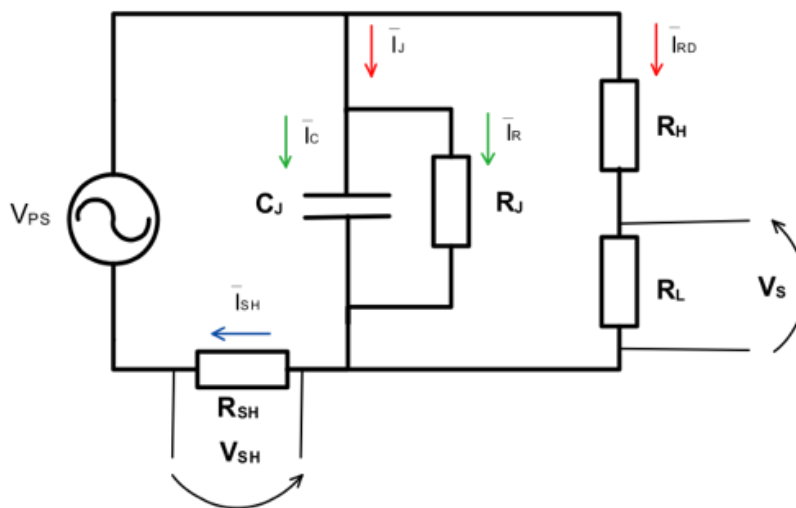


Figure 4-3. Equivalent electric circuit of the proposed setup

4.1.3 Sample Preparation

Samples used for Tan Delta measurement are cold shrink joints and the insulating material is silicon rubber. Seven samples are used with Glass Transition Temperature (T_G) ranging from 90 °C to 150 °C with steps of 10 °C. The joints connect two pieces of 130 mm² cables having length of about 0.5 m. Glass Transition Temperature of a material is the temperature at which the transition from the glassy to the rubbery state starts. T_G is always lower than the melting temperature of the material.

The samples used do not have the outer shrink and the metallic mesh, hence the dielectric object of study is already available. However, to perform a Tan Delta measurement, the metallic mesh is required for being used as ground potential electrode. The high voltage potential electrode is given by the cable conductor. Therefore, an aluminium foil layer has been applied to the dielectric of the joint to recreate the ground electrode. This can be seen in Figure 4-4, where the upper picture represents the original joint while the lower picture the joint after the aluminium application.



Figure 4-4. Picture of the cable joint under test before and after its preparation with aluminium foils

As for the contribution of the surface discharge to the Loss Factor, a simple test has been performed. Tan Delta has been measured when the discharge from the conductor to the semiconductor was very long (picture 1 in Figure 4-5) and when it was the shortest possible which is the radius of the cable (picture 2 and 3 of Figure 4-5). The results of both tests were identical; hence the surface discharge effect is negligible and then not considered in the following results.

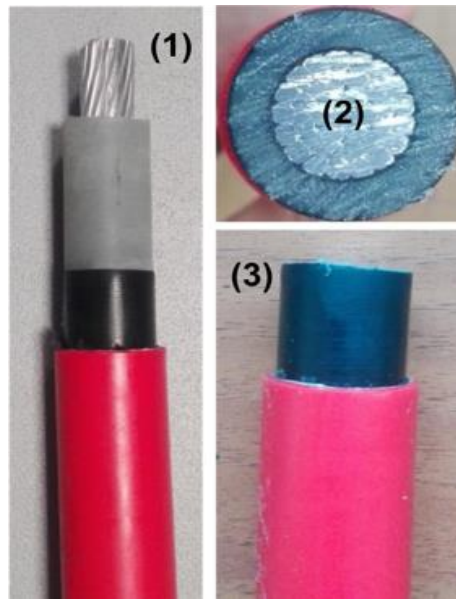


Figure 4-5. Picture from the cable: 1, the longest insulator path considered, 2 and 3 the minimum insulator path used for surface discharge test

4.1.4 Tan Delta Measurement Technique

Before detailing the procedure adopted for the measurements, Tan Delta must be defined. Figure 4-6 shows the equivalent circuit of a cable joint. It is then possible to define the Tan Delta (or dissipation factor) as ratio between the current flowing through the joint equivalent resistor and the one flowing through its equivalent capacitor (4-1).

$$\text{Tan}(\delta) = \frac{\bar{I}_R}{\bar{I}_C} \quad (4-1)$$

Hence, (4-1) represents the tangent of the dissipation angle δ , showed also in Figure 4-6.

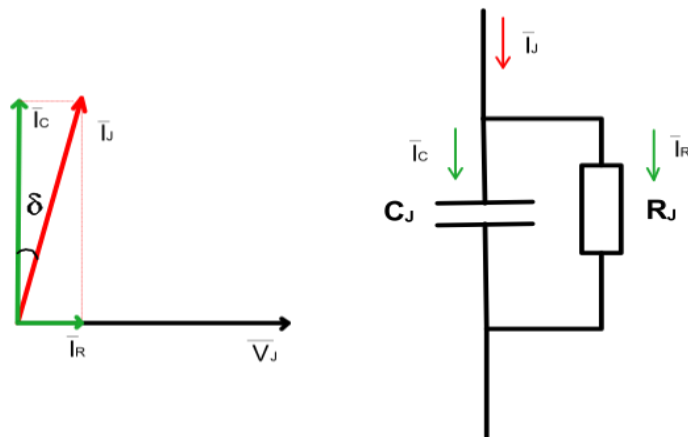


Figure 4-6. Right: equivalent circuit of a cable joint
Left: dissipation angle represented in the phasors plane

4.1.4.1 R_{SH} , R_H and R_L calibration

One element required to the Tan Delta measurement setup (Figure 4-2) is the resistive voltage divider. It allows to measure the voltage applied to the cable joint \bar{V}_J and it needs to be characterized. To this purpose, 1000 measurement have been acquired for all the resistors using the multimeter HP 3458A under metrological confirmation. According to [18] it features the following accuracy specification: 10 ppm of reading and 0.5 ppm of range, and 50 ppm of reading and 10 ppm of range, for the 10 k Ω and 10 M Ω ranges, respectively. Table 4-2 lists the mean value, the standard deviation u_A of the 1000 measurement performed, the standard uncertainty u_B (obtained from the multimeter parameters) and the relative combined uncertainty $u_C = \sqrt{u_A^2 + u_B^2}/R$ of the two resistors R_L and R_H that compose the divider and the shunt resistor R_{SH} used for the current measurement. It can be noted that all the combined uncertainties are lower than the rated accuracy provided by the manufacturers (Table 4-1). In addition, from the results of the Table the mean value and the uncertainty affecting the resistive divider ratio have been calculated. It is:

$$K = 201.01 \pm 0.02 \quad (4-2)$$

using a coverage factor of 2 and being,

$$K = \frac{R_L + R_H}{R_L} \quad (4-3)$$

Hence:

$$\bar{V}_J = K \bar{V}_S \quad (4-4)$$

Table 4-2. Results of the Resistor Characterization

Resistors	Mean Value [Ω]	u_A [Ω]	u_B [Ω]	u_C [-]
R_H	$2.0000 \cdot 10^6$	30	115	$5.9 \cdot 10^{-5}$
R_L	$9.9999 \cdot 10^3$	0.005	0.06	$6.0 \cdot 10^{-6}$
R_{SH}	$9.9994 \cdot 10^3$	0.003	0.06	$6.0 \cdot 10^{-6}$

AS Equation (4-4) shows, the uncertainty related to \bar{V}_J is driven from the uncertainty calculated for K (Equation (4-2)) and the uncertainty of measured \bar{V}_S . The systematic contribution to uncertainty of NI9239 Data Acquisition Board can give quantitative value for uncertainty to be sure that it can be neglected. To this purpose, we know that the cable joint experiences 1kV test voltage ($|\bar{V}_J|$) and considering the transformation ratio of the resistive voltage divider ($K = 200$), we have 5V in the resistive divider output ($|\bar{V}_S|$). Given that the NI9239 DAQ features 0.03% gain error and 0.008% of full-scale

error, type B method to calculate the systematic contribution to uncertainty leads to 1mV uncertainty which is 0.02% of the 5V measured voltage.

It is useful to discuss the effect of the noise on NI9239 DAQ. The reported input noise for this data acquisition board is $70 \mu V rms$. Considering the measured voltage of about 5 V we see that the effect of noise is negligible and the DAQ acts very satisfactory for our purpose. Considering $70 \mu V rms$ input noise, the Signal to Noise And Distortion (SINAD) of the NI9239 DAQ is 100 dB which is used to calculate Enable Number Of Bits (ENOB). The values shows that ENOB is 16 Bits for NI9238 DAQ with total number of 24 Bits.

Moreover, NI9323 features $1 M\Omega$ input impedance which is in parallel with the $10 k\Omega$ resistor in the voltage divider output. This effect is considered during signal conditioning. The performed uncertainty and loading effect analysis on DAQ, holds also for all other measurement setups in next chapters.

4.1.4.2 Measurement Algorithm

The main idea for the Tan Delta measurement is summarized in the flowchart depicted in Figure 4-7. It consists in the acquisition of the voltages on the resistive divider and on the shunt resistor, \bar{V}_S and \bar{V}_{SH} , respectively. Both are used to compute the current \bar{I}_{RD} flowing through the resistive divider and the one \bar{I}_{SH} flowing through the shunt resistor.

$$\bar{I}_{RD} = \frac{\bar{V}_S}{R_S} \quad (4-5)$$

$$\bar{I}_{SH} = \frac{\bar{V}_{SH}}{R_{SH}} \quad (4-6)$$

At this point, the current in the cable joint can be obtained as:

$$\bar{I}_J = \bar{I}_{SH} - \bar{I}_{RD} \quad (4-7)$$

Hence, the dissipation angle is:

$$\delta = \frac{\pi}{2} - \theta_{IV} \quad (4-8)$$

where θ_{IV} is the angle between the current and the voltage of the joint under test:

$$\theta_{IV} = \hat{I}_J - \hat{V}_J \quad (4-9)$$

Finally, the $Tg\delta$ is calculated as the tangent of (4-8). Figure 4-8 highlights the phasors acquired and used for the dissipation angle calculation.

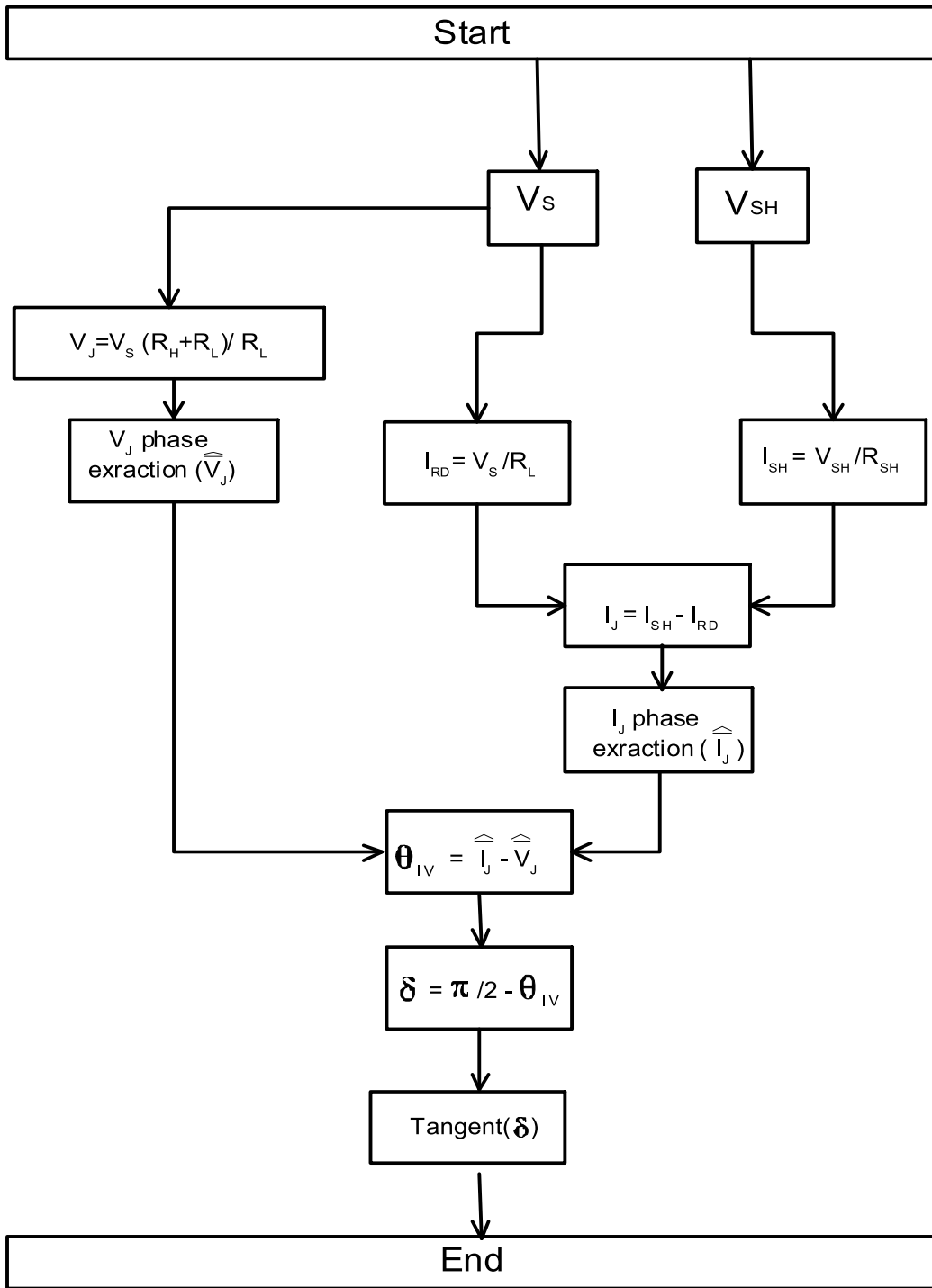


Figure 4-7. Tan Delta Measurement algorithm

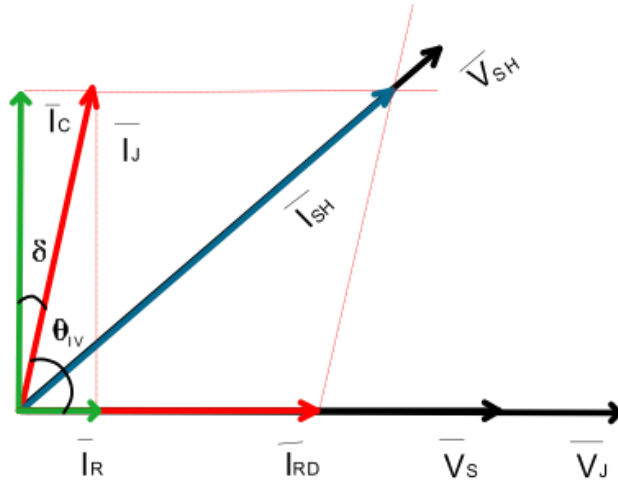


Figure 4-8. Voltage and current phasors acquired for the Tan Delta measurement

4.1.5 Tan Delta Measurement Results

The abovementioned procedure has been applied to test seven cable joints, which differ for their Glass Transition Temperature imposed by the manufacturer. To evaluate Tan Delta, 1000 measurements have been acquired and mean value and standard deviation $\sigma_{Tan\delta}$ have been calculated. All tests have been performed at an ambient temperature of 23 °C. Table 4-3 reports, for each cable joint, its Tg and mean value and $\sigma_{Tan\delta}$ of the Tan Delta. From the results, it can be stated that, the proposed setup can be used to measure, with significant accuracy, typical values of Tan Delta variations. In fact, also applying a cover factor of 3, standard deviation in order of 10^{-5} it is obtained. Moreover, such values are consistent with the ones used in dielectric diagnostic of cables. Even if a biased existed in the measurements, it would not affect the results since all the tests have been performed at the same way.

Table 4-3. The Tan Delta Measurement Results for 7 different Cable Joints in terms Glass Transition Temperature

#	Joint Tg [°C]	Tan Delta Mean Value [-]	$\sigma_{Tan\delta}$
1	90	$1.351 \cdot 10^{-2}$	$1 \cdot 10^{-5}$
2	100	$2.213 \cdot 10^{-2}$	$1 \cdot 10^{-5}$
3	110	$1.704 \cdot 10^{-2}$	$1 \cdot 10^{-5}$
4	120	$1.547 \cdot 10^{-2}$	$1 \cdot 10^{-5}$
5	130	$1.464 \cdot 10^{-2}$	$1 \cdot 10^{-5}$
6	140	$1.457 \cdot 10^{-2}$	$1 \cdot 10^{-5}$
7	150	$1.393 \cdot 10^{-2}$	$1 \cdot 10^{-5}$

As a further comment, from the results it seems that the Tan Delta of a cable joint is not affected by its Tg. However, further studies are necessary to evaluate this statement in different working conditions.

4.1.6 Conclusions

To avoid power network outages, its critical components must be studied, and the causes of such outages investigated. In particular, joints are one of the frequent causes of fault in MV cable networks. With this aim, an automatic test setup for the Tan Delta measurement on cable joints has been presented; which is one of the key tests to diagnostic the state of a cable. Such a setup has been calibrated and used to measure Tan Delta in 7 cable joints with Glass Transition Temperatures ranging from 90 to 150 °C. Provided results demonstrate the test setup efficiency being able to measure typical values of Tan Delta variations with a sufficient level of accuracy. Hence, the proposed setup could be used for the dielectric cable diagnostic, which give a reliable information of the cable degradation. It has been seen how the Glass Transition Temperature of the cable does not affect its Tan Delta measurement. The presented section is published as [19] Further studies are done in next chapters about the effect of temperature and interfacial pressure on the MV underground cable joints.

4.2 Effects of Temperature on MV Cable Joints Tan Delta Measurements

In this section, the test setup, which was designed and implemented in previous section, has been used to measure the cable joints Tan Delta to analyze cable joints Tan Delta behavior versus temperature. The setup was designed and tested under 1 kV applied voltage and 50 Hz frequency. This section deals with one of the causes that affects Tan Delta measurements: the temperature. Many works in the literature tackled the effects of temperature on electric assets [20] [21] and cable joints. In [22] [23] authors simulated the joint behavior when affected by temperature, while in [24] the failure rate vs. temperature is described. However, none of the works in the literature approach the temperature issue with the following point of view: connecting the tan delta measurement to the ambient temperature of the cable joint. To this purpose, the setup proposed in last subsection, is used to measure Tan Delta in different joints at three different temperatures: 10, 24 and 60 °C.

The section is structured as follows: the cable joint preparation is described, the test procedure is presented, the obtained results are discussed, and finally, conclusions are stated.

4.2.1 Sample Preparation

Samples used for Tan Delta measurement are cold shrink joints and the insulating material is silicon rubber, as described in Figure 4-1. In the measurements described in the following, three different joints have been selected. One joint has been collected from the field. After an in-field fault, the faulted joint was replaced, and immediately it has been cut and brought to the lab. This was done without informing the company responsible for the junction, to guaranteeing in-field working conditions. The other two cable joints instead are completely new and with a Glass Transition temperature of 100 and 150 °C, respectively. In the following, the three joints are referred as: in-field, TG 100, and TG 150, respectively. The joints connect two pieces of 130 mm² cables having length of about 0.5 m.

The used samples do not have the outer shrink and the metallic mesh; hence the dielectric object of study is easily accessible. However, to perform a Tan Delta measurement, the metallic mesh is required for being used as ground potential electrode, whereas the high voltage potential electrode is given by the cable conductor. Therefore, an aluminium foil layer has been applied to the dielectric of the joint to recreate the ground electrode. This is the same as the samples prepared in last section shown in Figure 4-4, where the upper picture represents the original joint while the lower picture the joint after the aluminium application.

4.2.2 Measurement Procedure

In this Section the proposed measurement technique is described. The aim is to measure Tan Delta of the three abovementioned joints at three different temperatures: 10, 24 and 60 °C. At a first sight, the temperature range chosen could not seem very spread. However, considering that the cables are installed underground (either in soil or concrete), it results in ambient temperatures varying moderately during the normal operations and completely comparable to the selected ones. Temperature is applied to the joints using a thermal chamber which can fit the three joints at the same time. Furthermore, to verify the temperature inside the chamber and on the joints a Chauvin Arnoux 863 thermocouple has been used. Its characteristics are summarized in Table 4-4. Its two thermocouple channels have been placed in two different points of the chamber: one in the upper right corner, and one in the lower left corner. That is to ensure a proper thermal uniformity in the whole chamber.

Table 4-4. Chauvin Arnoux 863 Digital Thermocouple Specifications

Measurement range	(-50 ÷ +1300) °C
Resolution	0.1 °C
Accuracy	± 0.3 % of reading

At the light of the aforementioned, the joints were subjected to the following thermal cycles:

- The three joints are placed inside the chamber and, at ambient temperature (24 °C) the Tan Delta is measured as described.
- The chamber is then set to 60 °C. To ensure the thermal stability of the joints under test, the temperature has been maintained for 1 night (12 hours) before collecting the quantities for the Tan Delta computation.
- The joints are then naturally cooled to return at the ambient temperature before setting the lower temperature (10 °C).
- Finally, one more night has been waited before measuring the Tan Delta values at 10 °C.

In the overall, 3 days were necessary to perform one cycle of measurements for the three joints. The same cycle was repeated 8 times so that one month was required to complete the tests.

4.2.3 Measurement Results

The abovementioned procedure has been applied to test three cable joints: the in-field, the TG 100 and the TG 150 joints. To evaluate Tan Delta, 1000 measurements, for each test, have been acquired and mean value $\text{Tan}\delta$ and standard deviation $\sigma_{\text{Tan}\delta}$ have been calculated.

$\text{Tan}\delta$ and $\sigma_{\text{Tan}\delta}$ for the three joints under test and at the three temperatures are listed in Table 4-5 for one of the eight cycles (similar figures have been obtained for all of them). As a first comment, Tan Delta values and standard deviations are consistent with the ones in Table 4-3, where Tan Delta was measured in previous section with the same measurement setup. It confirms the performance of the setup developed in previous section for Tan Delta measurement.

Table 4-5. Tan Delta vs. Temperature Measurement Results

Sample	10 °C		24 °C		60 °C	
	Tanδ [-]	$\sigma_{Tan\delta}$ [-]	Tanδ [-]	$\sigma_{Tan\delta}$ [-]	Tanδ [-]	$\sigma_{Tan\delta}$ [-]
In-field	0.03563	$5 \cdot 10^{-5}$	0.01852	$1 \cdot 10^{-5}$	0.01369	$1 \cdot 10^{-5}$
TG 100	0.05419	$6 \cdot 10^{-5}$	0.043009	$6 \cdot 10^{-6}$	0.003068	$8 \cdot 10^{-6}$
TG 150	0.04662	$6 \cdot 10^{-5}$	0.02042	$1 \cdot 10^{-5}$	0.00519	$1 \cdot 10^{-5}$

To better understand and present the results, Figure 4-9, Figure 4-10, and Figure 4-11 are provided for the in-field, TG 100 and TG 150 joints, respectively. It is evident from the comparison among the three that a common behaviour exists: The Tan Delta of all the three joints is decreasing when the temperature increases. Continuing the overall comparison, it can be highlighted that low temperatures cause a degradation of the Tan Delta value; in some cases, up to one order of magnitude greater than the values at 24 °C. In this concern, Table 4-6 presents, for the 3 joints under test, the percentage variation between 10 °C and 60 °C of the Tan Delta. From the Table it results that the in-field made joint has the best behaviour in terms of temperature with respect to the others. In other words, the in-field joint does not suffer the temperature variation (around 60 %) while joints made in the lab, with all the advantages of the case, do suffer extremely the climate changes (85-95 % variations). The most reasonable explanation for that relies on the fact that the two in-lab joints are produced by the same manufacturer.

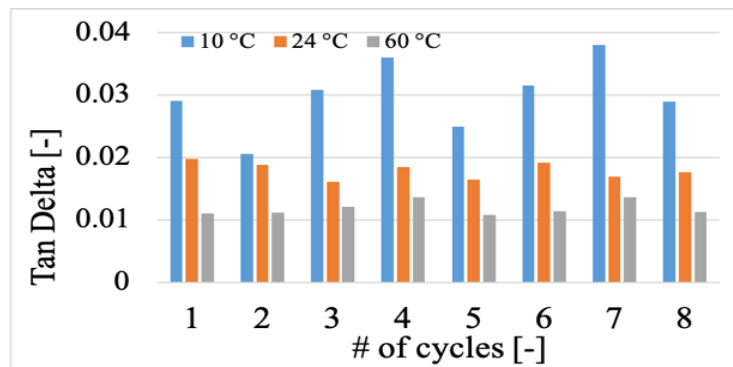


Figure 4-9. Tan delta vs. temperature measurement results for the in-field cable joint

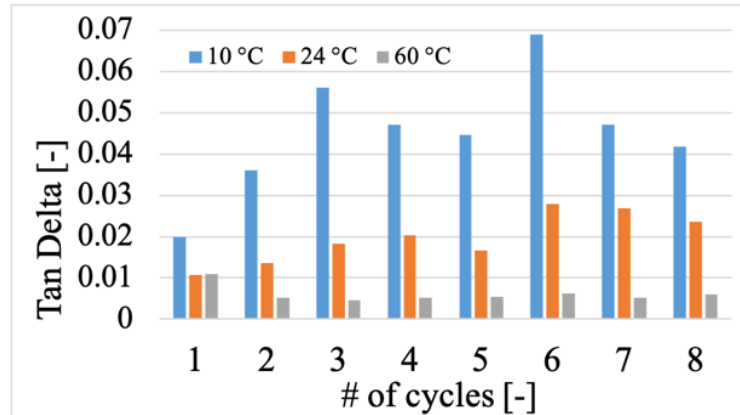


Figure 4-10. Tan delta vs. temperature measurement results for the TG 100 cable joint

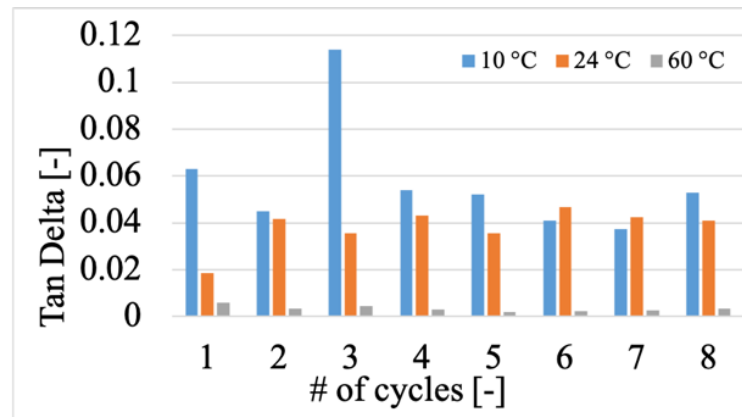


Figure 4-11. Tan delta vs. temperature measurement results for the TG 150 cable joint

Table 4-6. Tan Delta Variation between minimum and maximum Temperature applied to the Cable Joints

Sample	Tan δ [-]			Δ Tan δ [%]
	10 °C [-]	24 °C [-]	60 °C [-]	
In-field	0.03	0.01795	0.011888	60.4
TG-100	0.057425	0.038025	0.003363	94.1
TG-150	0.04515	0.01975	0.006113	86.5

One further comment can be stated concerning a hypothetical memory effect of the joints. Looking at the measured quantities in each cycle, it can be affirmed that values are almost constant. Moreover, considering that each cycle has been run immediately after the previous one, we can conclude that insulating and conductive materials used for the three joints do not present any significant hysteresis effect vs temperature. That also ensures the repeatability of the performed tests.

In the light of the aforementioned, a special attention is dedicated to the Tan Delta at high temperature, which is lower than that at low temperatures. To this purpose, Figure 4-12 shows the measured Tan Delta, for the 3 joints, at 60 °C. From the graph emerge that, except for the value of the TG 150 joint in cycle #1, the two in-lab made joints are subjected to a deep drop in the Tan Delta absolute value with respect to in-field made one. The reasons for this behavior can be reconducted to the way the joint is manufactured, but this requires further studies on the particular material used for the purpose.

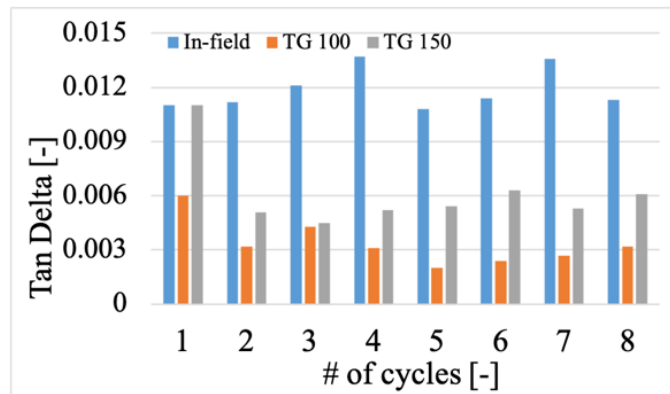


Figure 4-12. Tan delta vs. temperature measurement results for the 3 cable joints under test at 60 °C

As a final comment, it can be stated that cable joints Tan Delta depends on the ambient temperature whereas, as shown in previous section, it is independent of the Glass Transition Temperature.

4.2.4 Conclusions

To avoid power network outages, its critical components must be studied, and the causes of such outages investigated. In particular, joints are one of the frequent causes of fault in MV cable networks. With this aim, the author used an automatic test setup for the Tan Delta measurement on cable joints, which has been developed in a previous section, to assess the Tan Delta behavior vs. temperature. Tested joints came both from the field and from the manufacturers, to guarantee a complete scenario of ways to produce joints. Provided results, firstly confirm the performance of the developed setup; secondly show that cable joints Tan Delta is highly affected by temperature. In particular, it has been found that such quantity is increasing when the temperature decrease. Furthermore, an in-depth comparison between the different kinds of joints has been presented. On the overall, the setup proposed, and the obtained satisfactory results can represent a starting point for finding the reason why in higher temperatures, Tan

Delta decreases in cable joints. This analysis is carried out in next section analyzing the effect of mechanical pressure on Tan Delta measurement of cable joints. This section is published as in [25].

4.3 Effects of Mechanical Pressure on the Tangent Delta of MV Cable Joints

In light of the aforementioned analysis in previous section, this work focuses on a correlation between two crucial quantities in the cable joint fault-detection scenario: Pressure and Tan Delta (also referred to as $\text{Tan}\delta$ and Loss Factor). In detail, this section provides experimental results showing that the $\text{Tan}\delta$ in a cable joint is affected by external pressure. The pressure, which the cable joint is subjected to, could be originated either by a mechanical or a thermal stress. Both, indeed, cause a compression of the cable joint layers and consequently a $\text{Tan}\delta$ reduction. The setup used for Tan Delta measurement is the same which is designed, calibrated, and characterized in section 4-1. The present section is structured as follows: The setup short recall for the $\text{Tan}\delta$ measurement, characterized in section 4-1, The experimental test procedure, test results and discussion, and Finally, some comments and conclusion.

4.3.1 Test Setup Description

To measure Tan Delta, the setup reported in section 4-1, presented in Figure 4-2 is used. The setup is described in section 4-1-2 and it includes: a programmable power source Agilent 6813B, an isolation transformer, a step-up voltage transformer (0.1 kV/15 kV), a resistive voltage divider, a shunt resistor, a Data Acquisition Board NI9239 (DAQ) and a personal computer. The setup allows to appreciate $\text{Tan}\delta$ variations with an accuracy up to 10^{-5} starting from the voltage and current measurements on the joint under test. These two measurements are performed with the resistive divider and the shunt resistor, respectively.

In addition to this setup, other three items compose the overall equipment used in this work:

- the clamp for the pressure application. It consists in a typical Hose Clamp as the one showed in Figure 4-13, which allows to apply the desired pressure.
- a pressure sensor. It is a FujiFilm Prescale LW sensor which changes color depending on the applied pressure. Its main characteristics, including the accuracy one, are listed in Table 4-7.
- a set of three cold-shrink underground cable joints insulated with silicone rubber.



Figure 4-13. Picture of the hose clamp used to apply pressure to the cable joint under test

Table 4-7. Pressure Sensors Main Specifications

Thickness	100 um	Range of measurement	2.5 – 10 MPa
Size	270 x 12 mm	Accuracy	10 %
Measurement Temperature	25-35 °C		

One cable joint is made by one manufacturer and installed in-field by a DSO operator on an EPR cable. In detail, after a fault occurred the cable joint has been installed and immediately after removed and brought to the lab. The other two joints are made by another manufacturer in a laboratory environment. The joint has been installed on two one-meter portion of XLPE cable. The last two cable joints are manufactured with different Glass Transition Temperatures (TG), 100 and 150 °C. Consequently, from here on out they are referred as TG-100 and TG-150, respectively.

4.3.2 Test procedure

The test procedure is composed of two phases: Tan Delta measurement test, and pressure test. The first test is described in detailed in section 4-1-4. Instead, the pressure test will be described in detail in this section.

Moving to the $\text{Tan}\delta$ sources analysis, the cable joint has been modelled using finite-element software, as shown in Figure 4-14. Afterwards, an actual operational condition at 10 kV has been run to assess the electrical stress that it is subjected to. This can be seen in Figure 4-15, where the simulation output has been depicted. From it, can be distinguished the two electric field components cause of the $\text{Tan}\delta$: the perpendicular one E_P and the tangential one E_T , with respect to the longitudinal axes of the cable joint. In particular, E_P crosses all the joint layers, while E_T interests its interfacial surfaces.

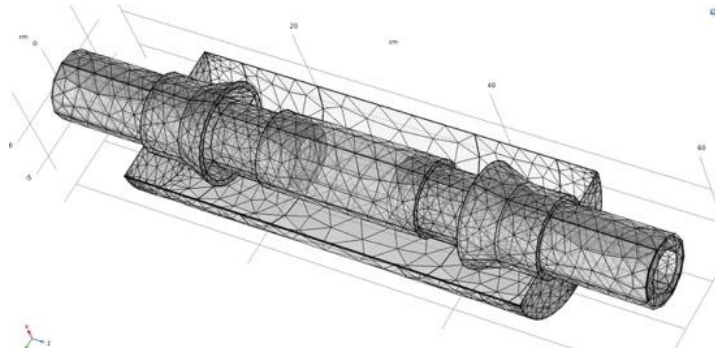


Figure 4-14. Picture of the simulated Cable Joint using finite-element software

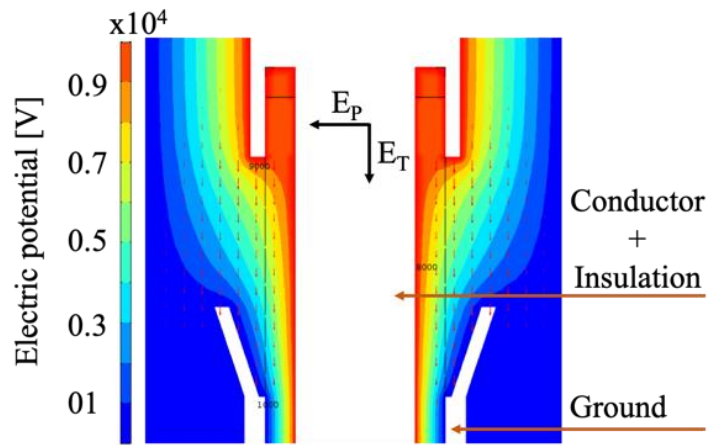


Figure 4-15. Electric potential distribution and electric field components of a simulated Cable Joint

4.3.2.1 Pressure Test

The test aims at verifying the author's hypothesis of a $\text{Tan}\delta$ reduction when the cable joint is subjected to an external pressure. Therefore, the test consisted of three different stages. Firstly, the $\text{Tan}\delta$ has been measured in absence of external pressure (Test A). Afterwards, $\text{Tan}\delta$ has been measured during the application of 0.8 MPa (Test B), with the Hose Clamp, at both cable joint terminals as clarified in Figure 4-16. Finally, $\text{Tan}\delta$ has been measured, without any external pressure, after 8 hours from the previous test (Test C). All three tests are performed in the room temperature of 24 °C. For each test, performed on all the three joints under test, 1000 measurements have been acquired. Hence, $\text{Tan}\delta$ mean value and standard deviation of the mean have been computed and listed in the following Section.

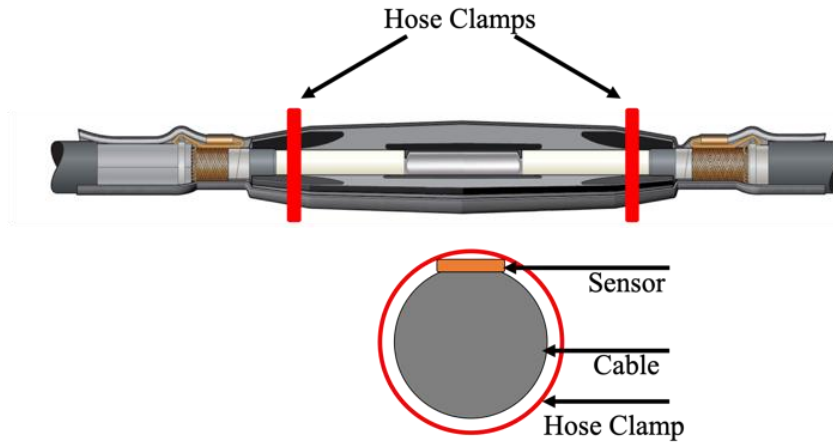


Figure 4-16. Schematic representation of the pressure application and measurement

4.3.3 Test Results

All tests results are listed in Table 4-8. It contains, for the three cable-joints under test, mean value and standard deviation of the mean for the three tests A, B and C, previously described.

Table 4-8. Tan Delta results during the Pressure Test for the Cable Joints under test

Pressure	In-field		TG-100		TG-150	
	$Tan\delta$ [-]	$\sigma_{Tan\delta}$ [-]	$Tan\delta$ [-]	$\sigma_{Tan\delta}$ [-]	$Tan\delta$ [-]	$\sigma_{Tan\delta}$ [-]
A	0.0135	0.0006	0.0231	0.0006	0.0261	0.0006
B	0.0088	0.0009	0.0141	0.0005	0.0181	0.0006
C	0.0072	0.0009	0.0180	0.0005	0.0207	0.0006

Figure 4-17 plots the obtained results. It clearly emerges that $Tan\delta$ value drops, for all the cable-joints, when the external pressure is applied. This can be explained by the fact that the pressure is reducing the interfacial leakage between the XLPE/EPR insulation of the cable and the joint silicon rubber, turning into a lower resistive leakage current. Moreover, the pressure is affecting singularly each material, hence they are facing an intrinsic reduction of $Tan\delta$, confirming the findings presented in [26] [27]. Regarding Test C, it has been observed that after the pressure removal, $Tan\delta$ returned almost to its original value. This is true only for the in-laboratory installed joints. As a matter of fact, the in-field installed joint shows an opposite behavior: its $Tan\delta$ continued to decrease also after the pressure removal. For the reason it can be explained that it is associated to the different materials used by the two manufacturers and the different cable insulation of the objects under test.

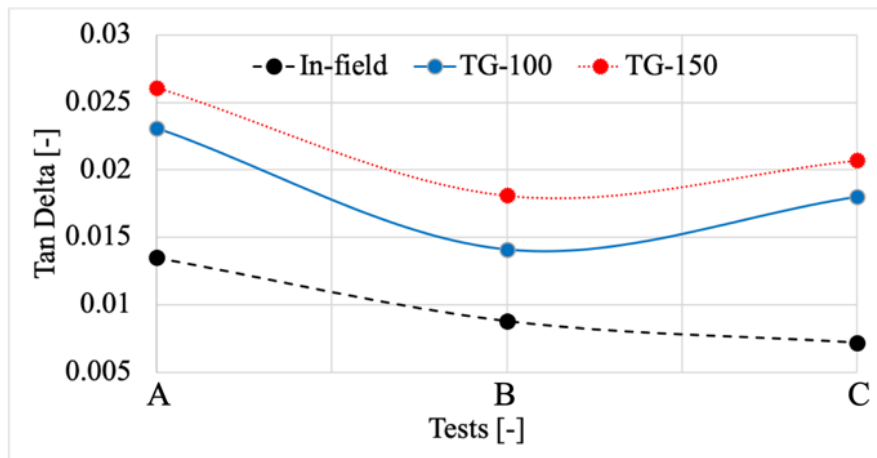


Figure 4-17. Tan delta measurement results for all the three pressure tests

4.3.4 Conclusions

MV underground cable networks are fundamental to supply domestic and MV industrial loads. The most critical cable accessories which are exposed to failure are the cable terminations and the cable joints. As the cable joints are undergrounded, the maintenance procedure is time consuming considering the fault location detection, digging and joint making. $\tan\delta$ and Partial Discharge measurements are two of the most important diagnostic tests on cable joints. In literature, different insulating material has been analyzed in terms of $\tan\delta$ versus difference influence quantity such as temperature, pressure, humidity, etc. In this section, the previously designed setup has been used for Tan Delta measurement vs. applied pressure on the overall cable joint system. It has been shown that by increasing the pressure between joint insulating material (Silicon Rubber) and cable insulating material Tan Delta decreases, yielding to an extension of the overall cable joint life.

Up to now, we know that in cable joints Tan Delta decreases when temperature increases. On the other hand, Tan delta decreases when the interfacial pressure (pressure in the interface between joint and cable insulating material) increase. This represents the loop shown in Figure 4-18.

To conclude the causes and effects for the relation between Tan Delta, Temperature, and interfacial pressure, it is only remaining to design a measurement setup to measure the interfacial pressure vs. temperature. As the finishing point of cable joint diagnosis, such setup is been designed, characterized and calibrated in next section. This section in published in [28].

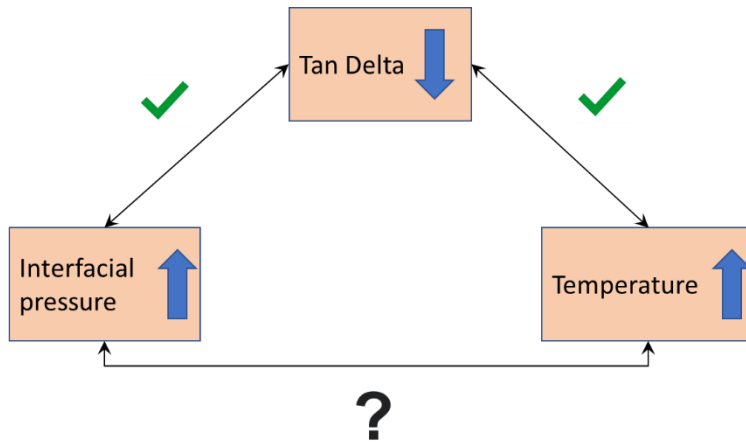


Figure 4-18. Cause and Effect loop for the relation between Tan Delta, Temperature, and Interfacial Pressure in cable joints

4.4 Test Bed Characterization for the Interfacial Pressure vs. Thermal cycle Measurements in MV Cable Joints

Medium Voltage (MV) cable joints have long been investigated due to the key role they play in underground power lines. Their careful design and installation are critical to ensuring good electrical power transmission in cable systems, effective repair, and installation of new lines. Being the weakest links in power lines, MV cable joints are responsible for most faults, causing detrimental consequences for customers and Distributed System Operators (DSOs) or utilities.

To reduce the occurrence of failures in MV cable joints, it is of major importance to understand the mechanisms leading to loss of insulation. A good insulation depends on several factors, such as, for a certain voltage level, interface pressure and surface smoothness, materials, manufacturing and installation. A given type of joint must exhibit a good thermal performance [29] [30] [31] since this capability is related to cable ampacity. Different sensing systems have been proposed for continuous temperature monitoring in cable joints [32] [33] [34] [35] and to be able to plan predictive maintenance.

Whilst the temperature has been recognized as a major cause of cable joint failure, more recently other parameters have been investigated, namely the tangent delta ($\text{Tan}\delta$), interfacial pressure, and Partial Discharge (PD) level. In section 4-1 an experimental setup is proposed for the estimation of tangent delta at ambient temperature. The same setup is then used to perform measurements in the 10-60 °C temperature range which is described in section 4-2. The experiments demonstrated a relationship between the temperature and the tangent delta, affecting the cable joint service life.

The pressure between the insulating elements and the cable joint is also believed to affect the insulation effectiveness provided by the cable joint. The selection of materials plays a relevant role in this respect [36]. A method is available in literature to calculate and simulate the surface pressure [37]. The correlation between the interfacial pressure and tangent delta has been explored in [28]. The variation of the interfacial pressure with the ambient temperature was also investigated [38].

As for the PD, they are considered by several experts an effective method to assess the “healthy” status of the cable joints. Therefore, literature provides a high number of studies on this topic. For example, new PD extraction and analysis methods are presented in [39] and [40], while an on-line measurement setup is described in [41].

In this section, the effect of long-term temperature cycles on the interfacial pressure of cable joints is studied. The obtained results are assessed from two points of view: the absolute value of the measured pressure and the overall effect on the cable joint and its ageing. From the results, compared also with the current literature, it is highlighted how the thermal cycles negatively affect the lifecycle of the cable joint.

The present section is structured as follows: first, the measurement setup and the details of its elements are described. Then the experimental tests are described, while the next section is dedicated to the results analysis. Finally, conclusions are stated to wrap the topic.

4.4.1 Measurement Setup

4.4.1.1 Overview

The measurement setup developed for the pressure vs. temperature tests on cable joints consists of:

- A thermostatic chamber with temperature ranging from 5 °C to 60 °C.
- Two cable joints (A and B for the sake of privacy) installed on pieces of MV cables as described in the following.
- Four pressure sensors (two for each cable joint) Flexi Force Standard Model HT201, and their quick-start board for the signal conditioning.
- NI Data acquisition board (DAQ).
- A two channels Chauvin Arnoux CA863 contact thermometer, to measure the temperature on the cable joints and of the thermostatic chamber.

- A simple DC power supply to feed the quick-start board of the pressure sensors.
- A personal computer and the LabView software to manage the acquired data.

The main elements of the setup as explained above, are the thermostatic chamber, capable of varying the temperature in the range 5 to 60 °C, and the cable joint under test (CUT). The CUTs are described in detail in next subsections. The setup is completed with (i) a Chauvin Arnoux CA863 contact thermometer to assess the temperature of the CUT and of the thermostatic chamber. The CA863 is a two channels device with operating temperature in the -50 - +1300 °C range, and it features a resolution and an accuracy of 0.1 °C and ± 0.3 % of the reading, respectively. (ii) a 24-bit National Instrument NI9239 Data Acquisition board (DAQ) featuring an input range of ± 10 V, a gain error and offset error of 0.03% and 0.008%, respectively. (iii) the sensing part of the setup, 4 pressure sensors Flexi Force Standard Model HT201. Their main characteristics are: thickness of 0.203 mm, linearity up to 3 MPa, temperature drift of 0.088 %/°C, and a non-linearity error of 3 % of the full scale. A simple schematic of the measurement setup is depicted in Figure 4-19.

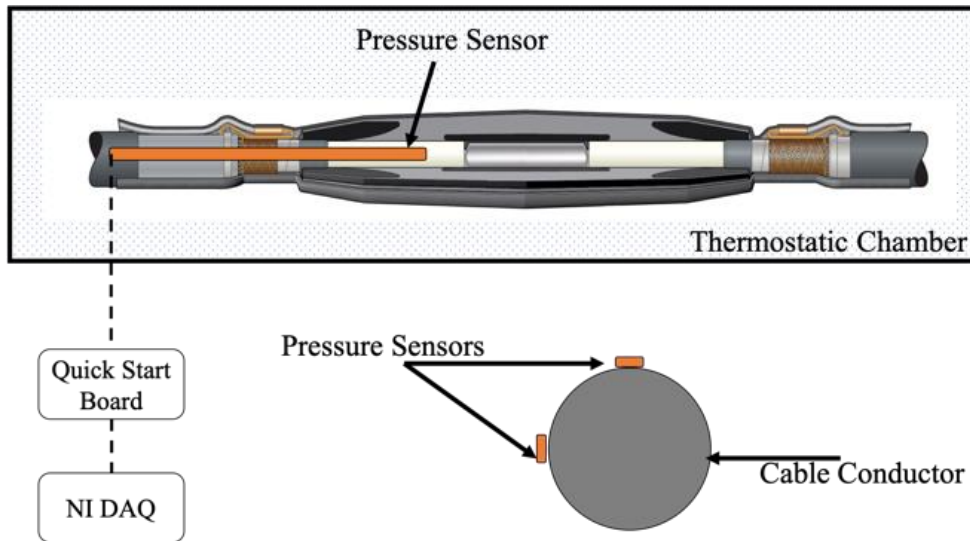


Figure 4-19. Schematic of the measurement setup and pressure sensors positioning

4.4.1.2 Cable Joints

For the experimental tests two cable joints built by two different manufacturers have been used. From here on now they will be referred as A and B for privacy reasons. The cable joints under test are

both cold-shrinkable joints for MV cables. They have been installed, in laboratory environment, on two pieces of 130 mm² MV, XLPE insulated cables. The CUT is composed of:

1. Metallic connector holding the two cable conductors.
2. Silicon Rubber (SR) as main insulating material covering the metallic connector and the XLPE insulating part of the cable. This silicon layer is covered by semi-conductive material.
3. A metallic meshed shielding covering the silicon rubber, which is used to maintain the ground electrical connection between the two portions of jointed cables.
4. The external cold-shrinkable layer.

The detailed cable joint parts are highlighted in Figure 4-20.

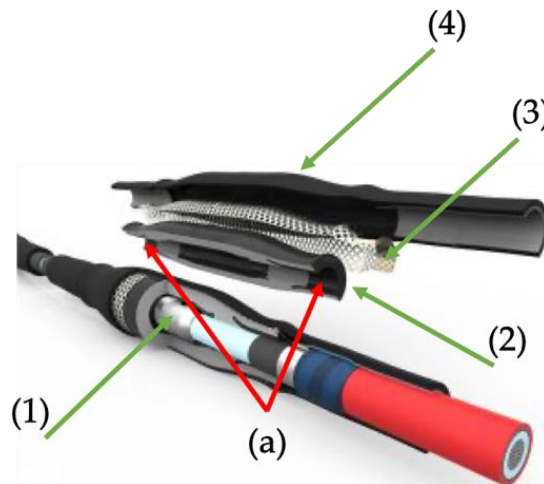


Figure 4-20. Cable joint structure with particular attention to the parts of interest

A few important comments can be made looking at Figure 4-20. Firstly, underneath the silicon rubber (2) a semi-conductive layer is placed on the metallic conductor to obtain a homogeneous electric field in that area. Secondly, at the two ends of the joint, a stress control layer, typically made of mastics, is placed over the XLPE insulation of the cable to modify gradually the electric field distribution (see (a), Figure 4-20).

In the CUT, the metallic meshed shielding has not been connected to the portion of cables shielding to allow the pressure sensors installation. However, neither voltages nor current have been applied for the following tests, hence the structure of the CUT has not been altered.

4.4.1.3 Pressure Sensors and Conditioning Board

Several types of pressure sensors are used in academia and industry for a variety of purposes. Such sensors are typically classified according to two criteria: the pressure measurement type, and the sensing principle implemented in the sensor.

Starting from the measurement type, three main categories can be described:

- Absolute measurement. It means that the reference point is the vacuum; therefore, one side of the sensor itself is dedicated to it, while the other side is faced to the mean to be measured.
- Gauge measurement. This type of sensor shares the structure with the previous one, but it uses as reference point the atmosphere. Hence, when using this kind of sensors, the operator should always check that the air can flow inside the side of the sensor dedicated to the atmosphere.
- Differential measurement. According to their name, these sensors measure the pressure between two arbitrary points.

From the description, it is clear how the types of sensors share the basic principles and then each of the three has been developed to answer specific requirements of measurement.

As for the sensing principle, the most used technologies are the resistive, the capacitive, the optical, and the piezoelectric. The resistive and the capacitive type have the same working principle underlying the operation of sensor; in fact, the pressure induces a change of resistance/capacitance. The piezoelectric exploits the generation of charge to detect the pressure change in the sensor. Finally, interferometry principle is used in optical sensor to appreciate pressure variations when the fiber optic is stressed.

In light of the different available technologies, author selected an enhanced piezo-resistive force sensor adaptable to extreme temperatures ($-40\text{ }^{\circ}\text{C}$ to $204\text{ }^{\circ}\text{C}$) and capable of linear measurements of pressures up to 3 MPa. The sensor is depicted in Figure 4-21. In addition, the adopted technology allows to appreciate little variations of pressure (in a wide range of pressures), which is a key-feature for the cable joint monitoring. One possible disadvantage of the piezo resistive sensor is the fact that they could be temperature dependent. However, the characterization procedure and the manufacturer specifications allowed to include the output variation due to the temperature.

A consideration is about the geometry of the system. The Flexi Force sensor has a thickness of 0.203 mm that makes it suitable for installation inside the CUTs without significantly changing their geometry; hence, without interfering with the effect of temperature on the cable joints.

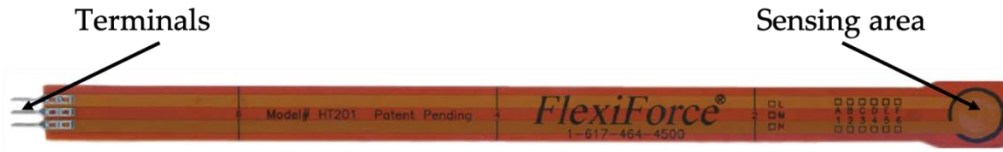


Figure 4-21. Picture of the adopted pressure sensor

As a matter of fact, the requirement was to have a sensor installable between the XLPE insulation of the cable and CUT silicon rubber without modifying the overall geometry. The specifications for sensors are collected in Table 4-9.

Table 4-9. Pressure Sensor main Specifications

Specification	Values
Width	14 mm
Length	191 mm
Thickness	0.203 mm
Sensing Area Diameter	9.53 mm
Non-linearity error	±3 % FS
Drift	3.3% per logarithmic time scale
Temperature Range	(-40 to 204) °C
Temperature Drift	0.16 % / °F
Linear Pressure Range	Up to 3 MPa

The piezoresistive sensors have a variable resistance proportional to the force applied to the sensing area. The resistance is linear, according to the manufacturer data sheet, up to 3 MPa pressure. Afterward, the nonlinear range starts up to maximum measurable value which is 30 MPa. However, the linear range is sufficiently large to contain the pressure test measurement values.

The pressure sensors are used together with the Quick Start board to condition their output signal. The board consists of an amplifier circuit with 5 to 9 Vdc supplying voltage which leads to a 0 to 5 Vdc output voltage. Such output is the result of a two-steps process performed by the board. First, it computes the sensors output value using:

$$V_{o1} = \left(1 + \frac{R_{pot}}{R_{sensor}}\right) * V_{ref} \quad (4-10)$$

where V_{ref} is the voltage output of the sensor when it is unloaded. R_{pot} and R_{sensor} are the resistance of the adjustable potentiometer, mounted on the board, and of the sensor itself, respectively. The second step consists in the offset removal. It is done by applying:

$$V_{o2} = (1.107) * V_{o1} - V_{ref} \quad (4-11)$$

Therefore, the output voltage of the board, before applying any other correction, is represented by V_{o2} .

4.4.2 Description of the Experimental Tests

The aim of this work, as introduced before, is to assess the effect of thermal cycles on the pressure at the interfacial surface between XLPE and SR of MV cable joints. To this purpose, the two CUTs have been tested as follows. For 12 days the pressure measured by the 4 sensors has been daily collected at two temperature: room temperature (24 °C) and at 60 °C. This last temperature has been kept for 4 hours to reach the thermal stability of the cable joint. After the collection of the measurements, the CUTs have been left naturally cooling at 24 °C until the next day set of measurements. To ensure the thermal stability of the CUT, the measurements have been performed only when the thermocouple gauging the air temperature and the one inserted in the joint have the same value (after 4 hours). For all tests, 250 measurements of pressure have been acquired from each sensor installed in the CUT. In addition, pressure has been collected, for both CUTs, at the same time to guarantee the same temperature conditions in all tests.

What above described represents the first part of the experimental measurements on the CUTs. After the 12 days, the CUTs have been kept at room temperature for 43 days without performing any pressure test. Then, another measurement at room temperature has been performed to understand the behavior of the CUTs. Such a measurement has been repeated again after 31 and 49 days, always at room temperature (24 °C).

To better clarify the overall experimental procedure, in Figure 4-22 the temperatures set during the tests have been plotted together with the time window of the entire measurement campaign. In the graph, the second part of the tests, which is at 24 °C without changes, has been compressed for the sake of clarity.

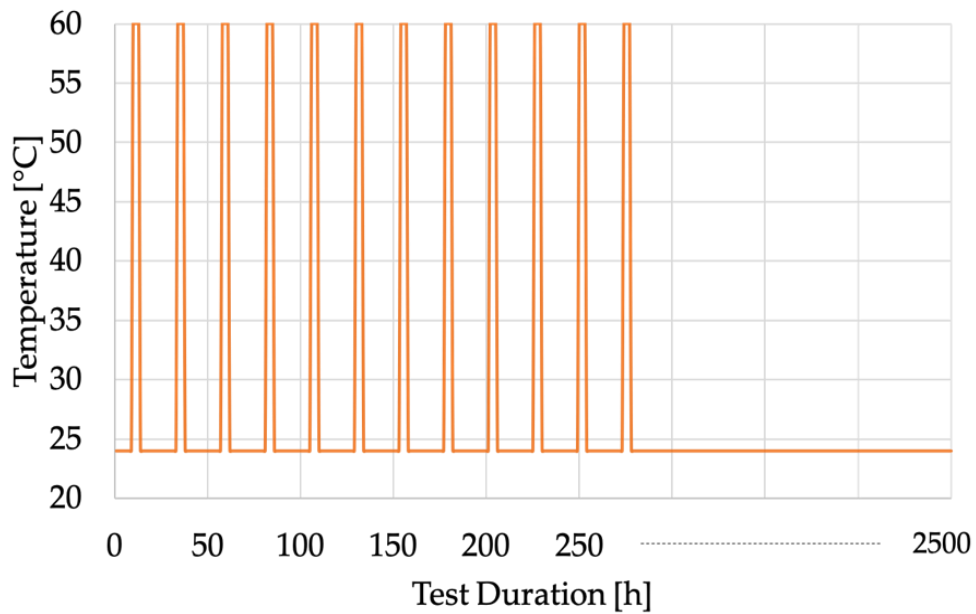


Figure 4-22. Temperature vs. duration of the tests on the CUTs

Overall, the experimental campaign on the CUTs lasted more than 3 months. Such a duration has been chosen to assess the interfacial pressure behavior of the CUTs when subjected to thermal cycles. It is worth to highlight that, for the duration of the tests, the CUTs have not been moved at all, to replicate the actual condition of the grid. In fact, MV cables, buried underground, are not subjected to any displacement in their life cycle (except for a fault happening on the portion of cable considered).

4.4.3 Results and Discussion

4.4.3.1 Measurement Results

The pressure measurements collected in the 3-months period are listed in Table 4-10. It contains on the first column the list of days when the measurements have been performed and, for each temperature,

the mean value of the acquired pressures (250 each). As mentioned, each CUT mounts 2 pressure sensors; hence they have been distinguished as A_1 and A_2 for the CUT A, and B_1 and B_2 for the CUT B.

Table 4-10. List of all pressure measurement results for the 2 CUTs

Days	Pressure [kPa]							
	24 °C				60 °C			
	A_1	A_2	B_1	B_2	A_1	A_2	B_1	B_2
1	750	1210	196	174	892	1473	256	205
2	729	1218	217	176	893	1471	276	209
3	735	1213	210	175	901	1482	249	215
4	747	1194	215	188	915	1500	281	216
5	743	1256	227	190	914	1502	273	224
6	748	1260	238	193	1191	1508	313	223
7	900	1267	248	195	1104	1523	308	228
8	872	1236	251	192	1075	1512	307	231
9	874	1273	258	195	1072	1520	309	233
10	870	1279	264	202	1064	1520	306	233
11	870	1273	267	199	1060	1513	311	235
12	866	1283	271	204	1058	1528	313	237
55	864	1278	206	188	-	-	-	-
86	875	1294	225	198	-	-	-	-
104	883	1303	231	203	-	-	-	-

The pressure measurement results are accurate for the purpose of the work. In fact, the overall uncertainty affecting the pressure measurement is 1 kPa, and therefore predominant compared to the calculated standard deviation of the mean, which has been neglected and not reported here (between 0.02 and 0.04 kPa). This last range of values for the standard deviation has been confirmed for the entire duration of the test; therefore, the stability and repeatability over the time is ensured.

From Table 4-10, it is worth to highlight two interesting comments: one about the two CUTs, and one about the two sensors of a single CUT. First, comparing the CUTs, a difference between the measured pressures is evident. Such a difference is due to the different manufacturers' ways of preparing the cable joints. Unfortunately, the manufacturers do not provide any details on the interfacial pressure of their joints; hence, the only source for such an information is from a measurement campaign, as it has been done in this work.

The second comment concerns the two sensors inside the single CUT; in fact, slightly different values have been collected in both CUTs. This effect is reasonable considering the 90° angle between two sensors of the same CUT (see Figure 4-23); as a matter of fact, the gravity and the positioning of the CUT over the working surface are affecting the measured pressure.

However, in this specific work the attention is not given to the absolute value of the pressure but on its variation vs. temperature.

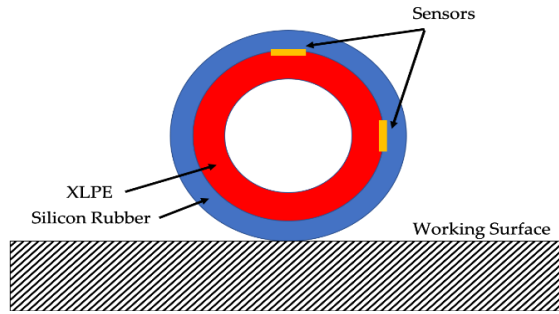


Figure 4-23. Positioning of the two sensors inside the CUT and of the CUT itself

To increase the readability of the results and to provide further comments on them, the pressure measurements have been plotted in Figure 4-24 and Figure 4-25 for the CUT A and B, respectively.

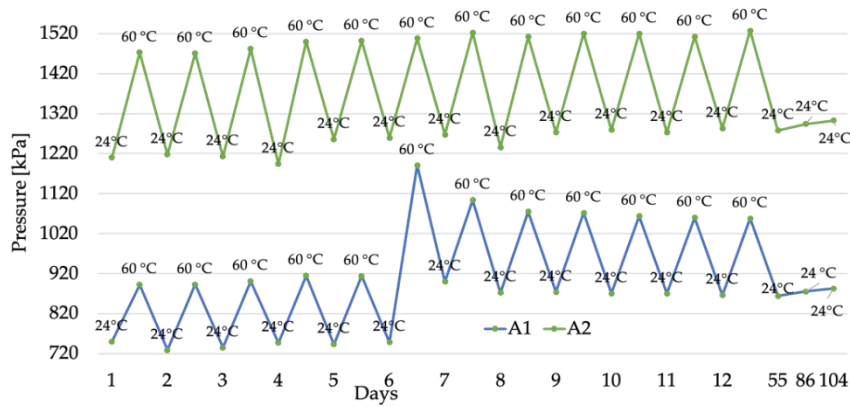


Figure 4-24. Pressure measurement results for CUT A, sensors A₁ and A₂

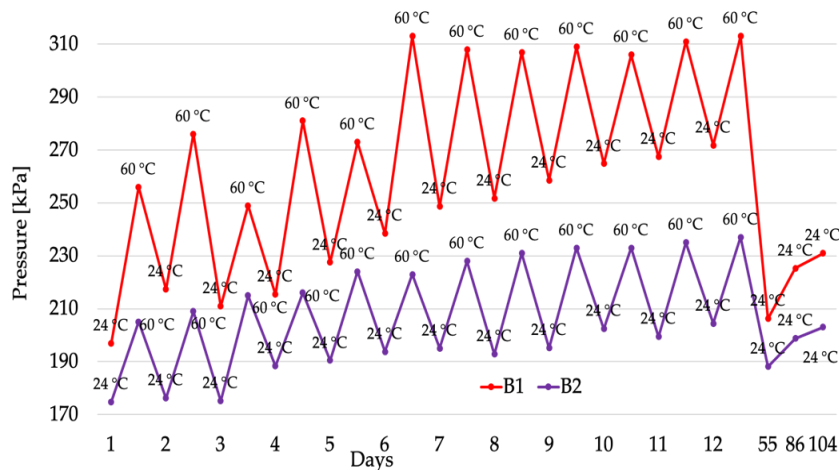


Figure 4-25. Pressure measurement results for CUT B, sensors B₁ and B₂

After the specific comments on the absolute value of the results, it is important now to highlight the trend of the pressure in the two CUTs. A general statement is that the thermal cycles have a non-negligible effect on the interfacial pressure of the cable joints. All 4 sensors, hence both joints, experience an increase of the pressure as the number of cycles increase. If this phenomenon is clear for sensors A_1 , B_1 , and B_2 , from the graph it is less appreciable for sensor A_2 . To this purpose, the percentage variation between day 1 and day 12 has been calculated for the 4 sensors. The results are 15.5, 6.0, 38.0, and 16.9% for A_1 , A_2 , B_1 , and B_2 , respectively.

Overall, the first 12-days temperature cycles stressed the CUTs causing an interfacial pressure variation up to 40 %. Such a pressure variation is critical when looking at the second-phase test results. In fact, after 43 days the room-temperature measured pressure dropped significantly compared to the one collected in the 12-days period. However, the detected drop is not sufficient to restore the interfacial pressure of the joint to the values obtained before the thermal cycles. In detail, percentage variations with respect of the first pressure measured at room temperature are 15.2, 5.6, 4.7, and 7.6 %, for A_1 , A_2 , B_1 , and B_2 , respectively.

The effects of the thermal cycles are persistent even after more than 80 days after their end. As it is evident from Fig. 6 and 7, the pressure remains quite stable in all tests; except for CUT B , which exhibits a slight pressure increase. Therefore, it can be concluded that the combination of the thermal cycles and the memory effect, of the materials adopted to build a cable joint, cause a variation of the mechanical properties of the joint itself.

4.4.3.2 Discussion & Comparison

What has been obtained in Table 4-10 can be described starting from the expression of the expansion that the material is suffering when subjected to temperature variations:

$$\Delta r_x = \alpha_x r_{0x} \Delta T_x \quad (4-12)$$

$$\Delta r_s = \alpha_s r_{0s} \Delta T_s \quad (4-13)$$

For the sake of simplicity, (4-12) and (4-13) refer to the linear expansion, but the concept can be extended also for the volumetric expansion. In (4-12) and (4-13), the subscript x and s refer to XLPE and SR, respectively. Such subscripts have been associated to the temperature variation experienced by the materials ΔT , the initial radius of both insulating materials r_0 , the thermal expansion coefficient α , and finally the radius variation caused by the temperature Δr .

Considering that the pressure increases with the temperature, the terms in (4-12) and (4-13) must be analyzed. Firstly, it can be assumed that $\Delta T_x = \Delta T_s = \Delta T$ due to the measurement process. In fact, the thermocouple has been placed at the interface between XLPE and SR and the measurements have been performed only when the thermal stability had been reached (as detailed above). Therefore, the contribute of the temperature to the thermal expansion of the insulation materials can be considered the same for both. Secondly, in terms of radius, XLPE and SR are laying one over the other; therefore, their layers subjected to the expansion can be considered equal.

Hence, it can be observed that the expansion in outer and inner direction (with respect to the cross section of the cable) has a similar contribution for both XLPE and SR. What differentiates (4-12) and (4-13) is simply the thermal coefficient of the two materials. In light of these assumption, and dividing (4-12) by (4-13):

$$\frac{\Delta r_x}{\Delta r_s} = \frac{\alpha_x}{\alpha_s} \quad (4-14)$$

it can be explained the reasons of the increase of pressure in the interfacial surface of the joint. Typically, α_x and α_s vary in the 4-to-7 · 10⁻⁴ 1/°C range, depending on the particular materials and by their cross-linking level [42] adopted by each manufacturer. Therefore, the pressure variation measured in the test can provide different results if $\alpha_x \lesseqgtr \alpha_s$ and from their absolute value. In particular, the different percentages in pressure variation can be associated to different values of α related to the manufacturers' materials.

As a final comment, the above discussion assumes that α is independent of the temperature. Such assumption can be considered relevant in this work due to the level of temperature used in the tests (60 °C), which is far lower from the glass transition temperature of XLPE (typically around 130 °C) and SR (90 °C, provided by the manufacturers), hence far from values at which α starts to experience the effect of temperature [43].

4.4.4 Conclusion

The causes of fault in MV electrical assets, and in particular in cable joints, is a current topic tackled in literature. To this purpose, the author addressed in this work one of the main influence quantities affecting the joints' operational life, i.e. the temperature. For three months the two cables joints under test have been subjected to thermal cycles. The obtained results showed that there is a strong relationship between the interfacial pressure of the insulating materials and the room temperature. When subjected to thermal cycles, the cable joint will experience an increase of its interfacial pressure between XLPE and

SR. Such an effect causes, individually assessed, an apparent increase of the dielectric properties of the materials. However, looking at the results from a wider point of view, it can be concluded that the temperature effect on the pressure causes an unwanted variation. In detail, a pressure change increases the generation of voids and weak spots in the insulating materials of the cable joints, and therefore a shortening of the cable joint lifecycle, causing damages to the DSOs and to their customers.

As the correlation between Tan Delta, Temperature, and Interfacial pressure was concerned from the beginning of the present chapter, Figure 4-26 (in correlation with Figure 4-18. Cause and Effect loop for the relation between Tan Delta, Temperature, and Interfacial Pressure in cable joints) shows the closure of the cause and effect loop by proofing the whole concept. [44], [45] and [38] are the published papers regarding this section.

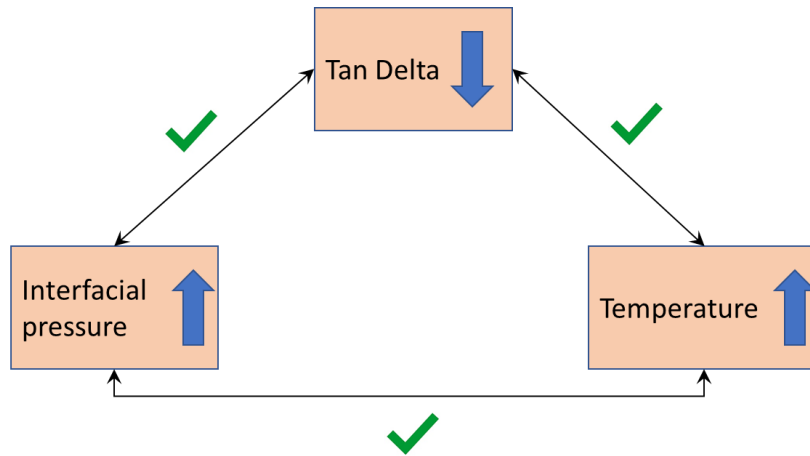


Figure 4-26. Cause and Effect loop for the relation between Tan Delta, Temperature, and Interfacial Pressure in cable joints

5 Measurement Model for Inductive Current Transformers

Despite the introduction of the new generation of Low-Power Instrument Transformer (LPIT), the classical Inductive ones (ITs) are still wide adopted. As a matter of fact, both inductive current and voltage transformers (CTs and VTs) [46] [4] [5] are reliable measurement instrument, in particular for Distribution Networks (DNs). Distribution System Operators (DSOs) and electrical utilities are moving towards the adoption of LPIT but still they prefer the ITs for a delicate aspect as the metering for pricing. To guarantee a high accuracy for such a measurement, a transformer should be known and tested in all its peculiarities.

As far as the internal behavior of the ITs is concerned, their modelling has always been a paramount and critical topic. To this purpose, this section aims at enhancing the knowledge of the core losses behavior vs. two quantities: the load current and the temperature.

Such behavior has not been tackled in the literature yet; despite that several papers can be found on the ITs modelling. For example, core saturation has been studied in [47], whereas the typical linear-model approach is described in [48] and [49]. In [50] and [51] new approaches for their modelling and their design are presented, respectively. Power quality is such an important topic that has been included in different ITs modelling studies [52] [53] [54]. Finally, another way to tackle the critical aspects of an IT model is to compensate all its non-linearities and losses with a posteriori analysis [55] [56].

In this section two works are done on inductive current transformers for the modelling. One for CT modelling by core parameters extraction and their variation vs. temperature and loading condition, and the second for ratio and phase error prediction under different temperature and loading condition along a ratio and phase error decomposition to analyze the filtering behavior of the CT in different temperatures and loading conditions.

5.1 Inductive Current Transformer Core Parameters Behaviour vs. Temperature Under Different Working Conditions

In this section, by using a developed test setup, different measurements have been performed on the CT under test (TUT) to calculate its series and parallel impedances. As it is well known, the main parameters of CTs, which affect its operation, are the series ones containing (i) primary and secondary equivalent leakage reactance X_{eq} , (ii) primary and secondary equivalent copper loss resistances R_{eq} , and the shunt parameters (iii): magnetizing reactance X_m and core losses (eddy currents and hysteresis)

resistance R_w . Then, working conditions and temperature have been varied to assess the shunt impedance behavior. This way, further studies could focus on their effect on the overall accuracy of the CTs.

The present section is structured as follows: first part describes the setup adopted to test the Medium Voltage (MV) CT. The performed tests are detailed in next part, while their results are showed and discussed next. Finally, the last part of the section presents some conclusions.

5.1.1 Test Setup

The circuit diagram shown in Figure 5-1 schematizes the general setup adopted for the measurements on the CT. It includes:

a programmable power source Agilent 6813B, which features up to 300 V RMS, 1750 VA from DC to 1 kHz. Which feeds:

- a 10-ratio step-down transformer used to isolate the source and to increase the current to the TUT rated value.
- The 0.5 accuracy class CT under test. It features ratio of 20/5 A, 10 VA rated power and rated frequency of 50 Hz.
- Two shunt resistors to measure the primary and the secondary currents, $R_1 = 1\text{ m}\Omega$ and $R_2 = 10\text{ m}\Omega$, respectively.
- A pure resistive load used as rated burden R_B .
- Two accurate resistive dividers to measure the primary and secondary voltages, both with nominal ratio equals to 11 (k_1 and k_2 , respectively).
- The thermal chamber, it contains only the TUT and it allows to reach 60 °C.
- Data Acquisition Board (DAQ) NI-9239 equipped with 4 synchronized channels and which main characteristics are summarized in Table 5-1.
- Personal Computer to analyze all the DAQ-acquired quantities.

Table 5-1. NI-9239 main features

Architecture	24-bit	Max input signal	$\pm 10\text{ V}$
Sample rate	50 kS/s/ch	Simultaneous channels	YES
ADC	Delta Sigma	Temperature range	-40 to +70 °C
Gain Error	0.03 %	Offset Error	0.008 %

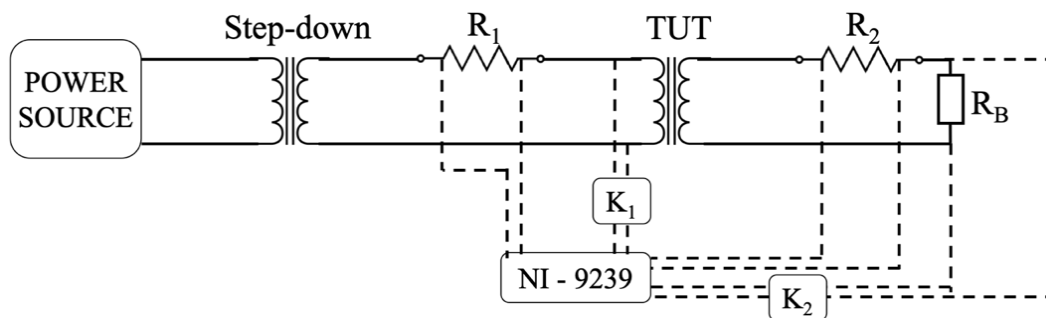


Figure 5-1. Circuit diagram of the measurement setup adopted for the tests

5.1.2 Experimental Tests Procedure

Before running the main tests aim of this work, the components of the proposed setup have been characterized. Hence, 1000 measurements have been acquired after injecting 20 A, 5 A, 5 A to R_1 , R_2 , and R_B , respectively. The injected values, by using the Fluke calibrator 6105a (Table 5-2 summarizes its main features), represent the ones the components will be subjected to during the main tests. With the same criterion, 3 V has been applied to the two resistive dividers to compute their ratios (k_1 and k_2). Results of the characterization tests are reported in Table 5-3 in terms of mean value and standard deviation of the mean σ_m of resistance and of the dividers ratio. As it can be seen from the Table, all the components are known with a high accuracy level. As for R_B , the required value was 0.4 Ω according to the ratio rated voltage (2 V) overrated current (5 A). The measured one instead is slightly different, however, from [4] it is possible to extend the rated burden value if the CT remains in its accuracy class.

Table 5-2. Fluke 6105a main features

At power frequency conditions	
Range [V]	Accuracy (ppm + mV)
1 – 23	42 + 0.2
70 – 1008	60 + 10
Range [A]	Accuracy (% of output + % of range)
120	0.009 + 0.002
Frequency	Accuracy (ppm)
Full range	50

Table 5-3. Components Characterization results

Item	Mean value	σ_m
R_1 [Ω]	0.0010250	$3 \cdot 10^{-7}$
R_2 [Ω]	0.010035	$1 \cdot 10^{-6}$
k_1 [-]	11.00215	$4 \cdot 10^{-5}$
k_2 [-]	11.00110	$5 \cdot 10^{-5}$
R_B [Ω]	0.52571	$7 \cdot 10^{-5}$

5.1.2.1 Rated Condition Test

The first test performed on the setup depicted in Figure 5-1 has the aim of computing ratio and phase error at rated conditions of the TUT at 24°C and 60 °C. Hence, the power source was adjusted to provide an equivalent current of 20 A when the rated burden is connected. Then, 1000 values of primary and secondary quantities (current and voltages) have been acquired. Consequently, ratio and phase error (ε and φ) have been computed, for both the operating temperatures, as:

$$\varepsilon = \frac{kI_2 - I_1}{I_1} \quad (5-1)$$

$$\varphi = \hat{I}_2 - \hat{I}_1 \quad (5-2)$$

where k is the nominal ratio of the CT, I_1 and I_2 are the RMS values of the primary and secondary currents, respectively. In (5-2), \hat{I}_1 and \hat{I}_2 are the phases of the primary and secondary current phasors.

5.1.2.2 Short Circuit Test

The Short Circuit (SC) test is done in the same way as for power transformers. Figure 5-2 shows the adopted setup. While the secondary terminals are short circuited, on the primary side the voltage is increased, and the current monitored till it reaches the test value. For this test the measured quantities are: primary current phasor \bar{I}_1 , primary voltage phasor \bar{V}_1 and phase displacement θ_1 between them. SC test has been performed at 24 °C and 60 °C under different primary current conditions (100 %, 75 %, 50 %, and 25 % of the rated current).

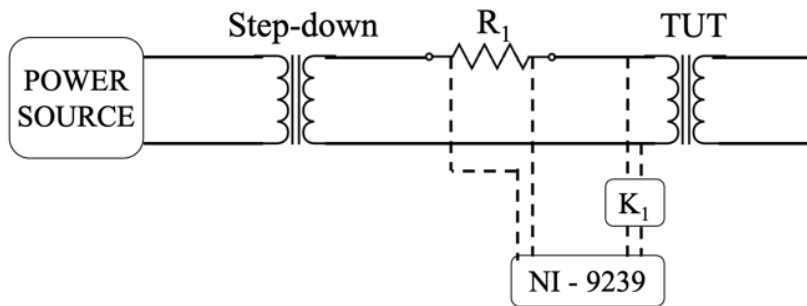


Figure 5-2. Circuit diagram of the measurement setup adopted for the short circuit tests

From such measurements the series equivalent parameters R_{eq}' and X_{eq}' , referred to the primary side, can be calculated as:

$$R_{eq}' = \frac{V_1 * \cos(\theta_1)}{I_1} \quad (5-3)$$

$$X_{eq}' = \frac{V_1 * \sin(\theta_1)}{I_1} \quad (5-4)$$

where θ_1 is computed as the difference between the angles of the current and voltage phasors. These are obtained by applying the Fourier Transform (FT) to the sequences of samples acquired by the DAQ.

5.1.2.3 Open Circuit Test

The Open Circuit (OC) test has been performed on the secondary side of the TUT by using the setup depicted in Figure 5-3. The test consisted of applying the secondary rated voltage (i.e. the ratio between rated power and rated secondary current, 2 V) and measuring its phasor (\bar{V}_2) along with the secondary current phasor \bar{I}_2 and the phase displacement θ_2 between voltage and current. The above phasors are obtained by applying the FT to the acquired samples. Then, the test has been repeated for the 75 %, 50 %, and 25 % of the rated voltage and for the two temperature of interest. Of course, the varied quantity is the voltage and not the current due to the peculiarities of the OC test. This way, it is possible to vary the operating conditions of the ferro-magnetic core. Thus, leading to different core-losses and magnetization inductance.

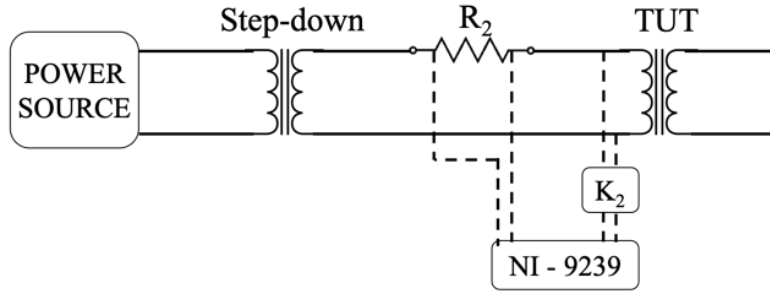


Figure 5-3. Circuit diagram of the measurement setup adopted for the open circuit tests

By using the aforementioned acquired quantities, it is possible to calculate the parallel parameters of the CT as:

$$R_w'' = \frac{V_2}{I_2 * \cos(\theta_2)} \quad (5-5)$$

$$X_m'' = \frac{V_2}{I_2 * \sin(\theta_2)} \quad (5-6)$$

In light of the performed test, the equivalent model of the CT adopted is depicted in Figure 5-4.

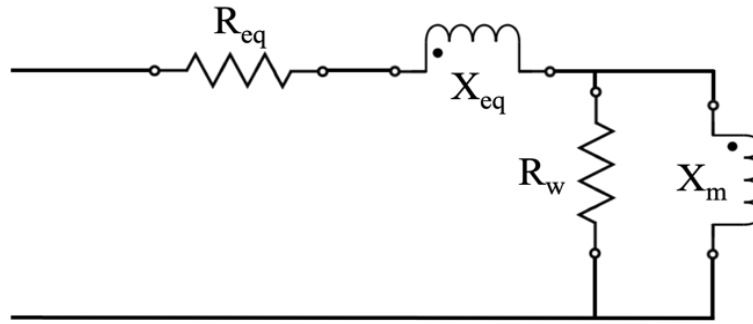


Figure 5-4. Circuit diagram of the CT equivalent circuit considered

After the description of the OC and the SC test, it is worth to highlight an important aspect. Even if the former has been performed varying the applied voltage and the latter varying the injected current, both are varying the current flowing in the CT shunt impedance. Hence, in different ways, they are changing the CT working conditions.

5.1.3 Tests Results

As previously mentioned, 1000 values for all the measured quantities have been collected.

5.1.3.1 Rated Condition Test Results

In Table 5-4, the measurement results from the test at rated conditions are presented. From the Table it can be seen that at room temperature the TUT works within its accuracy class (0.5) limits. Conversely, at 60 °C the TUT slightly overcome the 0.5 % limit value of the ratio error while the phase one is still within the 9 mrad limit. The reason for that might be the high temperature, [4] states that the working conditions should not exceed the 50 °C. However, author wanted to stress the TUT operating conditions to assess its behavior at higher temperatures.

Table 5-4. Rated conditions test results

Quantity	24 °C		60 °C	
	Mean Value	σ_m	Mean Value	σ_m
I_1 [A]	20.402	$6 \cdot 10^{-3}$	19.926	$2 \cdot 10^{-3}$
I_2 [A]	5.122	$2 \cdot 10^{-3}$	5.0081	$7 \cdot 10^{-4}$
V_1 [V]	0.87419	$5 \cdot 10^{-5}$	0.86705	$9 \cdot 10^{-5}$
V_2 [V]	2.9526	$3 \cdot 10^{-4}$	2.9078	$4 \cdot 10^{-4}$
θ_1 [rad]	0.23897	$9 \cdot 10^{-5}$	0.23639	$4 \cdot 10^{-5}$
ε [%]	-0.413	$2 \cdot 10^{-3}$	-0.532	$6 \cdot 10^{-3}$
φ [mrad]	5.54	$6 \cdot 10^{-2}$	5.50	$2 \cdot 10^{-2}$

5.1.3.2 Short Circuit Test Results

SC test results are listed in Table 5-5. Primary voltage, current and phase displacement have been acquired at 4 different current conditions. Such results represent the base to compute R_{eq}' and X_{eq}' by applying (5-3) and (5-4). The series parameters results are summarized in Table 5-6. At a glance, from the Table it can be highlighted that both operating temperature of the TUT and the primary current are not affecting its series parameters. In other words, during the CT modeling, the series parameters can be treated as constants with respect to those two quantities. The results confirm what expected in terms of dependency on the applied primary current, given that the series parameters represent leakage inductance and resistance of the TUT windings. However, the behavior of the series parameters vs. temperature was not predictable as for the previous.

Table 5-5. Short Circuit test results for different load currents

Load [%]	Quantity	24 °C		60 °C	
		Mean Value	σ_m	Mean Value	σ_m
100	I_1 [A]	20.506	$3 \cdot 10^{-3}$	20.415	$7 \cdot 10^{-3}$
	V_1 [V]	0.26561	$4 \cdot 10^{-5}$	0.27067	$7 \cdot 10^{-5}$
	θ_1 [rad]	0.8655	$2 \cdot 10^{-4}$	0.8455	$2 \cdot 10^{-4}$
75	I_1 [A]	14.846	$4 \cdot 10^{-3}$	14.814	$3 \cdot 10^{-3}$
	V_1 [V]	0.19208	$4 \cdot 10^{-5}$	0.19622	$3 \cdot 10^{-5}$
	θ_1 [rad]	0.8665	$4 \cdot 10^{-4}$	0.8463	$3 \cdot 10^{-4}$
50	I_1 [A]	10.311	$2 \cdot 10^{-3}$	10.227	$3 \cdot 10^{-3}$
	V_1 [V]	0.13377	$3 \cdot 10^{-5}$	0.13537	$3 \cdot 10^{-5}$
	θ_1 [rad]	0.863	$2 \cdot 10^{-3}$	0.8468	$4 \cdot 10^{-4}$
25	I_1 [A]	5.017	$3 \cdot 10^{-3}$	5.283	$3 \cdot 10^{-3}$
	V_1 [V]	0.06497	$4 \cdot 10^{-5}$	0.06986	$3 \cdot 10^{-5}$
	θ_1 [rad]	0.8653	$7 \cdot 10^{-4}$	0.8476	$7 \cdot 10^{-4}$

Table 5-6. CT series parameters computation results, for different loads and two temperatures

Load [%]	24 °C				60 °C			
	R_{eq}' [Ω]	σ_m [Ω]	X_{eq}' [Ω]	σ_m [Ω]	R_{eq}' [Ω]	σ_m [Ω]	X_{eq}' [Ω]	σ_m [Ω]
100	0.008397	$2 \cdot 10^{-6}$	0.009863	$3 \cdot 10^{-6}$	0.008795	$5 \cdot 10^{-6}$	0.009921	$6 \cdot 10^{-6}$
75	0.008377	$4 \cdot 10^{-6}$	0.009860	$5 \cdot 10^{-6}$	0.008778	$3 \cdot 10^{-6}$	0.009919	$4 \cdot 10^{-6}$
50	0.008436	$3 \cdot 10^{-6}$	0.009858	$4 \cdot 10^{-6}$	0.008768	$4 \cdot 10^{-6}$	0.009916	$5 \cdot 10^{-6}$
25	0.008396	$1 \cdot 10^{-5}$	0.009859	$1 \cdot 10^{-5}$	0.008751	$9 \cdot 10^{-6}$	0.009914	$1 \cdot 10^{-6}$

5.1.3.3 Open Circuit Test Results

Table 5-7 shows the OC test results performed on the secondary side of the TUT while the primary is open. As mentioned in the previous Section, the peculiarity of this test consists of varying the applied voltage from the rated to its 25 %. From the results such an approach is confirmed. As a matter of fact,

the current flowing in the CT is very low (the magnetizing current), hence it is preferable to adopt the voltage as a reference quantity for the OC test.

By starting from the measurements results of Table 5-7, the shunt parameters referred to the secondary side (R_m'' and X_m'') can be computed by using (5-5) and (5-6). Their values include also R_{eq}' and X_{eq}' ; however, considering the latter negligibility (three orders of magnitude) compared to the former, the results of (5-5) and (5-6) can be directly treated as the shunt parameters of the CT. Obtained results are collected in Table 5-8. From it, and with the help of the graph in Figure 5-5, two interesting comments arise. Firstly, both the resistance and the reactance increase when the TUT is subjected to 60 °C. Secondly, by reducing the applied voltage, hence reducing the magnetizing current circulating in the CT, a decrease of both R_m'' and X_m'' is experienced.

Table 5-7. Open Circuit test results for different load currents

Load [%]	Quantity	24 °C		60 °C	
		Mean Value	σ_m	Mean Value	σ_m
100	I_2 [A]	0.04423	$3 \cdot 10^{-5}$	0.04089	$7 \cdot 10^{-5}$
	V_2 [V]	2.05823	$9 \cdot 10^{-5}$	2.0625	$2 \cdot 10^{-4}$
	θ_2 [rad]	0.572	$1 \cdot 10^{-3}$	0.592	$2 \cdot 10^{-3}$
75	I_2 [A]	0.03341	$4 \cdot 10^{-5}$	0.03247	$7 \cdot 10^{-5}$
	V_2 [V]	1.47292	$8 \cdot 10^{-5}$	1.5591	$3 \cdot 10^{-4}$
	θ_2 [rad]	0.623	$2 \cdot 10^{-3}$	0.639	$3 \cdot 10^{-3}$
50	I_2 [A]	0.02536	$6 \cdot 10^{-5}$	0.0238	$1 \cdot 10^{-4}$
	V_2 [V]	1.05131	$9 \cdot 10^{-5}$	1.0526	$2 \cdot 10^{-4}$
	θ_2 [rad]	0.675	$3 \cdot 10^{-3}$	0.708	$5 \cdot 10^{-3}$
25	I_2 [A]	0.01575	$9 \cdot 10^{-5}$	0.0141	$1 \cdot 10^{-4}$
	V_2 [V]	0.54873	$9 \cdot 10^{-4}$	0.4657	$1 \cdot 10^{-4}$
	θ_2 [rad]	0.803	$5 \cdot 10^{-3}$	0.89947	$8 \cdot 10^{-3}$

Table 5-8. CT shunt parameters computation results, for different loads and two temperatures

Load [%]	24 °C				60 °C			
	R_w'' [Ω]	σ_m [Ω]	X_m'' [Ω]	σ_m [Ω]	R_w'' [Ω]	σ_m [Ω]	X_m'' [Ω]	σ_m [Ω]
100	55.34	0.02	85.96	0.06	60.8	0.1	90.4	0.2
75	54.28	0.07	75.56	0.09	59.8	0.1	80.5	0.2
50	53.1	0.1	66.3	0.2	58.2	0.3	68.0	0.3
25	50.2	0.4	48.4	0.4	53.1	0.4	42.2	0.3

In light of the obtained results, the “calibration” curves reported in Figure 5-5 can be used for enhancing the inductive CT modelling. In particular, once the operating temperature and the working point are known, the proper values of the shunt parameters can be selected and implemented in every model.

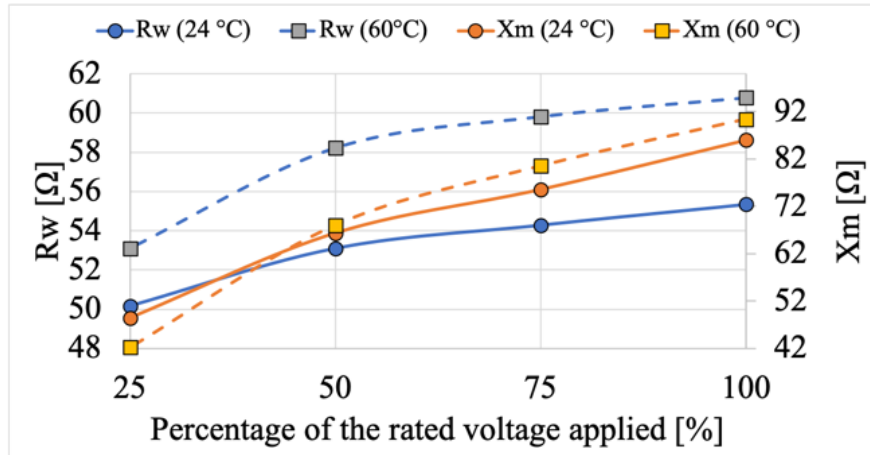


Figure 5-5. Shunt parameters representation vs. temperature vs. applied voltage

5.1.4 Conclusions

In this research work, series and parallel parameters of a 20/5 current transformer are calculated by performing short circuit and open circuit test in different loading conditions at 24 °C and 60 °C. It has been shown that series parameters can be neglected if compared to parallel parameters. In particular, the former is not affected neither from the temperature nor from the core operating conditions. Instead, the latter resulted to be affected by both quantities. More in detail, an increase of temperature turns into an increase of the shunt parameters, while a decrease of the overall current flowing in the CT core results into their decrease. In the overall, the presented study results can be used to enhance the CT modeling. this section has been published in [57].

5.2 Procedure for Inductive Current Transformers error prediction at Different Operating Conditions

In last section, open circuit test (designed for power transformers) is adapted to the CTs by accurately measuring the voltage of the CT in different conditions. Furthermore, CT shunt parameters and their variation vs. loading current and temperature are measured using open circuit test results.

In light of this, the present section addresses the influence of the loading conditions and temperature on inductive Current Transformers. To this purpose, a decomposition procedure in the CT model is performed to demonstrate the contribution of the RL filter composed of the CT shunt parameters (calculated in section 5-1) to the total ratio and phase errors.

Moreover, by starting from a simplified CT model (as in section 5-1), experimental measurements are performed to predict its ratio error and phase displacement in different operating conditions. Such a prediction is achieved from measurements done at rated conditions of the CT and applying a sort of calibration coefficients.

To the author's knowledge, the proposed approach cannot be found in literature, whereas several others compensating techniques, applied to the CTs, can. In particular, [55] deals with the compensation of the leakage currents of the CT. Harmonics and non-linearity are compensated in [58] and [59], respectively, whereas different error corrections are discussed in [60] [61] [62].

The present section is structured as: First subsection contains the measurement test setup description. The experimental tests and analysis performed on their results is tackled in next subsection. Afterwards, results are presented along with the ratio error and phase displacement prediction procedure. Finally, the main conclusion of the work is drawn.

5.2.1 Test Setup

The setup used to test the CT is depicted in Figure 5-6. It is based on the one presented last section for CT core parameters computation and it consists of:

- a function generator Agilent 33250 to generate a voltage of the desired waveform, which is applied to:
- a Fluke transconductance 52120A. It transduces the input voltage into a current in the range 0-120 A. Its main characteristics are listed in Table 5-9.
- The inductive current transformer under test. It is a 20/5 A transformer with rated power and frequency of 10 VA and 50 Hz, respectively. In addition, it features a 0.5 accuracy class designed for indoor application in Medium Voltage (MV) networks.
- A thermostatic chamber, in which the CT under test has been placed for measurements at different temperatures (24 and 65 °C).
- A $R_1 = 1\text{ m}\Omega$ and $R_2 = 10\text{ m}\Omega$ shunt resistors to measure the primary and the secondary currents, respectively.
- A pure resistive load used as rated burden ($R_B = 470\text{ m}\Omega$).
- Two resistive dividers (ratios k_1 and k_2) to measure the primary and secondary voltages.
- A NI-9238 data acquisition board (DAQ).

- A personal computer running LabView software to compute the DAQ-acquired data.

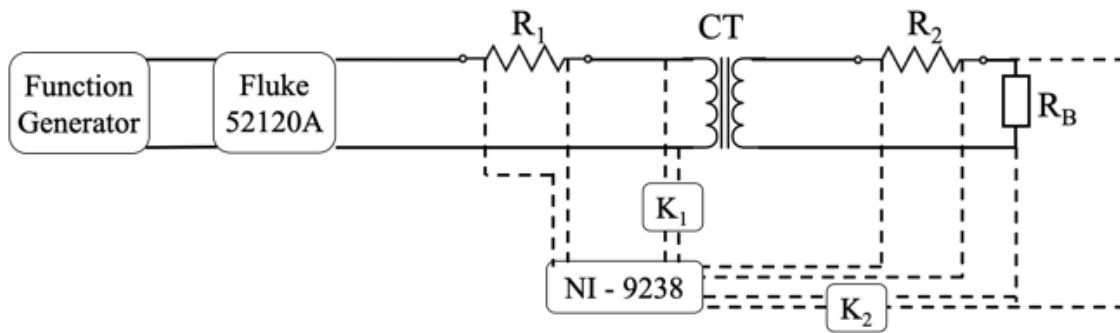


Figure 5-6. Measurement setup adopted for the rated conditions tests

Table 5-9. Fluke transconductance 52120A main characteristics

Current range [A]	Frequency [Hz]	% of output	% of range
2	10 to 65	0.015	0.070
	65 to 300	0.030	0.070
20	10 to 65	0.015	0.060
	65 to 300	0.030	0.060

Presented test setup measures primary and secondary voltages and currents waveforms which are sufficient to measure open circuit test quantities and total ratio and phase errors.

5.2.2 Experimental Tests and Analysis

With the aim of predicting the ratio error ε and the phase displacement $\Delta\varphi$ of an inductive CT, in this section rated condition test (RC) is described to obtain them in different loading conditions and different temperatures.

Moreover, experimental procedures are described to decompose the overall ε and $\Delta\varphi$ and to evaluate the shunt parameters contribution to them. Firstly, Open Circuit (OC) test is described to obtain the shunt parameters of the CT in different loading conditions and different temperatures. Secondly, its equivalent parameters (R_w and X_m) are used to estimate their contribution as RL filter, shown in Figure 5-7 from the simplified CT model, to the overall ratio error and phase displacement measured during RC test. Thirdly, the mathematical expression to assess ε and $\Delta\varphi$ yields the non-ideal CT transformation ratio, which is presented as an ideal transformer with the calculated transformation ratio (N_I). The complete model of the CT with ideal transformer (N_I) and the RL filter composed of R_w and X_m is shown in Figure 5-8.

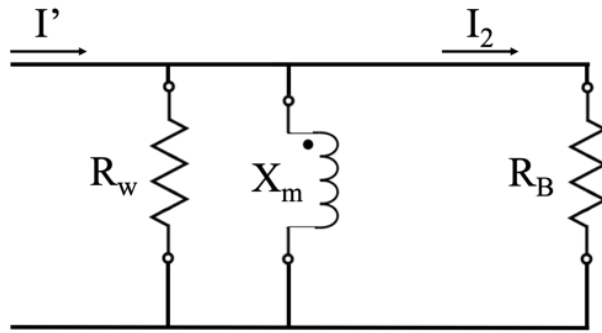


Figure 5-7. Part of the CT equivalent circuit detailing the shunt parameters and the burden

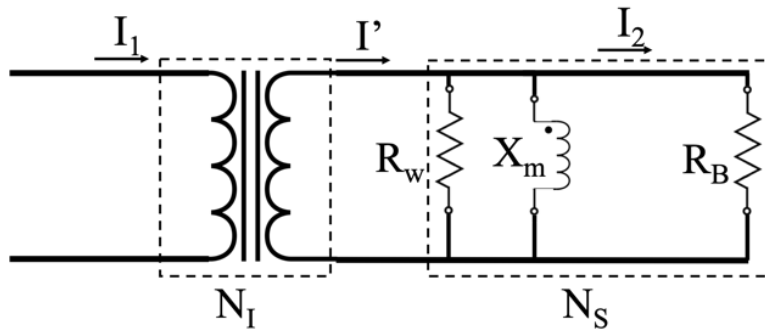


Figure 5-8. Complete model of the CT adopted in the work

5.2.2.1 Rated Condition and Open Circuit test

By using the setup depicted in Figure 5-6, during the rated condition test four different currents: 5, 10, 15, and 20 A have been injected in the CT at 24 °C which correspond to the 25, 50, 75, and 100 % of the CT primary current, respectively. Then, both primary and secondary voltage and current phasors have been acquired to calculate ε and $\Delta\varphi$ using (5-1) and (5-2) which are introduced in previous section.

Afterwards, the same test has been performed also at 40 °C, 50 °C, and 65 °C. The latter temperature overcomes the limit for the CT testing according to the Standards [4]; however, in this way the temperature working range is extended and include more plausible operating conditions.

As for the OC test, it has been done in previous section (section 5-1-2-3). The OC test has been performed (i) keeping the primary (high current) side open, (ii) applying the voltages measured in RC tests to the secondary, and (iii) measuring the secondary voltage and current phasors. Such test, under the assumption of neglecting the CT series parameter (as justified in section 5-1), allows to determine the shunt parameters of the CT as (5-5), and (5-6).

5.2.2.2 Shunt Parameters role in the CT accuracy

The shunt parameters R_w and X_m are here used to assess their contribution to the overall ratio (hence ratio error) and phase displacement of the CT. By starting from the equivalent circuit shown in Figure 5-7, and after frequency magnitude response calculation, the ratio N_S and phase-shift φ_S introduced by the shunt parameters are:

$$N_S = \frac{I_2}{I'} = \frac{R_w * X_m}{\sqrt{R_w^2 * R_b^2 + X_m^2 * (R_b + R_w)^2}} \quad (5-7)$$

$$\varphi_S = \tan^{-1} \left[\frac{R_b * R_w}{X_m * (R_b + R_w)} \right] \quad (5-8)$$

where I' is the module of the current flowing upstream the shunt parameters.

5.2.2.3 Ratio and Phase Displacement Components

From the knowledge of N_S and φ_S , and by referring to the equivalent circuit shown in Figure 5-8, all the contributions to ε and $\Delta\varphi$ can be highlighted. In detail, ε and $\Delta\varphi$ can be considered as due to two factors: the shunt parameters (as described above) and a quasi-ideal transformer which has an actual ratio and phase different from the rated one due to its manufacturing process. Therefore, the overall transformer ratio N can be expressed as:

$$N = \frac{I_1}{I_2} = N_I * N_S = \frac{I_1}{I'} * \frac{I'}{I_2} \quad (5-9)$$

where $N_I = I_1/I'$ is the quasi-ideal transformer ratio. Such value has been computed, for all the cases of the RC test, by starting from the quantities N_S and N (also refer to Figure 5-8).

As for the phase, the overall $\Delta\varphi$ is the sum of two separate phase-shiftings:

$$\Delta\varphi = \varphi_I + \varphi_S \quad (5-10)$$

where φ_I is the not-null phase-shift component introduced by the non-idealities of the CT. Considering (5-9) and (5-10) it is then possible to assess the effect of each contribution, by means of the experimental results.

5.2.3 Experimental tests and accuracy prediction results

This section describes the obtained results and use them to obtain a sort of calibration curves to predict the ε and $\Delta\varphi$ of a CT under determined operating conditions, by proposing some coefficients.

5.2.3.1 OC test results

Test results are reported in Table 5-10. The table contains the parameters at 24 °C and 65 °C obtained in previous section, and the new parameters obtained at 40 °C and 50 °C. The parameters R_w and X_m , are expressed as their mean value of 1000 measurements along with their standard deviation of the mean. About 10 % of the variation is seen in both shunt resistance and inductive reactance.

Table 5-10. CT shunt parameters for different loads and temperatures

Load [%]	24 °C				40 °C				50 °C				65 °C			
	R_w [Ω]	σ_m [Ω]	X_m [Ω]	σ_m [Ω]	R_w [Ω]	σ_m [Ω]	X_m [Ω]	σ_m [Ω]	R_w [Ω]	σ_m [Ω]	X_m [Ω]	σ_m [Ω]	R_w [Ω]	σ_m [Ω]	X_m [Ω]	σ_m [Ω]
100	55.34	0.02	85.96	0.06	57.06	0.02	89.12	0.04	58.1	0.1	90.1	0.3	60.8	0.1	90.4	0.2
75	54.28	0.07	75.56	0.09	56.11	0.02	80.41	0.03	57.2	0.2	80.4	0.2	59.8	0.1	80.5	0.2
50	53.1	0.1	66.3	0.2	54.55	0.03	70.11	0.07	55.8	0.1	69.6	0.2	58.2	0.3	68.0	0.3
25	50.2	0.4	48.4	0.4	51.51	0.03	53.09	0.06	52.5	0.3	49.3	0.3	53.1	0.4	42.2	0.3

5.2.3.2 Ratio and Phase displacement decomposition results

The results of the RC tests and of the application of the inverse equations of (5-9) and (5-10) are collected from Table 5-11 to Table 5-16. In detail, Table 5-11 to Table 5-14 contain, for each loading condition and for each temperature, the ratios N and N_S along with the phase displacement $\Delta\varphi$ and φ_S . Table 5-15 and Table 5-16 instead lists, for each temperature and loading condition, the computed ratios N_I and phase displacement φ_I (starting from (5-9) and (5-10)).

Table 5-11. Ratio error and phase displacement results and the decomposition at 24 °C

Load [%]	24 °C				
	Shunt Parameters		RC		
	N_S [-]	φ_S [rad]	N [-]	ε [%]	$\Delta\varphi$ [rad]
100%	0.991282	0.00562	3.9932	-0.17	0.00441
75%	0.991355	0.00610	3.9945	-0.14	0.00473
50%	0.991267	0.00714	3.9957	-0.11	0.00516
25%	0.990881	0.01003	3.9978	-0.05	0.00602

Table 5-12. Ratio error and phase displacement results and the decomposition at 40 °C

Load [%]	40 °C				
	Shunt Parameters		RC		
	N_S [-]	φ_S [rad]	N [-]	ε [%]	$\Delta\varphi$ [rad]
100	0.991817	0.005231	3.9936	-0.16	0.00451
75	0.991677	0.005796	3.9944	-0.14	0.00491
50	0.991436	0.006646	3.9956	-0.11	0.00535
25	0.990919	0.008772	3.9980	-0.05	0.00627

Table 5-13. Ratio error and phase displacement results and the decomposition at 50 °C

Load [%]	50 °C				
	Shunt Parameters		RC		
	N_S [-]	φ_S [rad]	N [-]	ε [%]	$\Delta\varphi$ [rad]
100	0.991962	0.005175	3.9944	-0.14	0.00473
75	0.991834	0.005798	3.9948	-0.13	0.00508
50	0.991625	0.006696	3.9960	-0.10	0.00555
25	0.991083	0.009448	3.9984	-0.04	0.00645

Table 5-14. Ratio error and phase displacement results and decomposition at 65 °C

Load [%]	65 °C				
	Shunt Parameters		RC		
	N_S [-]	φ_S [rad]	N [-]	ε [%]	$\Delta\varphi$ [rad]
100	0.991993	0.00538	3.9947	-0.13	0.00480
75	0.991967	0.00596	3.9952	-0.12	0.00521
50	0.991869	0.00694	3.9963	-0.09	0.00574
25	0.991183	0.01105	3.9987	-0.03	0.00669

Table 5-15. Quasi-ideal transformer ratio and phase displacement for Temperatures 24 °C and 40 °C

Load [%]	24 °C		40 °C	
	N_I [-]	φ_I [rad]	N_I [-]	φ_I [rad]
100	4.0283	-0.00121	4.0265	-0.00072
75	4.0294	-0.00139	4.0279	-0.00088
50	4.0306	-0.00198	4.0301	-0.00129
25	4.0346	-0.00403	4.0346	-0.00250

Table 5-16. Quasi-ideal transformer ratio and phase displacement for Temperatures 50 °C and 65 °C

Load [%]	50 °C		65 °C	
	N_I [-]	φ_I [rad]	N_I [-]	φ_I [rad]
100	4.0268	-0.00044	4.0270	-0.00058
75	4.0273	-0.00071	4.0276	-0.00075
50	4.0297	-0.00114	4.0291	-0.00120
25	4.0344	-0.00299	4.0343	-0.00433

As a first comment, ε , which standard deviation of the mean is in the order of 10^{-4} seems to be slightly affected from loading condition, whereas the temperature does not affect it. $\Delta\varphi$ instead, which standard deviation of the mean is in the order of 10^{-5} , remains almost constant vs. both influence quantities. A

further comment can be done on shunt parameters contributions: both N_S and φ_S , despite the R_w and X_m changes, remain almost constant for temperature or loading current variations. Hence, the contribution of the shunt parameters in the overall accuracy performance of the CT is constant. Furthermore, N_S and φ_S are known with a low level of uncertainty: 10^{-6} and 10^{-5} , respectively. It is pointed out that the shunt parameters introduce about 1 % error in the magnitude, which is mechanically compensated during the manufacturing process by acting on the secondary number of turns.

5.2.3.3 Ratio and Phase Error Prediction

To predict ratio and phase error, ε and $\Delta\varphi$ at 24 °C and 100 % loading current from Table V have been chosen as a reference point and referred to as ε_{ref} and $\Delta\varphi_{ref}$ ($\varepsilon_{ref} = -0.17\%$ and $\Delta\varphi_{ref} = 0.0044$). Afterwards, ratio errors and phase displacements from RC test reported in Table V, VI, VI, and VIII have been used to compute four dynamic coefficients, dependent on the operating temperature and load (e_T and e_C for predicting the ratio error w.r.t. temperature and current respectively, and f_T and f_C for predicting the phase error w.r.t. temperature and current respectively). Four coefficients are calculated as following:

- e_T : ratio error at 40 °C, 50 °C, and 65 °C divided by the ε_{ref} . For each temperature, the average ratio error from 25% to 100% of loading is considered.
- e_C : ratio error at 25%, 50%, and 75% of loading current divided by the ε_{ref} . For each loading current the average ratio error from 24 °C to 65 °C is considered.
- f_T : phase displacement at 40 °C, 50 °C, and 65 °C divided by the $\Delta\varphi_{ref}$. For each temperature, the average phase error from 25% to 100% of loading is considered.
- f_C : phase displacement at 25%, 50%, and 75% of loading current divided by the $\varepsilon_{ref} \Delta\varphi_{ref}$. For each loading current the average phase error from 24 °C to 65 °C o is considered.

Finally, a 3rd order curve fitting procedure has been applied to the four obtained coefficients curves to obtain four functions listed in Table 5-17. In Figure 5-9 the two functions for the temperature e_T and for the current e_C related to ε are graphed. As for the phase, the obtained functions f_T and f_C are depicted in Figure 5-10.

Table 5-17. Dynamic coefficients and their functions

Symbol	Function
e_T	$0.000016886*T^3 - 0.002368509*T^2 + 0.098128875*T - 0.224269268$
e_C	$0.000211765*I^3 - 0.009411765*I^2 + 0.171176476*I - 0.352941200$
f_T	$-0.000003065*T^3 + 0.000405028*T^2 - 0.013966379*T + 1.144266878$
f_C	$-0.000063307*I^3 + 0.0036204*I^2 - 0.08130733*I + 1.684440$

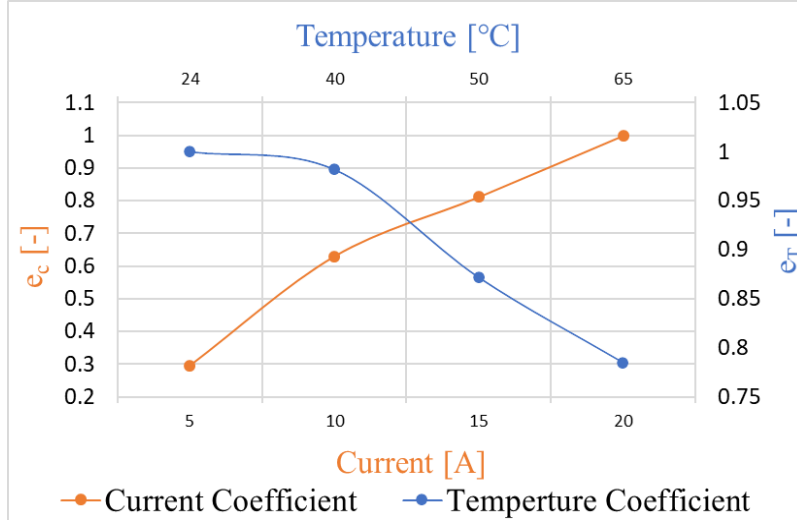


Figure 5-9. Functions e_T and e_C for the ratio error prediction

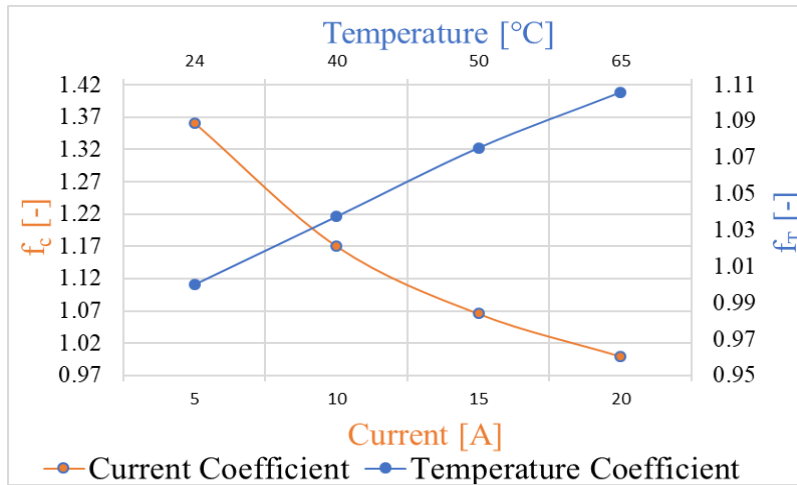


Figure 5-10. Functions f_T and f_C for the phase displacement prediction

At this point, to predict ε and $\Delta\varphi$ by starting from determined loading and temperature conditions, the following equations apply:

$$\varepsilon_x = \varepsilon_{ref} * e_T * e_C \quad (5-11)$$

$$\Delta\varphi_x = \Delta\varphi_{ref} * f_T * f_C \quad (5-12)$$

where ε_x and $\Delta\varphi_x$ are the generic ratio error and phase displacement at predefined temperature and loading conditions. As all coefficients are achieved by division to the reference values, by approximating the coefficients from the obtained curves and multiplication by the reference points, the ratio error and phase displacement are predicted.

To prove the effectiveness of (5-11) and (5-12) a further test has been performed. The CT has been run at 45 °C and 55 °C with a loading current of 8 A and 12 A respectively, which correspond to the 40 % and 60 % of the rate loading condition. Considering the reference ratio and phase error at 24 °C and 20 A ($\varepsilon_{ref} = -0.17\%$ and $\Delta\varphi_{ref} = 0.0044$), the measurement of ε and $\Delta\varphi$ provides the results of Table XII. The comparison of the two set of results confirms the proposed approach and expressions. Of course, both predicted random error and possible systematic error from RL filter response can be compensated real time.

As a final comment, by starting from a set of simple initial measurements, the CTs behavior can be predicted in terms of ratio error and phase displacement. The linear results vs. temperature and vs. loading current suggest that even a lower number of tests might be performed, fastening the calibration process of a single CT.

5.2.4 Conclusions

This section has presented a further step towards the complete knowledge of the CT behavior when influenced by different quantities. In particular, the main accuracy parameters have been measured varying the ambient temperature and the loading current flowing through the CT. Firstly, a simplified CT model has been used to highlight the main contributions to the ratio error and phase displacement which can be used to calculate the type B error to be compensated during operation of CTs. Then, the performed tests have been used to obtain a sort of “calibration” curves to be used to predict the CTs accuracy. Afterwards the proposed approach has been verified with an experimental test, which confirmed what aimed by the author. In conclusion, the proposed solution can be adopted when all other influence quantities effect on CT are known or stable. Of course, in complex scenarios the effects cannot be predicted, but in a stable environment (as a laboratory one) the presented approach can be used to avoid continuous calibration of the own equipment.

6 Low-Power Voltage Transformer Smart Frequency Modeling and Output Prediction up to 2.5 kHz, Using Sinc-Response Approach

In smart grid paradigms, knowledge of power network state variables is a key requirement for the power-system stability. To measure the node voltages and the branch currents as state variables, instrument transformers (ITs) are deployed. Because of the widespread use of distributed generation (DG) especially at the medium voltage (MV) level, studies on MV ITs are hot topics nowadays. Inductive-voltage transformers (VTs) and inductive current transformers (CTs) form the legacy or conventional ITs family, while the low-power voltage transformers (LPVTs) and low-power current transformers (LPCTs) form the new generation of low-power instrument transformers (LPITs). LPVTs feature a smaller size and lighter weight as compared to conventional ITs, which make them distinguished in smart grids considering the DGs. Moreover, LPITs have a wider frequency band which makes them suitable for power-quality measurements, as well as other applications that involves a substantial harmonic content and frequencies different from the typical 50–60 Hz range.

ITs are mainly used for protection and measurement purposes. Protection ITs need to detect rapidly changing voltages or currents, while measurement ITs need to measure voltage and current with as much accuracy as possible. Measurement errors may lead to wrong estimates of state variables during the state-estimation (SE) process and load-flow measurements in MV network; therefore, resulting in network instability whether or not wrong corrective actions are implemented according to the wrong measurements obtained. The measured power may also be used for billing purposes, which means that it is mandatory for the ITs to be compliant with the limits fixed by their accuracy class (AC). For the above reasons, studies on the modeling, characterization, uncertainty analysis, and accuracy assessment under different influence quantities are some of the most studied topics in this area.

For example, [63] [64] introduce a test bed for LPITs for industrial applications and methods for their testing. For accuracy assessment, ratio error and phase displacement are the two main parameters to be measured. In terms of accuracy assessment, [65], [66], and [67] represent the efforts on the installation, traceability, and challenges of integration in LPVTs. The uncertainty analysis of the ITs and their calibration test bed as a key factor for measurement, is performed in [68], [69], [70], [71], and [72], while the nonlinearity compensation is assessed in [73] for voltage and current ITs.

The modeling of ITs at first glance looks already familiar due to the fundamental operation of ITs, but it requires new techniques to be developed. Such techniques are required because the measurement

ITs model must be very accurate to be reliable for electric utilities and to provide useful information for the network management. In other words, the research works on modeling are closely linked to those on the ITs accuracy.

The impulse-response (IR) test is a well-known method for dynamic systems modeling. In this work, the author starts from the IR test concept for modeling a passive LPVT rated for a MV network. There is a large limit on IR test performance on LPVTs. LPVTs based on capacitive dividers are only slightly dependent on frequency. Normally, this dependency is neglected in industrial applications, while it is critical when LPVTs need to be accurately characterized for different frequencies even though the accuracy may slightly change. In the literature, IR tests and sweep frequency (known as frequency-response) tests are performed for different applications. [74], and [75] are some research works on IR test performed on mechanical and electrical systems. For frequency-response tests, [76], [77], and [78] are the research works done on VTs. [79] represents another frequency characterization of VTs, while [80] analyzes the frequency characterization of VT under network interruptions. For LPCTs, [81] introduces a new Rogowski coil design to measure a wide pulse current.

To overcome the limitations on IR accurate measurement, this work applies a new technique using a normalized sinc signal for the characterization of LPVTs. This approach is called sinc-response (SR) test in correlation with IR test terminology. In contrast to impulse signal, a sinc signal has the advantage of being easily measurable by conventional acquisition systems. However, in the SR test, the maximum frequency is limited to a certain range to be set during the design of the sinc signal (as detailed in the core of the work). The limited frequency is not an issue for the purpose of the work, which is to characterize the passive LPVT up to power quality frequency range (2.5 kHz) (see [82]).

The SR approach was introduced in [35] and applied for the prediction of the Rogowski coil output, but without focusing on ratio error and phase-displacement aspects.

In this work, an electric equivalent circuit of the LPVT under test is introduced in, while the concept of SR and IR testing is discussed afterwards. The section after, deals with the theoretical and mathematical design of the sinc signal. The adopted experimental setup is introduced in next subsection. In the next subsection, the required experimental test procedures, model extraction using SR test, and simulations for output prediction are discussed. The simulation and experimental test results are reported and discussed in results subsection, while in the last section, it is summarized, the main achievements of the work and presents the main conclusions.

6.1 LPVT Model

In this work, the considered LPVT is a capacitive one. The reason for this choice is that such kind of LPVT is increasing adopted when an LPVT is considered for installation in the distribution network. However, any kind of LPVT may be tested with the proposed approach.

LPVTs based on capacitive dividers are mainly designed in active and passive configurations. The difference between the two categories concerns the design limitation and the customer preference. Figure 6-1 shows an electric equivalent circuit of a passive LPVTs based on a pure capacitive divider. Normally, the secondary capacitor is an embedded one, while the primary capacitor is a built-in capacitor obtained from the chassis of the device. For this reason, the built-in primary capacitance may vary from device to device, hence leading to different transformation ratios for different products. To normalize the transformation ratio and phase displacement of each product to the nominal values—after the characterization process—correction factors are provided to the customer by the manufacturer. It should be noted that in any case the accuracy class is not compromised.

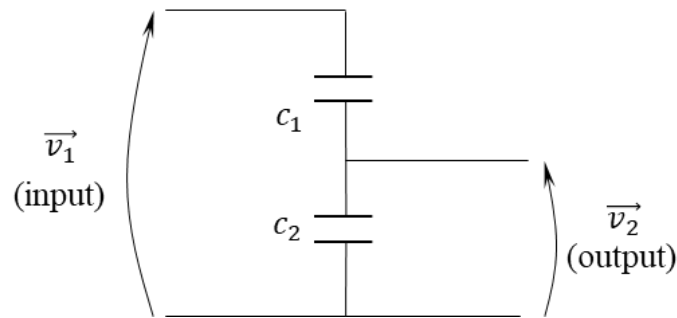


Figure 6-1. Low-power voltage transformers (LPVT) electric equivalent circuit

On the other hand, in active LPVTs an active electronic amplifier is added to the passive LPVT to bring the transformation ratio and phase displacement to the nominal ones so that all final products keep the nominal values declared on the nameplate without introducing extra correction factors.

In case of considering an ideal LPVT (composed of ideal capacitors) showed in Figure 6-1, the transformation ratio expressed in Equation (6-1) is simply a gain with zero phase displacement and it is not frequency-dependent.

$$\vec{v}_2 = \frac{c_1}{c_1+c_2} \vec{v}_1 \quad (6-1)$$

Equation (6-1) represents the input–output relation of the ideal LPVT where v_1 and v_2 are the primary and secondary voltages, respectively, while c_1 and c_2 are the primary and secondary capacitors, respectively.

The ideal LPVT cannot be obtained in practical situations and the non-idealities are mainly due to two reasons: (a) resistive or conduction leakage in the dielectric material of capacitors and (b) phase displacement between real and imaginary part of dielectric permeability in capacitors. Both mentioned properties are slightly variable with frequency, which lets the overall ratio error and phase displacement to be slightly frequency-dependent. The word “slightly” in the term “slightly frequency dependency” is used to emphasis the fact that, in contrast to Equation (6-1), the transfer function of an LPVT is not simply a gain. Therefore, the LPVTs can be considered dynamic systems which accurate modeling by using SR test builds the core of the present research.

6.2 IR Test Method vs. SR Test Method

6.2.1 IR Test Method

The characterization of a dynamic or static system using IR test, corresponds to the system input–output relation in different frequencies. The range of the frequency and the frequency component selection depends on the closeness of the impulse signal to the ideal one. According to Equation (6-2), an ideal impulse signal implementation is a crucial task to perform. The challenge of implementing such signal mainly concerns the width of the signal around $t = 0$. The importance of the implementation of a quasi-ideal impulse signal is even greater if the system under test is not highly frequency-dependent.

$$\delta(t) = 0 \text{ for } t \neq 0, \int_{-\infty}^{+\infty} \delta(t) dt = 1 \quad (6-2)$$

In Equation (6-2), $\delta(t)$ indicates the Dirac delta distribution function. In case of a slightly frequency-dependent system, the impulse-response is highly similar to the input impulse signal. The slightly difference between input impulse signal and impulse response represents the system model included in the transfer function. In this case, highly accurate signal acquisition techniques are required for both input and output signals to establish the input–output relation. In particular, high sampling rate for the analog-to-digital converter (ADC) is required for the transfer function extraction. In practice, even high-resolution data-acquisition boards (DAQ) and oscilloscopes are not capable of input impulse signal and impulse-response signal acquisition for some slightly frequency-dependent systems such as LPVTs.

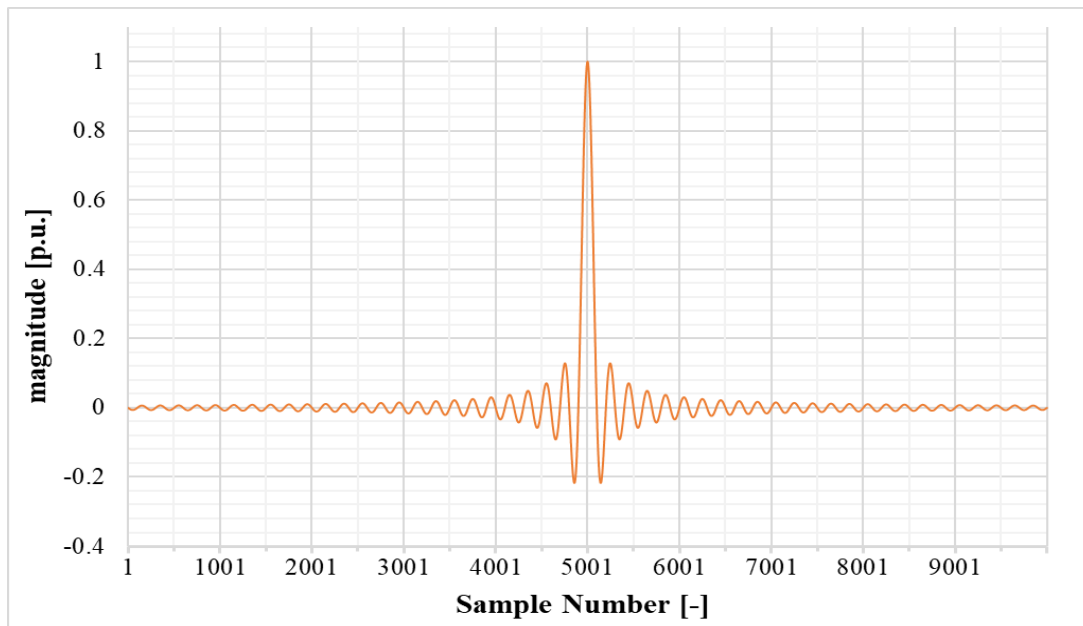
Consequently, the input–output relation is not well established and the procedure for model extraction fails.

6.2.2 SR Test Method

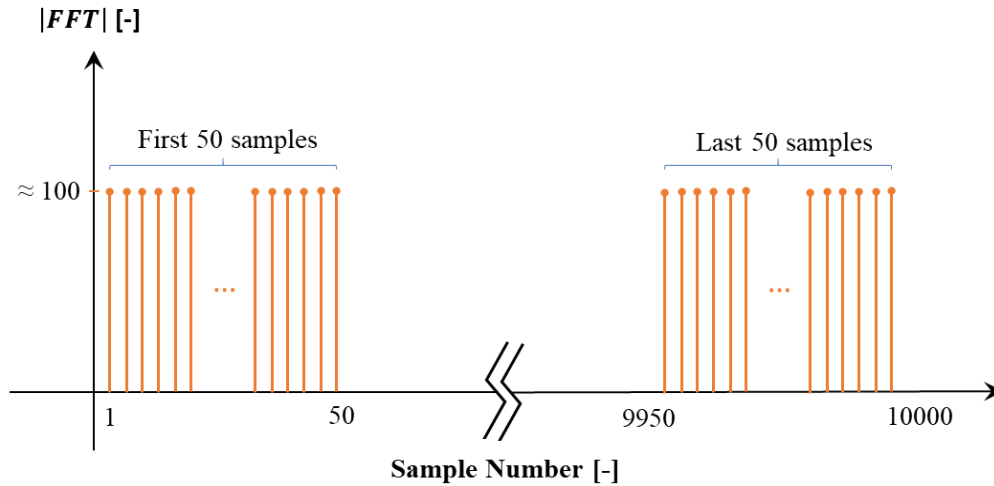
The sinc-response test represents the characterization of the system using the normalized sinc signal instead of an impulse signal. The normalized sinc function defined as:

$$\text{Sinc}(x) = \frac{\sin(\pi x)}{\pi x} \quad (6-3)$$

has a frequency domain characteristic similar to that of an impulse signal, but in a limited range and with a frequency step defined during the design of the sinc signal. The ideal impulse signal in frequency domain represents a constant function with unity value ranging from $-\infty$ to $+\infty$ while, a sampled sinc signal represents a rectangular window. Figure 6-2 shows the designed sinc signal for this work and the corresponding Discrete Fourier Transform (DFT) using 49 side lobes and $N = 10,000$ samples.



(a)



(b)

Figure 6-2. Designed normalized sinc signal. (a) Time domain; (b) discrete Fourier transform (DFT) magnitude

According to the sinc signal repetition frequency and the considered number of lobes, the width of each lobe is wide enough to be sampled using conventional ADCs and to be measured using conventional DAQs and oscilloscopes. This feature is the key to overcome the challenge of accurate measurement of input and output signals in IR test by using SR test instead of it. This is the approach adopted in this work.

On the other hand, the disadvantage of SR test is the limitation on the frequency range that the LPVT is characterized for. However, the 2.5 kHz power quality frequency range (adopted in this work) allows a proper testing of the LPVTs, guaranteeing the desired accuracy and resolution for the characterization process.

Of course, even if omitted in Figure 6-2, the signal has a direct component which is completely neglectable, compared to the main signal and out of scope of this work.

Summarizing, the three main characteristics of a sinc signal are: (i) number of lobes; (ii) number of samples which represents the magnitude of each frequency component in frequency domain and (iii) repetition frequency of the sinc signal itself. The relation between the mentioned three features and the procedure for the discrete sinc signal design is expressed in immediate next section.

6.3 Sinc Signal Design

The goal is to specify the frequency corresponding to any sample, within the rectangular window in the DFT graph of Figure 6-2, to design the sinc signal to operate in the power quality range (2.5 kHz)

and to calculate the Fourier series coefficient for each frequency component. In this work, the normalized sinc function is designed and sampled to be generated, amplified, and applied to the LPVT under test. According to Figure 6-2, the design variables to be considered are: the DFT amplitude, frequency range and frequency resolution (frequency step). In the sinc function design procedure, a tradeoff between the three variables should be obtained.

6.3.1 Sinc Function Fourier-Transform Analysis

Both time domain and frequency domain sinc signals are sampled data; this is why DFT is used. It is recalled that the Discrete Time Fourier Transform (DTFT) applied to a sampled signal, outputs the continuous frequency domain signal with period of 2π as:

$$X(e^{j\omega}) = \sum_{n=-\infty}^{+\infty} x(n)e^{-j\omega n} \quad (6-4)$$

In order to extract the DFT, the periodic function DTFT is sampled in frequency domain with respect to the variable ω . One important consideration is that both time and frequency domain sampling frequency is equal to the same value N . Applying DTFT sampling, Equation (6-4) turns into:

$$X(k) = \sum_{n=-\infty}^{+\infty} x(n)e^{-j\left(\frac{2\pi}{N}k\right)n} \quad (6-5)$$

As Figure 6-2 shows, the width of the window is represented in terms of number of Samples N . It is well known that the width of the window represents the range of the frequency components contained in the designed sinc signal. To specify the frequency corresponding to the number of samples in the width of the window, it is useful to define the following variables:

- f_o [Hz]: the sinc signal repetition frequency in time domain.
- T_o [s]: the period of the sinc signal ($1/f_o$).
- f_s [Sa/s]: sampling frequency of the DAQ.
- T_s [s]: the sampling time ($1/f_s$).
- N : the number of samples in only one period of the sinc signal.

According to the above definitions and to Figure 6-3. Sampling principle of an arbitrary signal, one can obtain Equation (6-6). Through simple mathematics it can be shown that T_s is normalized in Equation (6-6) and it is the motivation to define a new variable f_n , the “normalized frequency”.

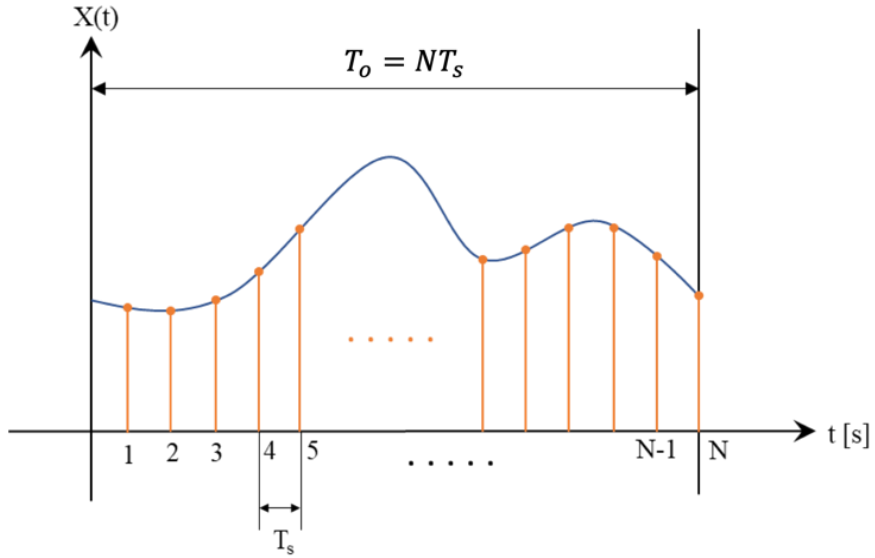


Figure 6-3. Sampling principle of an arbitrary signal

$$\frac{f_o}{f_s} = \frac{1}{N} = f_n \quad (6-6)$$

Then, in light of Equations (6-5) and (6-6), it is possible to write:

$$\omega_k = 2\pi \frac{k}{N} = 2\pi k f_n \quad (6-7)$$

Since f_o and f_s are known design parameters, according to Equation (6-6), f_n is known as well. Moreover, k is ranging from 1 to N . Now Equation (6-6) can be rewritten in the general form as Equation (6-8), which $f_{o,k}$ is defined as the frequency corresponding to the sample number k .

$$f_{o,k} = \frac{k}{N} f_s = k f_n f_s \quad (6-8)$$

From Equations (6-6) and (6-8), the relation between the sample number (k), time domain repetition frequency (f_o), and corresponding frequency to k th sample is summarized in:

$$f_{o,k} = k f_o \quad (6-9)$$

which shows that the frequency corresponding to the k -th sample ($f_{o,k}$) is dependent of the sinc signal repetition frequency in time domain (f_o), that is the design parameter to be chosen. Moreover, Equation (6-9) indicates that the frequency resolution is exactly f_o .

6.3.2 Sinc Function Characteristic

The normalized sinc function expressed in Equation (6-3) crosses the horizontal axis at each integer value of the amplitude variable. Considering the sinc function domain $[-a, +a]$ such that $a \in \mathbb{Z}^+$, there will be $2a - 1$ extrema in that domain. One extremum appears at $x = 0$ and $(2a - 2)$ extrema appear

between each two consecutive integer points in domains $[-a, -1]$ and $[+1, +a]$. The extrema points are maxima and minima alternatively. By convention, each extremum represents a lobe in the sinc function. Therefore, there is one “*main lobe*” and $(a - 1)$ “*side lobe*” at each side of the main lobe.

For a sinc signal with “ a ” numbers of side lobes and N samples, DFT amplitude outputs two rectangular windows with the width of “ a ” number of samples each and the approximated amplitude of $N/2a$. An approximation of the DFT amplitude in terms of samples (n) for the considered sinc function can be generalized as:

$$|FFT| = \begin{cases} N/2a & 1 \leq n < a \\ 0 & a < n < N - a \\ N/2a & N - a < n \leq N \end{cases} \quad (6-10)$$

Considering the continuous normalized sinc function defined in $[-a, +a]$, negative numbers are considered, but in sampled normalized sinc function, the samples range from 0 to N . For this reason, the DFT outputs two rectangular windows with the width of “ a ” for each window. In this case we only consider the first rectangle window from 0 to “ a ”, because the other rectangle corresponds to the negative frequencies in Fourier Transform analysis of the continuous sinc function and not the discrete one.

In this stage, according to Equation (6-9), we can specify the full frequency range of the designed sinc signal by considering $k = a$ and selecting the proper value for f_o . Parameters f_o and “ a ” are considered as design parameters and in this work a normalized sinc function with $a = 50$ and $f_o = 50$ Hz with $N = 10,000$ samples for each period is designed. Inserting the design parameters in Equation (6-9) leads to $f_{o,50} = 2.5$ kHz which is the power quality range. As for the selected $a = 50$, it gives a sinc signal with 49 side lobes as shown in Figure 6-2.

6.3.3 Sinc Function Fourier Series Coefficients

In practice, the Fourier Series (FS) coefficients for each harmonic are critical to be considered. FS coefficients represent the amplitude of each sine wave with different frequencies applied to the LPVT during the SR test. As the LPVT is designed to be supplied with sinusoidal waveforms, it is important to verify the LPVT operation under sinc function. To do this, the study of FS coefficients is necessary. In this work, the signal processing is based on DFT and to calculate the FS coefficients from DFT amplitude we need to divide it to the number of samples (N). Considering Equation (6-10), the FS coefficients are approximated as $1/2a$ for all the harmonics. The $1/2a$ values are the amplitude of the sinusoidal waves which are applied to the LPVT during the SR test if the amplitude of sinc signal is one. To compute the

ratio error and phase displacement in the test procedure in Section 6, the exact values are calculated and considered. Considering the design parameters $a = 50$ and $f_o = 50 \text{ Hz}$, the FS coefficients are approximated as $1/2a = 0.01 \text{ V}$, if the peak amplitude of sinc Signal is 1 V. In practice the sinc signal is amplified 16,000 times and by applying 16 kV sinc signal to the LPVT, the FS coefficient are about 160 V ($0.01 \times 16,000$). In other words, while LPVT is supplied by the series of sinusoidal waveforms with the amplitude of 160 V, the LPVT is experiencing 16-kV peak value by injecting the 16 kV sinc signal, and this is one of the big advantages of SR test. Although the LPVTs are designed to be supplied with sinusoidal waveforms and sinc signal has a different voltage profile (in terms of RMS and mean values), in the results section it is shown that the LPVT behavior is the same as long as it experiences the same voltage stress related to the peak voltage.

6.4 Experimental Test Setup

The designed sinc signal from last section is sampled and uploaded in a signal generator as an arbitrary waveform to be generated. The obtained signal is amplified by a power amplifier up to the rated peak voltage (16 kV). The amplified signal is applied to the LPVT under test as the primary voltage. The LPVT secondary voltage is acquired using a DAQ along with the primary voltage which is scaled using a resistive–capacitive reference voltage divider. Figure 6-4 represents the simplified scheme of the implemented test setup.

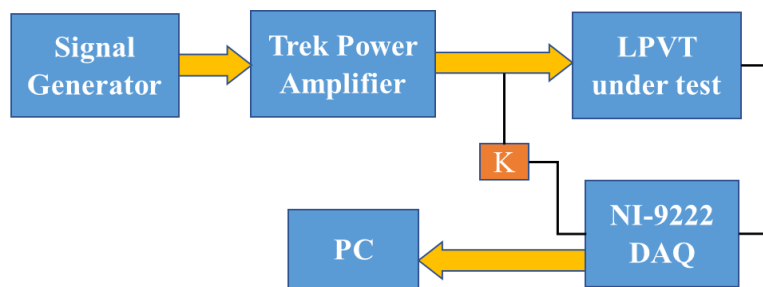


Figure 6-4. Experimental test setup scheme

Its main components are:

- Agilent 33250A 80 MHz function/arbitrary signal generator used to generate the designed sinc signal.
- Trek high speed/high voltage power amplifier model 20/20C-HS to amplify the generated signal to 16-kV peak rated voltage. Its main characteristics are listed in Table 6-1.

- Passive capacitive LPVT under test with $\frac{20}{\sqrt{3}}kV/\frac{2.73}{\sqrt{3}}V$ rated voltage and 0.5 accuracy class.
- Resistive–capacitive reference voltage divider with $\frac{20}{\sqrt{3}}kV/\frac{3.34}{\sqrt{3}}V$ rated voltage, ratio K and 0.1 accuracy class to measure the primary signal. It is used as a reference.
- NI 9222 data-acquisition board with ± 10 -V range and 500 kSa/s sampling frequency. Its accuracy features are: $\pm 0.02\%$ gain error and $\pm 0.01\%$ offset error.

Table 6-1. Trek power amplifier features

Output Voltage Range	0 to 20–kV DC or AC Peak	DC Voltage Gain	20,000 V/1 V
Input voltage range	0 to 10–V DC or AC peak	Drift with time	<50 ppm/h
DC voltage gain accuracy	<0.1% of full scale	Slew rate	800 V/ μ s
Drift with temperature	<100 ppm/ $^{\circ}$ C	Signal bandwidth	DC to 5.2 kHz

6.5 Experimental Tests

The experimental tests are divided in three empirical test procedures including sinc-response (SR) test, Single Frequency (SF) test and Distorted Waveform (DW) test. SR test is the main test to extract the LPVT model by acquiring its transfer function. By using the transfer function, it is possible to predict the LPVT output for any inputs with frequency components up to 2.5 kHz. The prediction of the output is done by convolution between the acquired transfer function and the input signal in time domain.

The SF and DW tests are simply used for validation of the SR test and of the output prediction. The ratio error and phase displacement are then used as tools to validate the proposed approach.

6.5.1 SR Test Procedure

To perform the SR test, the designed sinc signal with $a = 50$ is supplied to the Agilent 33250A signal generator. The signal generator output is amplified using Trek Voltage amplifier with repetition frequency of $f_o = 50$ Hz. The amplified signal (16 kV) is applied to the LPVT under test as the primary voltage.

Afterwards, the ratio error ε and the phase displacement $\Delta\varphi$ are computed as:

$$\varepsilon = \frac{K|\vec{v}_2| - |\vec{v}_1|}{|\vec{v}_1|} 100 \quad (6-11)$$

$$\Delta\varphi = \angle\vec{v}_2 - \angle\vec{v}_1 \quad (6-12)$$

in which \vec{v}_2 and \vec{v}_1 are the secondary and primary voltage phasors, respectively. \vec{v}_2 is measured directly from the LPVT output and \vec{v}_1 is measured using a resistive–capacitive reference voltage divider, which was characterized in a range of frequency that includes the power quality one.

Once both primary and secondary quantities are acquired, the DFT is applied and then ε and $\Delta\varphi$ are calculated for each frequency component from 50 Hz to 2.5 kHz with frequency step of $f_o = 50$ Hz. Moreover, the frequency spectrum is saved for analytical operation to extract the transfer function and output prediction.

6.5.2 SF Test Procedure

The SF test is done using the same test setup as SR test, but with rated voltage pure sinusoidal waveforms with frequencies 50 Hz, 500 Hz and 1 kHz. For each frequency, ε and $\Delta\varphi$ are calculated to be compared with those computed after the estimation process. The SF test is limited to 1 kHz due to amplifier power limitation under the rated voltage; however, the LPVT linearity guarantees that if the method is effective up to 1 kHz, it will be effective even at 2.5 kHz.

6.5.3 DW Test Procedure

The distorted waveform test is another test for validation of the SR test and the results of the output prediction like SF test, except that in the DW test the fundamental harmonic at 50 Hz is superimposed to 3rd, 5th and 7th harmonics to simulate a distorted waveform in the power network. The amplitude of fundamental harmonic is set to the rated voltage, while the 3rd, 5th and 7th harmonics are set to the 10% of the rated voltage. Overall, 4 tests were performed: (i) three tests in which the 50 Hz component is applied when one of the three harmonics is superimposed; (ii) one test in which the three harmonics are superimposed at the same time to the 50 Hz. During these tests, ε and $\Delta\varphi$ are calculated for each frequency components using DFT analysis to be compared with the one from output prediction.

The DW test is included in the method validation procedure because LPVTs experience distorted voltages during their actual operation. Therefore, a method capable of estimating the LPVTs behavior even in distorted (hence more actual) conditions is more desirable than methods which simply works at rated conditions. As it is demonstrated in the next sections, the proposed approach is fully effective and applicable in all distorted conditions.

6.5.4 Output Prediction and Validation

The purpose is to predict the output of the LPVT using its sampled data transfer function in simulation. Finally, the predicted outputs are validated by the experimental test. Furthermore, the SR test is validated by SF and DW tests.

First, the transfer function is calculated using the SR test results. During the SR test, the DFT of the input sinc (IS) signal and sinc-response which are row vectors of complex numbers with the length of $N = 10,000$ samples, are saved in polar coordinate. Using:

$$H(j\omega) = \frac{FFT(SR)}{FFT(IS)} = \frac{|FFT(SR)|}{|FFT(IS)|} (\angle FFT(SR) - \angle FFT(IS)) \quad (6-13)$$

the frequency domain transfer function ($H(j\omega)$) is calculated for the LPVT. Writing (6-13) in polar coordinates is useful to interpret Equation (6-13) as ε and $\Delta\varphi$ ($\|$ and \angle for the amplitude and phase, respectively). It is necessary to consider that the LPVT needs to have zero initial condition for the tests, and we are interested only in the steady state response of the LPVT. The calculated $H(j\omega)$ is a vector of complex numbers with length $N = 10,000$ Sa.

By applying the inverse DFT, the time domain transfer function ($h(t)$) is found as a row vector of real numbers and with the length of N . Afterwards, it is possible to apply the convolution

$$\mathcal{F}\{h(t) * x(t)\} = \mathcal{F}\{h(t)\} \cdot \mathcal{F}\{x(t)\} \quad (6-14)$$

to $h(t)$ with any other LPVT input signal ($x(t)$) to predict the device output. The convolution theorem is the main motivation to use (6-13) to extract the transfer function and for this reason, the $h(t)$ is referred as the model of LPVT to be validated by SR experimental test.

It is important to mention that the computed convolution is valid if and only if the generic input signal $x(t)$ has a frequency content limited to 2.5 kHz. The reason is obvious when considering the synthesized sinc signal which has a bandwidth limited to 2.5 kHz.

6.5.4.1 Filtered Transfer Function

The purpose of this paragraph is to explain the removal of the noise frequency components higher than 2.5 kHz from the adopted signals. To shine some light on the topic, Figure 6-5 is considered as the amplitude of the DFT for both IS signal and SR signal ($|FFT|$). To use Equation (6-13) for calculating the frequency domain transfer function ($H(j\omega)$), the quotient between DFT of IS signal and SR signal showed in Figure 6-5 is computed. In Equation (6-13), $|FFT(SR)|$ is the primary voltage measured by LPVT and $|FFT(IS)|$ is the reference primary voltage measured by reference voltage divider. To calculate $\frac{|FFT(SR)|}{|FFT(IS)|}$, the two rectangular windows in Figure 6-5 are divided to each other. For frequencies

higher than 2.5 kHz (sample numbers higher than 50) two small numbers c_i and c_o are divided to each other, while for the frequencies below 2.5 kHz (sample numbers from 1 to 50) high values of b_i and b_o (≈ 160 V) in rectangle width are divided to each other. The division of two small values (c_i and c_o) turned out to be about 1 like the division of two high values in rectangle width is ($b_o/b_i \approx c_o/c_i \approx 1$).

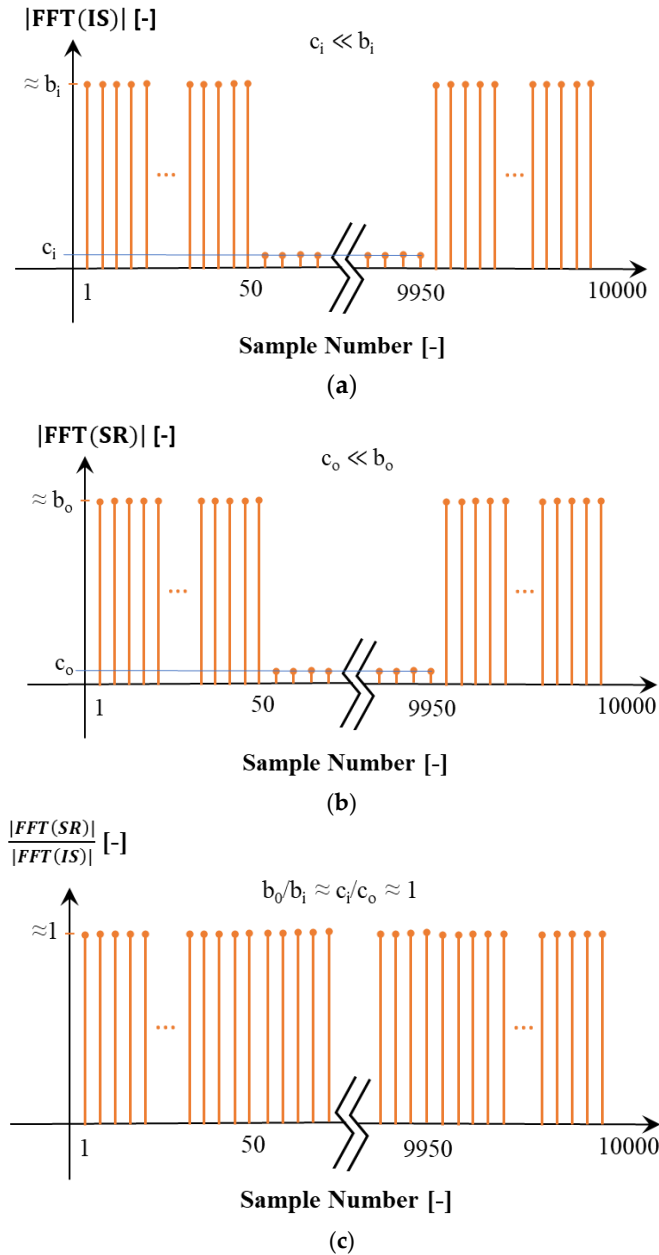


Figure 6-5. (a) DFT magnitude of the input sinc signal; (b) DFT magnitude of the sinc-response signal; (c) ratio between DFT magnitude of input sinc and sinc-response signal

One can interpret this flat profile in all the frequency rang as a normalized impulse-response related to the ratio error of the LPVT in all frequencies. The approach to remove the effect of the ratio error in high frequencies is to consider zero ratio error (fixing $\frac{|FFT(SR)|}{|FFT(IS)|} = 1$) and zero phase displacement ($\angle FFT(SR) - \angle FFT(IS) = 0$) for frequencies higher than 2.5 kHz. The two filtered and unfiltered versions of $h(t)$ represent the same values for frequencies below 2.5 kHz. In what follows only the filtered version is used.

6.6 Results

6.6.1 SR Experimental Test Results

The primary IS signal was applied to the LPVT under test as the primary signal and the output signal (SR signal) multiplied by the rated transformation ratio was the measured primary voltage. Figure 6-6 shows both IS and SR signals in time domain. Using the DFT of both IS and SR signals, it was possible to calculate ε and $\Delta\varphi$ for all frequency components from 50 Hz to 2.5 kHz with steps of 50 Hz. For the sake of clarity and of comparison in what follows, for some frequencies ε and $\Delta\varphi$ are listed in Table 6-2. The values in the table are the mean of 500 computations; furthermore, the values are given with their standard deviation of the mean σ_m . From the table it is possible to conclude that for the ratio error the passive LPVT under test was properly operating within the limits of its accuracy class (0.5). For the phase error as declared in section 6.1, it must be compensated applying the proper correction factor introduced by manufacturer. This is due to the fact that in passive LPVTs there are no electronic circuit to compensate the errors. It is worth clarifying that the DC offset observable in Figure 6-6 is mainly due to the instrumentation adopted for acquiring the primary and the secondary quantities. However, it was not significant in the experimental resulted as it was confirmed by the resulted in Table 6-2.

Table 6-2. Experimental SR test results in terms of ε and $\Delta\varphi$.

f (Hz)	ε (%)		$\Delta\varphi$ (rad)	
	Mean Value	σ_m	Mean Value	σ_m
50	0.015	0.02	0.0647	0.0001
150 (3rd harmonic)	0.28	0.01	0.0187	0.0001
250 (5th harmonic)	0.246	0.009	0.00947	0.00009
350 (7th harmonic)	0.212	0.008	0.00548	0.00008
500	0.166	0.008	0.00244	0.00008
1000	0.069	0.007	-0.00115	0.00007

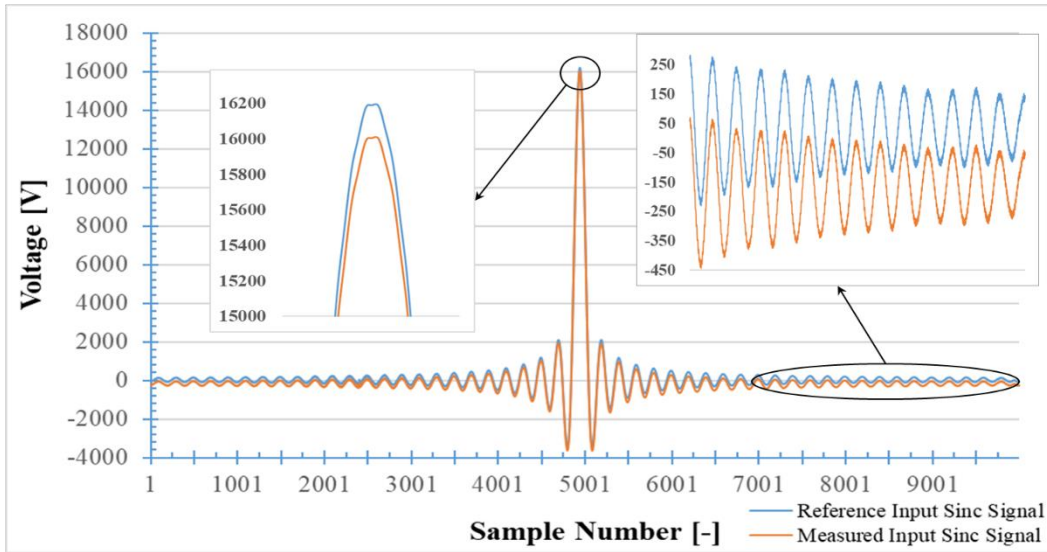


Figure 6-6. Reference input sinc signal applied to the LPVT under test, measured by reference resistive–capacitive voltage divider and the input sinc signal measured by the LPVT under test (LPVT sinc-response transferred to the primary side)

Corresponding to Table 6-2, Figure 6-7 and Figure 6-8 represent the graph diagram of all 50 calculated ratio and phase errors, respectively from 50 Hz to 2.5 kHz with steps of 50 Hz.

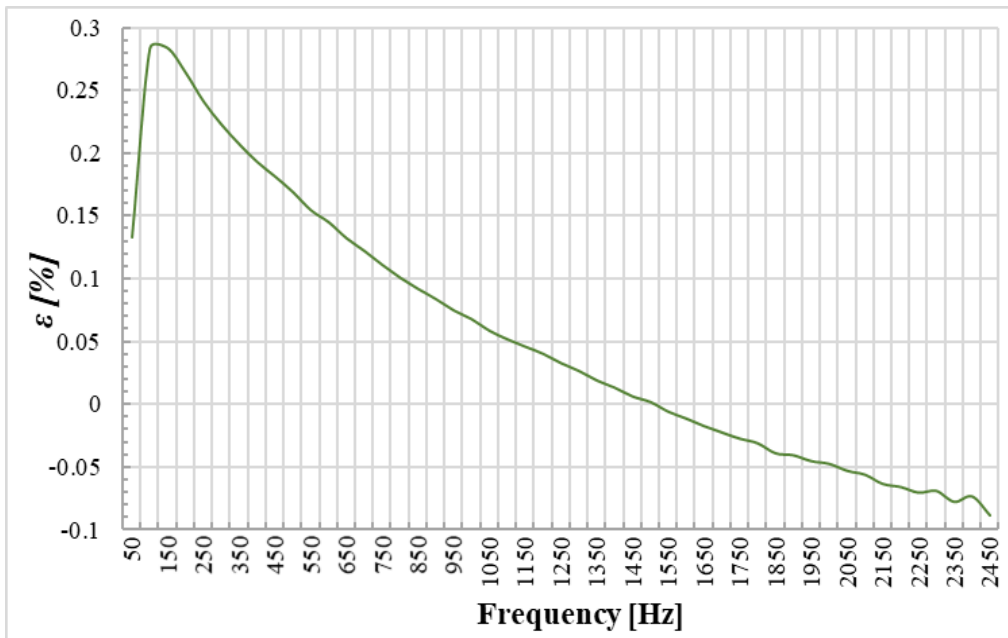


Figure 6-7. Ratio Error trend vs. frequency

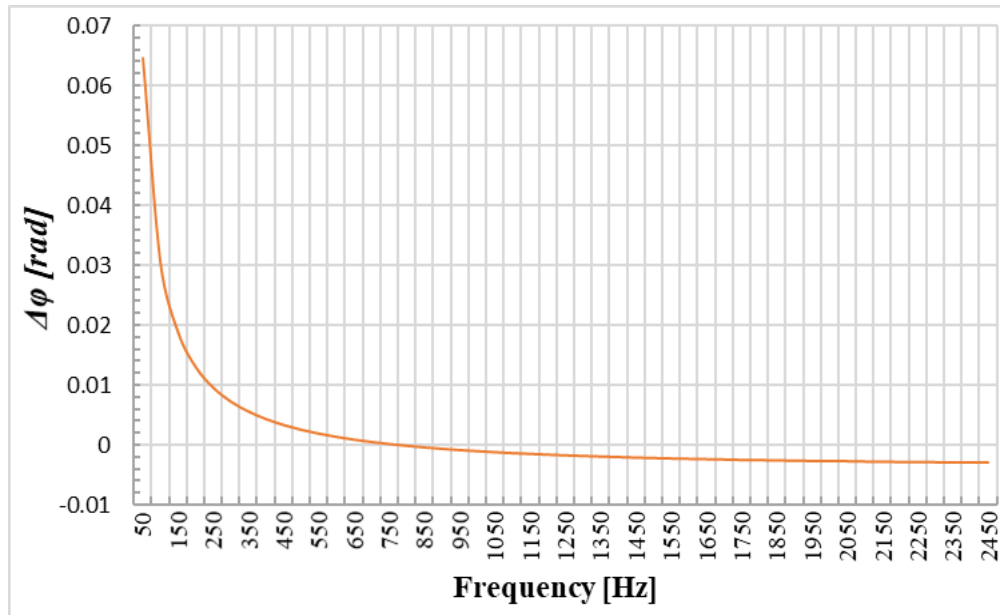
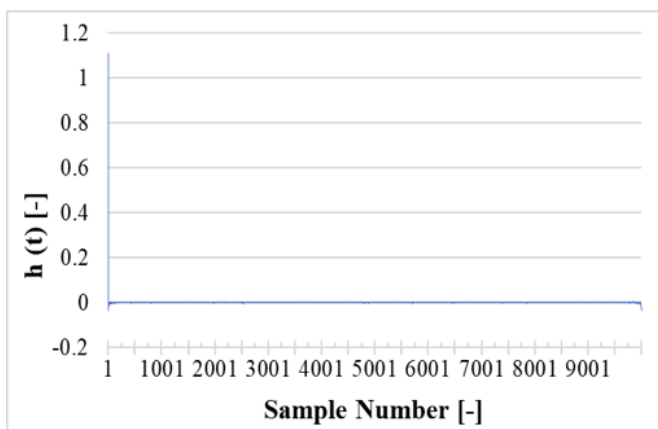


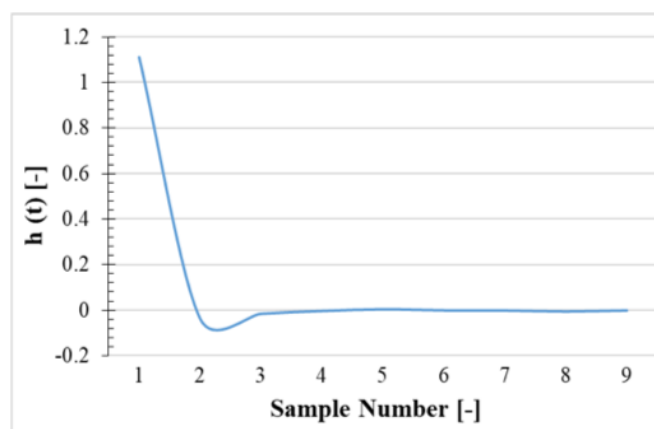
Figure 6-8. Phase Displacement trend vs. frequency

6.6.2 Transfer Functions

The time domain transfer function ($h(t)$) calculated by performing the inverse DFT on $H(j\omega)$ in Equation (6-13), is divided in two filtered and unfiltered versions. The results of the filtered version are graphed in Figure 6-9, while those of the unfiltered ones are plotted in Figure 6-10. In both cases and figures, 4 zoomed parts of the graphs can be distinguished.



(a)



(b)

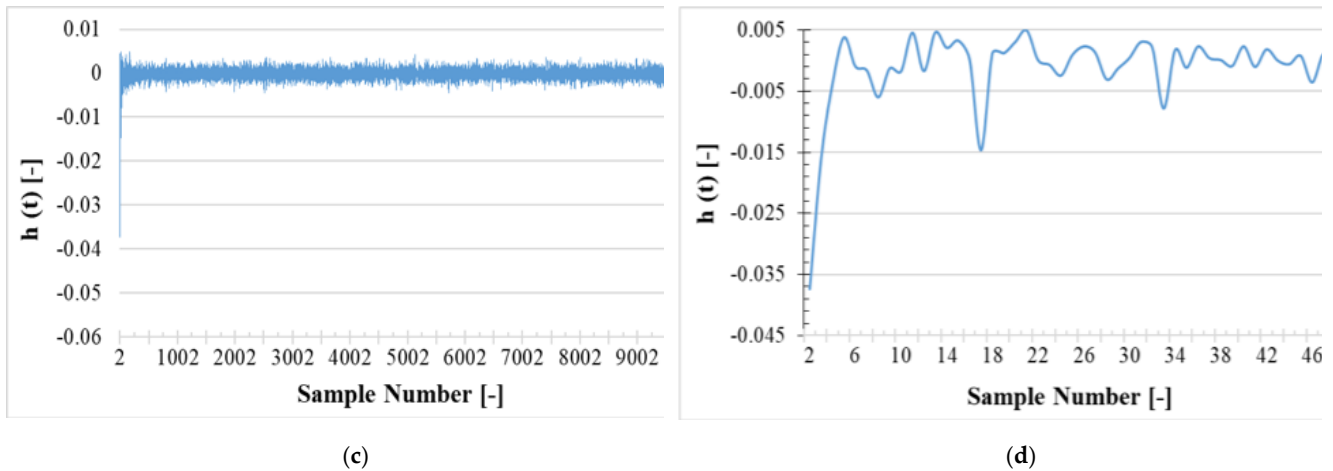
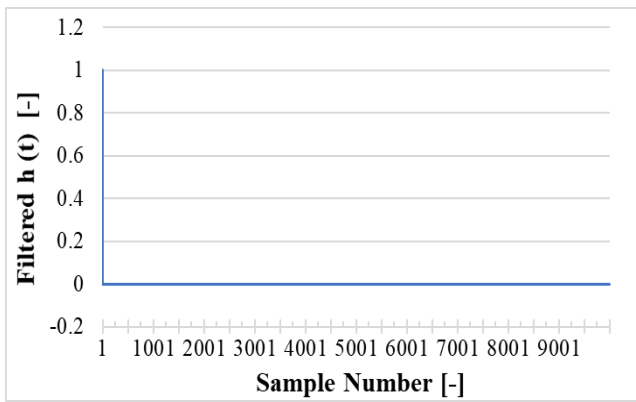


Figure 6-9. Time domain unfiltered version of The LPVT sampled data transfer function. (a) all 10,000 samples; (b) first 9 samples; (c) only the first sample removed; (d) samples from the 2nd to the 50th

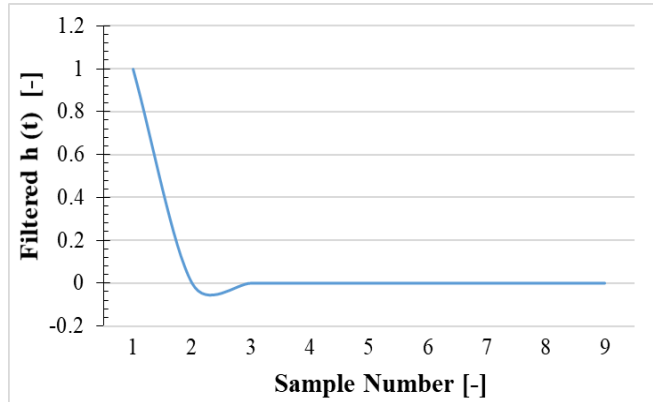
This is mainly due to (i) the high number of samples and (ii) to the sharp variations of the transfer function in the time domain. In both Figure 6-9 and Figure 6-10, the fast reduction of $h(t)$ magnitude from first sample to the second sample is clear. This is a typical impulse-response for a Linear Time Invariant (LTI) system. The reason for the fast decreasing of $h(t)$ magnitude is the slightly frequency dependence feature of the LPVT under test.

Let us consider a frequency independent system impulse-response which is another impulse signal in the system output. In this case the system transfer function amplitude in frequency domain ($|H(j\omega)|$) will be a fixed gain and in the time domain, $h(t)$ represents an impulse. This behavior is clearly seen in Figures 6-9 (b) and 6-10 (b).

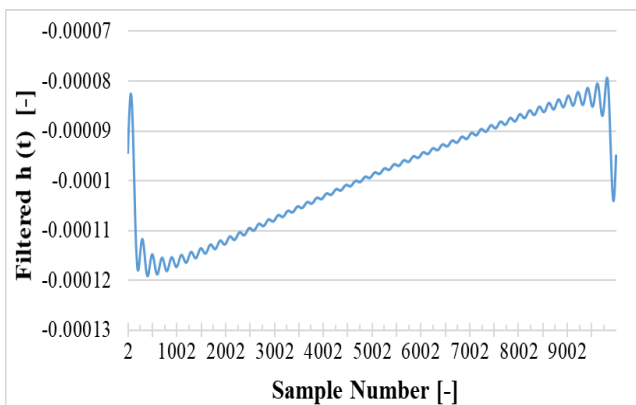
Discarding the fast reduction in $h(t)$ magnitude, it can be seen in Figures 6-9 (c) and 6-10 (c) that the variation from second sample to the end is much smaller than the fast drop of the $h(t)$ magnitude from the first to the second sample. To magnify the variation of the $h(t)$ magnitude from the 2nd sample to the 50th sample, Figures 6-9 (d) and 6-10 (d) are presented.



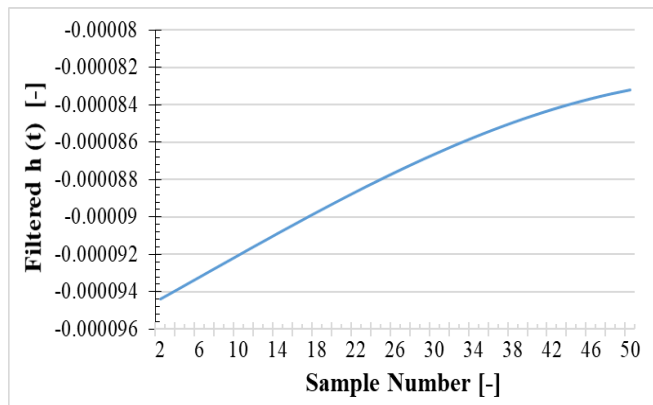
(a)



(b)



(c)



(d)

Figure 6-10. Time domain filtered version of the LPVT sampled data transfer function. (a) all 10,000 samples; (b) first 9 samples; (c) only the first sample removed; (d) samples from the 2nd to the 50th

Figure 6-10 features a smooth profile due to the filtering action on ε and $\Delta\varphi$ for samples number higher than 50 (corresponding to frequencies higher than 2.5 kHz). The filtering action refers to the ε and $\Delta\varphi$ set to zero for frequencies higher than 2.5 kHz. Moreover, the filtering action in Figure 6-10 has reduced the variation of $h(t)$ magnitude compared to Figure 6-9.

6.6.3 SF Experimental Test Results

Table 6-3 shows ε and $\Delta\varphi$ results for SF test under 50 Hz, 500 Hz and 1 kHz at rated voltage ($20/\sqrt{3}$ kV). The table contains the mean value and standard deviation of 500 ε and $\Delta\varphi$ measurements. From the table, it is evident that the obtained ε and $\Delta\varphi$ values confirm those listed in Table 6-2, which are computed by using the SR test (variations below 10 %). In other words, this first test confirms the applicability of the simple SR test.

Table 6-3. Experimental SF test results

f (Hz)	ε (%)		$\Delta\phi$ (rad)	
	Mean Value	σ_m	Mean Value	σ_m
50	0.1435	0.0002	0.064691	0.000002
500	0.1638	0.0002	0.002444	0.000002
1000	0.0761	0.0002	-0.001190	0.000002

6.6.4 DW Experimental Test Results

The DW test is performed using the same test setup and a distorted waveform as primary voltage. This set of tests contains 4 different tests with different composition of the harmonics superposed to the fundamental harmonic (50 Hz). ε and $\Delta\phi$ results for each frequency component are reported in Table 6-4.

Table 6-4. Experimental DW test results.

Test	Component	ε (%)		$\Delta\phi$ (rad)	
		Mean Value	σ_m	Mean Value	σ_m
50 Hz + 3rd	50 Hz	0.1475	0.0002	0.064736	0.000001
	150 Hz	0.3103	0.0008	0.018602	0.000008
50 Hz + 5th	50 Hz	0.1396	0.0001	0.064723	0.000001
	250 Hz	0.2692	0.0007	0.009485	0.000007
50 Hz + 7th	50 Hz	0.1406	0.0002	0.064721	0.000001
	350 Hz	0.2327	0.0006	0.005461	0.000006
50 Hz + all	50 Hz	0.1409	0.0001	0.064719	0.000001
	150 Hz	0.3083	0.0008	0.01857	0.00001
	250 Hz	0.2691	0.0008	0.009433	0.000007
	350 Hz	0.2302	0.0007	0.005462	0.000007

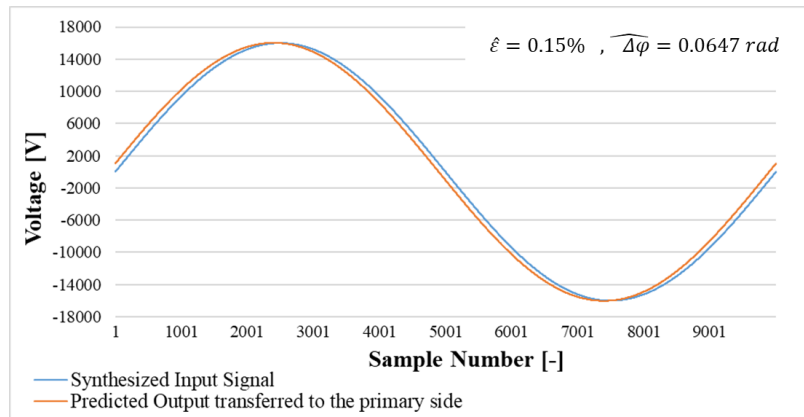
In all harmonic compositions, the amplitude of the fundamental harmonic is set to the rated value and the amplitude of the 3rd, 5th and 7th harmonics is set to 10% of the rated voltage. In all Cases 500 ε and $\Delta\phi$ are computed and mean values are reported in Table 6-4 along with the combined uncertainty. The results show that the LPVT under distorted condition still holds the accuracy class of 0.5 for the ratio error, and for the phase error it should be compensated by the introduced correction factor as explained before. Moreover, DW test results validate the results achieved from SR test reported in Table 6-2 for the same frequency composition. Such a validation is only preliminary and secondary; as a matter of fact, the DW test is aimed at validating the estimation approach presented in the next subsection.

6.6.5 Output Prediction and Validation

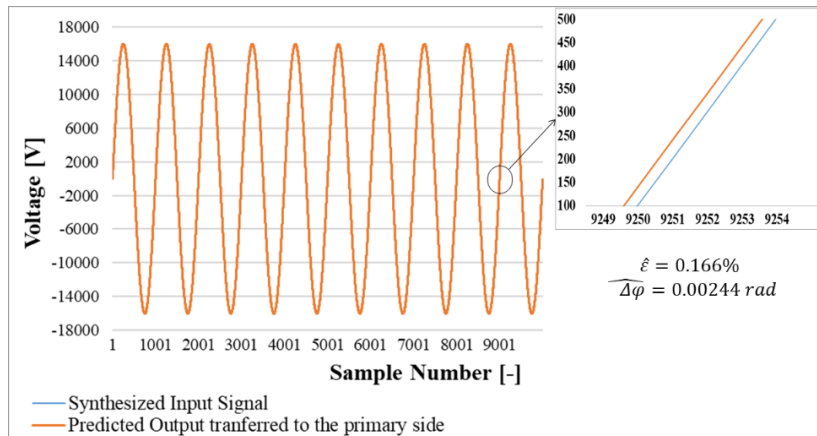
The output prediction is simulated in software environment by synthesizing the input signals, adopted for the SF and DW experimental tests and then convolute them with the calculated transfer function in time domain ($h(t)$). The purpose is to use the LPVT model Transfer function ($h(t)$) in software environment to predict the LPVT output signal, validating it by computing ε and $\Delta\varphi$ and comparing it with those obtained from the experimental results. The estimated ratio error and phase displacement are denoted with $\hat{\varepsilon}$ and $\widehat{\Delta\varphi}$.

6.6.5.1 SF Test Prediction

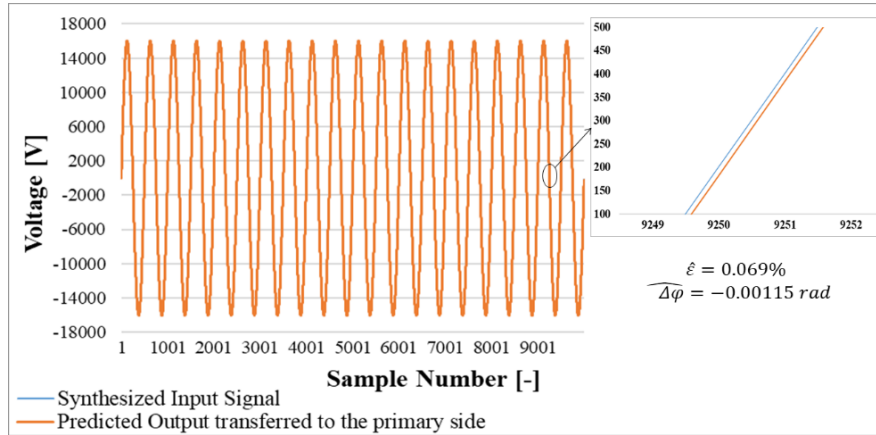
For each of the 3 frequencies (50 Hz, 500 Hz, and 1 kHz) a waveform was synthesized and convoluted with $h(t)$. Then, $\hat{\varepsilon}$ and $\widehat{\Delta\varphi}$ were computed in all cases. Figure 6-11 shows both synthesized input signals and predicted outputs along with the estimated $\hat{\varepsilon}$ and $\widehat{\Delta\varphi}$.



(a)



(b)



(c)

Figure 6-11. Synthesized sinusoidal input signal and the measured signal prediction by simulation. (a) prediction for 50 Hz; (b) prediction for 500 Hz; (c) prediction for 1 kHz.

For the sake of comparison, Table 6-5 reports both the $\hat{\varepsilon}$ and $\widehat{\Delta\varphi}$ estimated in this section and the ε and $\Delta\varphi$ obtained during the experimental SR tests. From table it can be appreciated the efficiency and validity of the estimation approach for both the ratio error and the phase displacement.

Table 6-5. SF Prediction results and comparison with SR experimental test results

f (Hz)	SR Experimental Test Results		SF Prediction Results by Simulation	
	ε (%)	$\Delta\varphi$ (rad)	$\hat{\varepsilon}$ (%)	$\widehat{\Delta\varphi}$ (rad)
50	0.15	0.0647	0.15	0.0647
500	0.166	0.00244	0.166	0.00244
1000	0.069	-0.00115	0.069	-0.00115

6.6.5.2 DW Test Prediction

For the distorted waveforms introduced in the DW tests, the estimation process described before was applied, obtaining another set of estimated $\hat{\varepsilon}$ and $\widehat{\Delta\varphi}$. Figure 6-12 shows, for each synthesized distorted signal, the primary voltage and the estimated secondary one, scaled to the primary side. Starting from those waveforms, $\hat{\varepsilon}$ and $\widehat{\Delta\varphi}$ were computed (estimated) for each case and listed in Table 6-6. Table must be compared with Table 6-4 (and also with Table 6-2) to appreciate the obtained estimates. Note that the

estimated and experimental values are almost identical and confirm, even in the case of distorted waveforms, the efficiency and applicability of the estimation approach.

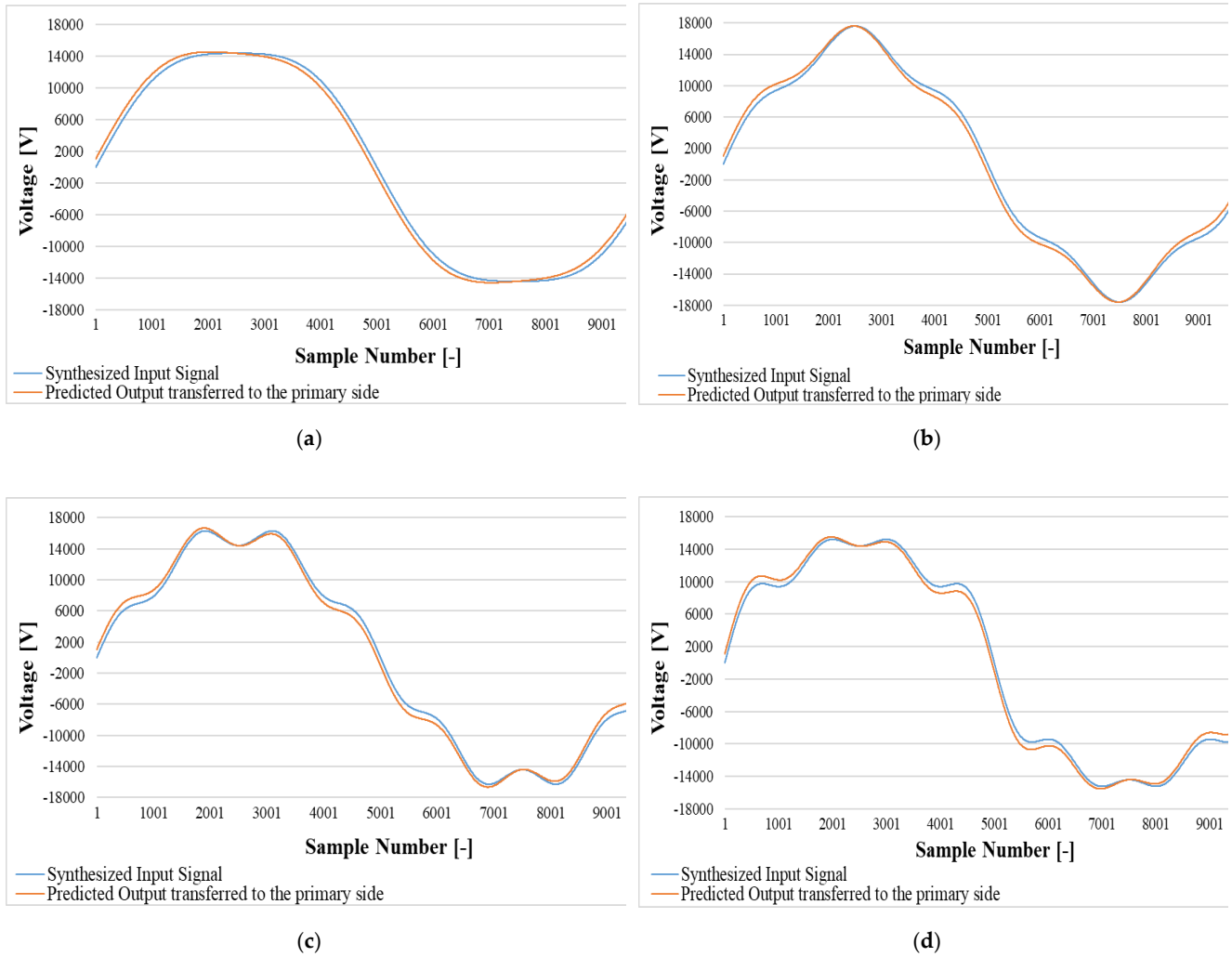


Figure 6-12. Synthesized distorted input signal and the measured signal prediction by simulation. (a) prediction for 1st + 3rd harmonics; (b) prediction for 1st + 5th harmonics; (c) prediction for 1st + 7th harmonics; (d) prediction for 1st + 3rd + 5th + 7th harmonics.

Table 6-6. DW prediction results.

Test	Component	$\hat{\varepsilon}$ (%)	$\widehat{\Delta\varphi}$ (rad)
50 Hz + 3rd	50 Hz	0.15	0.0647
	150 Hz	0.28	0.0187
50 Hz + 5th	50 Hz	0.15	0.0647
	250 Hz	0.246	0.00947
50 Hz + 7th	50 Hz	0.15	0.0647
	350 Hz	0.212	0.00548
50 Hz + all	50 Hz	0.15	0.0647
	150 Hz	0.28	0.0187
	250 Hz	0.246	0.00947
	350 Hz	0.212	0.00548

As a final comment, it is worth summarizing the main achievements of this work:

- The SR approach was validated with typical tests methods like SF and DW. By means of ε and $\Delta\varphi$ it was demonstrated the high accuracy and validity of the proposed SR test;
- The SR test combined with the mathematical convolution were implemented to estimate the output of the LPVT under test plus its two main accuracy indices: $\hat{\varepsilon}$ and $\widehat{\Delta\varphi}$;
- All experimental tests were compared with the associated estimated ones demonstrating that, in all cases, the proposed approach provides very accurate results.

6.7 Conclusion

The study, after presenting related theoretical aspects, describes the experimental setup and tests performed on a low-power voltage transformer. The sinc-response is used to obtain a transfer function, hence a model of the device, which allows the estimation of the transformer output in whatever operating condition. Such an approach was validated comparing experimental measurements and estimations at: (i) rated conditions, (ii) frequencies different from the rated, (iii) distorted conditions. What was demonstrated with the results is that the developed approach is effective and applicable in all abovementioned operating conditions. Therefore, what proposed here can become a useful and powerful tool to improve the characterization of voltage transformers and to be implemented inside simulation software used by distributed system operators, utilities, and academic bodies. [83], and [84] are the publications resulting this section research work.

7 Conclusions

In the present thesis as the result of a 3-years research work, new measurement models and procedures are designed and implemented for instrument transformer characterization and modeling, and for power networks component diagnosis in particular MV cable joints. The purpose is to solve the challenges in power systems from the metrology point of view. As the core of the thesis 3 different topics are presented in detail as following:

The measurement setup for Tan Delta measurement test setup is designed and implemented for MV cable joints diagnosis. The designed test setup is used for Tan Delta variation vs. temperatures in cable joints. On the other hand, to find out the effect of mechanical pressure, the same setup is used to measure Tan Delta vs. mechanical pressure. as the final step, the interfacial pressure has been linked with temperature and a test setup is characterized to measure interfacial pressure vs. temperature.

The second work concerns a measurement model for inductive current transformers and core parameters extraction using open circuit and short circuit test. To do this, open circuit test and short circuit test which are adopted for power transformers, are adapted to the current transformers. After extracting the core parameters, their variation vs. temperature has been linked to the ratio and phase error variation vs. temperature. Moreover, the ratio and phase errors are decomposed to analyze the effect of temperature only on the RL filter composed of measured the core parameters. This helps to calculate the systematic contribution to uncertainty which can be compensated in real time based on the temperature and loading condition. Finally, by extracting a set of dynamic correction factors, the ratio and phase error has been predicted under different currents and temperatures. This approach can be used to build a portable standard unit for online metrological confirmation of deployed current transformers.

As the last research work reported in present thesis, an approach is invented for frequency characterization of dynamic systems up to a limited frequency range. The approach is called sinc response approach in correspondence to impulse response approach. In this test method a sinc signal is used instead of an impulse signal. As the sinc signal is measurable using conventional data acquisition systems, it has been shown that the frequency component of a 16.3 kV sinc signal implies the same ratio and phase error as the sweep frequency test does. For the frequency modeling, a test setup is designed and implemented to apply the input sinc signal and measure the output signal for further analysis. Used the measure signals,

a transfer function is extracted as the LPVT model which can predict the output using the convolution theorem.

For each research works, multiple papers are published which are referenced at the end of each subsection.

8 References

- [1] J. T. R. N. a. M. Z. A. Phadke, "Recent developments in state estimation with phasor measurements," in *Power Systems Conference and Exposition*, Seattle, WA, USA, 2009.
- [2] A. S. B. a. S. A. R. P. N. G. Bretas, "Masked errors in power systems state estimation and measurement gross errors detection and identification," in *PowerTech*, Trondheim, Norway, 2011.
- [3] M. P. P. A. P. a. S. S. C. Muscas, "Uncertainty of Voltage Profile in PMU-Based Distribution System State Estimation," *Transactions on Instrumentation and Measurement*, vol. 65, no. 5, pp. 988-998, 2015.
- [4] IEC-61869-2, "Instrument transformers - Part 2: Additional requirements for current transformers," in *International Electrotechnical Commission*, Geneva, Switzerland, 2012.
- [5] IEC-61869-3, "INSTRUMENT TRANSFORMERS – Part 3: Additional requirements for inductive voltage transformers," in *International Electrotechnical Commission*, Geneva, Switzerland, 2011.
- [6] VIM, "International Vocabulary of Metrology," in *BIPM- Available at: <https://jcgm.bipm.org/vim/en/index.html>*, Last update 2017.
- [7] A. F. a. D. Petri, "MEASUREMENT MODELS AND UNCERTAINTY," in *Modern Measurements, Fundamentals and Applications*, IEEE Press, 2015, pp. 3-6.
- [8] GUM, "Evaluation of measurement data – Guide to the expression of uncertainty in measurement-JCGM 100:2008 (GUM 1995 with minor corrections)," in *BPIM- available at <https://www.bipm.org/en/publications/guides/gum.html>*.
- [9] A. K. A. S. V. E. P. L. L. G. E. G. D. Evagorou, "Setup and preliminary results of a pilot on-line cable PD monitoring system on an 11 kV switchboard using capacitive couplers," in *7th Mediterranean Conference and Exhibition on Power Generation, Transmission, Distribution and Energy Conversion (MedPower 2010)*, Agia Napa, Cyprus, 2010.
- [10] R. A. J. E. G. J. J. S. B. Q. F. P. F. D. V. P. Cichecki, "Statistical approach in power cables diagnostic data analysis," *IEEE Transaction on Dielectrics and Electrical Insulation*, vol. 15, pp. 1559-1569, 2008.
- [11] Y. G. J. B. G. M. Y. Z. W. Chang, "High frequency partial discharge measurement of straight power cable joint," in *IEEE Electrical insulation conference*, Baltimore, 2017.
- [12] B. H. S. H. B. L. G. W. T. Liu, "Experimental and simulation analysis of electrical breakdown for 220kV silicone rubber pre-moulded cable joints," in *13th International Electrical Insulation Conference, Birmingham*, Birmingham, UK, May 2017.
- [13] J. C. S. W. Y. J. T. L. Y. Z. X. Zhou, "Simulation of electric field around typical defects in 110kV XLPE power cable joints," in *International Conference on Circuits, Devices and Systems*, Chengdu, Sept 2017.
- [14] T. M. A. A. B. A. R. C. C. H. Shafi, "Extraction of cable joints tangent delta from bulk tangent delta measurement using HFAC method," in *International Conference on Power and Energy*, Melaka, Nov. 2016.

- [15] A. R. A. A. G. B. C. Chakrabarty, "Development of high frequency Tan Delta measurement method for 132kV transmission underground cables," in *IEEE 2nd International Symposium on Telecommunication Technologies*, Langkawi, Nov. 2014.
- [16] C. K. C. A. R. A. T. M. H. S. H. N. Permal, "Tangent delta extraction of cable joints for aged 11kV underground cable system," in *International Conference on Advances in Electrical and System Engineering*, Putrajaya, Nov. 2016.
- [17] A. G. M. J. T. Neier, "Identification of joints affected by water ingress in complex hybrid MV cable networks: 2 Field examples of combined VLF withstand testing, with Tan Delta (TD) and Partial Discharge (PD) diagnostics," in *International Conference on Condition Monitoring and Diagnosis*, Bali, Sept. 2012.
- [18] "Keysight Technologies, "Keyseight 3458A multimeter", datasheet, July 2014."
- [19] A. M. L. P. R. T. a. F. L. Abbas Ghaderi, "Test Setup Design, and Calibration for Tan Delta Measurements on MV Cable Joints," in *9TH IEEE INTERNATIONAL WORKSHOP ON APPLIED MEASUREMENTS FOR POWER SYSTEMS*, Bologna, 2018.
- [20] L. P. R. T. F. M. I. G. A. Mingotti, "Assessment of Metrological Characteristics of Calibration Systems for Accuracy vs. Temperature Verification of Voltage Transformers," in *IEEE workshop on Applied Measurements for Power Systems*, Liverpool, UK, Sept. 2017.
- [21] L. P. R. T. G. P. A. Mingotti, "Effect of Temperature on the Accuracy of Inductive Current Transformers," in *International Instrumentation and Measurement Technology Conference-I2MTC*, Houston, TX, USA, 2018.
- [22] N. S. M. C. X. W. Y. Qin, "Impacts on the distribution of electric-field in HVDC cable joint," in *IEEE International Conference on the Properties and Applications of Dielectric Materials*, Sydney, 2015.
- [23] W. H. S. Lin, "Theoretical research on temperature field of power cable joint with FEM," in *International Conference on System Science and Engineering*, Dalian, 2012.
- [24] P. H. F. M. J. J. S. A. L. J. J. R. A. Jongen, "Influence of ambient temperature on the failure behavior of cable joints," in *Conference on elctrical Insulation and Dielectric Phenomena*, Vancouver, 2007.
- [25] A. M. F. L. L. P. a. R. T. Abbas Ghaderi, "Effects of Temperature on MV Cable Joints Tan Delta Measurements," *IEEE Transactions on Instrumentation and Measurement*, vol. 68, no. 10, pp. 3892 - 3898, 2019.
- [26] L. G. B. X. Du, "Effects of interfacial pressure on tracking failure at XLPE cable joint by analyzing discharge light distribution," in *IEEE International Conference on Solid Dielectrics*, Potsdam, 2010.
- [27] L. L. D. Fournier, "Effect of pressure and temperature on interfacial breakdown between two dielectric surfaces," in *Conference on Electrical Insulation and Dielectric Phenomena*, Victoria, 1992.
- [28] A. M. L. P. a. R. T. Abbas Ghaderi, "Effects of Mechanical Pressure on the Tangent Delta of MV Cable Joints," *IEEE Transactions on Instrumentation and Measurement*, vol. 68, no. 7, pp. 2656 - 2658, 2019.

- [29] M. M. G. M. L. P. R. T. A. Albertini, "Toward a BITE for Real-Time Life Estimation of Capacitors Subjected to Thermal Stress", *IEEE Transaction on Instrumentation and Measurements*, vol. 60, no. 5, pp. 1671 - 1684, 2011.
- [30] T. Bragatto, A. Cerretti, L. D'Orazio, F. Gatta, A. Geri and M. Maccioni, "Thermal Effects of Ground Faults on MV Joints and Cables," *Energies*, vol. 18, no. 12, p. 3496, 2019.
- [31] J. Ruan, Q. Zhan, L. Tang and K. Tang, "Real-Time Temperature Estimation of Three-347 Core Medium-Voltage Cable Joint Based on Support Vector Regression," *Energies*, vol. 11, no. 6, p. 1405, 2018.
- [32] D. Fournier and N. Amyot, "Diagnostic of overheating underground distribution cable joints," in *16th International Conference and Exhibition on Electricity Distribution, 2001. Part 1: Contributions. CIRED. (IEE Conf. Publ No. 482)*, Amsterdam, Netherlands, 2001.
- [33] P. T. J. Z. X. Xiang, "Application of Fiber Bragg Grating Sensor in Temperature Monitoring of Power Cable Joints," in *IEEE International Conference on Electronics, Communications and Control*, Ningbo, 2011.
- [34] H. X. M. Xianbo, "Design of on-line temperature monitoring system for power cable joints based on supercapacitor," in *IEEE International Conference on Industrial Informatics*, Beijing, 2012.
- [35] A. G. G. M. e. a. A. Mingotti, "Low-cost monitoring unit for MV cable joints diagnostics," in *IEEE International Workshop on Applied Measurements for Power Systems*, Bologna, 2018.
- [36] T. M. A. A. B. A. R. C. C. H. Shafi, "Extraction of cable joints tangent delta from bulk tangent delta measurement using HFAC method," in *IEEE International Conference on Power and*, Melaka, Malaysia, 2016.
- [37] Z. J. M. Song, "Calculation and simulation of mechanical pressure of XLPE-SR surface in cable joints," in *International Conference on the Properties and Applications of Dielectric Materials*, Xi'an, May 2018.
- [38] R. D. S. A. M. L. P. R. T. A. Ghaderi, "Test bed characterization for the interfacial pressure vs. temperature measurements in MV cable joints," in *2019 II Workshop on Metrology for Industry 4.0 and IoT (MetroInd4.0&IoT)*, Naples, Italy, 2019.
- [39] J. Chen, Y. Dou, Z. Wang and G. Li, "A Novel Method for PD Feature Extraction of Power Cable with Renyi Entropy," *Entropy*, vol. 17, no. 11, pp. 7698-7712, 2015.
- [40] L. K. B. Rajalakshmi, "Analysis of partial discharge in underground cable joints," in *International onference on Innovation in Information, Embedded and Communication Systems*, Coimbatore, India, 2015.
- [41] W. Z. e. a. B. Sheng, "On-line PD detection and localization in cross-bonded HV cable systems," *IEEE Transaction on Dielectrics and Electrical Insulation*, vol. 21, no. 5, pp. 2217-2224, 2014.
- [42] E. D. N. Amyot, "A Study of Interfacial Pressure Behavior for Two Types of Thermally Cycled," in *International Symposium on Electrical Insulation*, Boston, USA, 2002.
- [43] L. Li, L. Zhong, K. Zhang, J. Gao and M. Xu, "Temperature Dependence of Mechanical, Electrical Properties and Crystal Structure of Polyethylene Blends for Cable Insulation," *Materials*, vol. 11, no. 10, p. 1922, 2018.

- [44] A. G. A. M. L. P. a. R. T. Raffaella Di Sante, "Effects of Thermal Cycles on Interfacial Pressure in MV Cable Joints," *Sensors*, vol. 20, no. 1, p. 169, 2020.
- [45] A. M. R. T. L. P. Abbas Ghaderi, " Analysis of MV Cable Joints Equivalent Impedance and its Variation vs. Temperature,," in *Proceedings of the 23rd IMEKO TC-4*, Xi'an, China, 2019.
- [46] IEC-61869-1, Instrument transformers - Part 1: General requirements, Geneva, Switzer: International Electrotechnical Commission, 2011.
- [47] G. K. S. M. K. Kumar, "new efficient algorithm to detect Current Transformer saturation," in *IEEE Power and Energy Society General Meeting*, Boston, 2016.
- [48] S. Z. H. I. H. D. G.S.S. Chau, "Experimental verification of the linear current transformer model," in *Australasian Universities Power Engineering Conference*, Sydney, 2008.
- [49] T. Ž. G. K. M. Dadić, "FIR modeling of voltage instrument transformers from frequency response data," in *First International Colloquium on Smart Grid Metrology*, Split, 2018.
- [50] M. F. A. P. M. R. O. C. C. M. G. P. M. F. Della Torre, "Instrument transformers: A different approach to their modelling," in *International Workshop on Applied Measurements for Power Systems*, Aachen, 2011.
- [51] D. K. Z. N. I. Paic, "A new approach to design and construction process of instrument transformers," in *The International Conference on Computer as a Tool*, Belgrade, 2005.
- [52] H. Y. L. P. C. F. G. S. Zhao, "Testing and modelling of voltage transformer for high order harmonic measurement," in *4th International Conference on Electric Utility Deregulation and Restructuring and Power Technologies*, Weihai, 2011.
- [53] V. S. A. Y. G. F. V. Lebedev, "“Modeling of measuring current and voltage transformers in dynamic modes,” in *International Conference on Mechanical Engineering, Automation and Control Systems*, Tomsk, 2014.
- [54] D. S. A. S. G. A. L. T. M. Brehm, "Modeling capacitive voltage transformers for distorted waveforms measurements," in *IEEE PES Transmission & Distribution Conference and Exposition-Latin America*, Morelia, 2016.
- [55] C. M. N. Locci, "Hysteresis and eddy currents compensation in current transformers," *IEEE Transactions on Power Delivery*, vol. 16, no. 2, pp. 154-159, 2001.
- [56] P. Daponte, "Electronically compensated current," *Measurement*, vol. 15, no. 4, pp. 213-222, 1995.
- [57] A. M. L. P. R. T. A. Ghaderi, "Inductive Current Transformer Core Parameters Behaviour vs. Temperature Under Different Working Conditions," in *Proceedings of the 23rd IMEKO TC-4*, Xi'an, Cina, 2019.
- [58] M. G. W. H. M. S. M. Sudhakar Ballal, "A Novel Approach for the Error Correction of CT in the Presence of Harmonic Distortion," *IEEE Transactions on Instrumentation and Measurement* , vol. 68, no. 10, pp. 4015 - 4027, 2018.
- [59] D. S. A. Santos, "Error Compensation Of Current Transformers Used In High Voltage Networks," *IEEE Latin America Transactions*, vol. 4, no. 3, pp. 165-169, 2006.

- [60] P. Sankaran and V. Murti, "Electronic error compensation of a current transformer," *Electronics Letters*, vol. 7, no. 12, pp. 327-328, 1971.
- [61] M. D. L. Eren, "Instrument transformer error compensation in Fourier based power metering," in *Proceedings of the 19th IEEE Instrumentation and Measurement Technology Conference*, Anchorage, USA, 2002.
- [62] V. C. G. C. e. a. A. Cataliotti, "Compensation of Nonlinearity of Voltage and Current Instrument Transformers," *IEEE Transactions on Instrumentation and Measurement*, vol. 68, no. 5, pp. 1322-1332, 2019.
- [63] G. Crotti, D. Gallo, D. Giordano, C. Landi and M. Luiso, "Non-conventional instrument current transformer test set for industrial applications," in *In Proceedings of the 2014 IEEE International Workshop on Applied*, Aachen, Germany, 2014.
- [64] H. Jiang, X. Yu and H. Wang, "Electronic current transformer test method research," *Applied Mechanics and Materiest method research*, Vols. 530-531, 2014.
- [65] J. Radek, P. Vaclav, D. Eddy and M. Stefaan, "Low-power voltage transformers for use with separable connectors n MV secondary gas-insulated switchgear: New challenge for standardization," *Cired Open Access Proc. J.*, p. 289–292, 2017.
- [66] P. Roccato, A. Sardi, G. Pasini, L. Peretto and R. Tinarelli, "Traceability of MV low power instrument transformer LPIT," in *In Proceedings of the 2013 IEEE International Workshop on Applied Measurements for Power Systems*, Aachen, Germany, 2013.
- [67] B. Kerr, L. Peretto, N. Uzelac and E. Scala, "Integration challenges of high-accuracy LPIT into MV recloser," *Cired-Open Access Proc. J.*, p. 260–263, 2017.
- [68] D. Crotti, C. Giordano and P. M. Cherbaucich, "Calibration of non-conventional instrument transformers," in *In Proceedings of the Conference on Precision Electromagnetic Measurements*, Washington, DC, USA, 2012.
- [69] W. Ren, Y. Yuan, X. Hu, Z. Yang and Y. Zhang, "Steady-state error calibration technology for electronic instrument transformer," in *In Proceedings of the 9th IET International Conference on Advances in Power System Control, Operation and Management (APSCOM 2012)*, Hong Kong, China, 2012.
- [70] A. Mingotti, L. Peretto, R. Tinarelli and A. Ghaderi, "Uncertainty Analysis of a Test Bed for Calibrating Voltage Transformers vs. Temperature," *Sensors*, p. 4472, 2019.
- [71] A. Mingotti, L. Peretto, R. Tinarelli and A. Ghaderi, "Uncertainty sources analysis of a calibration system for the accuracy vs. temperature verification of voltage transformers.," *J. Phys. Conf. Ser.*, p. 1065, 2018.
- [72] K. Draxler and R. Styblikova, "Calibrating an Instrument Voltage Transformer to achieve reduced uncertainty," in *In Proceedings of the IEEE Instrumentation and Measurement Technology Conference*, Singapore, 2009.

- [73] A. Cataliotti, V. Cosentino, G. Crotti, A. Delle Femine, D. Di Cara, D. Gallo, D. Giordano and C. Landi, "Compensation of Nonlinearity of Voltage and Current Instrument Transformers," *IEEE Trans. Instrum. Meas.*, vol. 68, no. 5, 2019.
- [74] Y. Yan, M. Chen, Y. Cheng, J. Kong, H. Ji and A. Song, "A Nanosecond High Voltage Impulse Protector for Small Signal Measurement Device," in *In Proceedings of the Second International Conference on Intelligent System Design and Engineering Application*, Sanya, China, 2012.
- [75] S. Shoichiro, N. Akira and H. Yoichi, "Dynamic impulse response model for nonlinear acoustic system and its application to acoustic echo canceller," in *In Proceedings of the 2012 Second International Conference on Intelligent System Design and Engineering Application*, New Paltz, NY, USA, 2009.
- [76] C. Buchhagen, M. Fischer, L. Hofmann and H. Däumling, "Metrological determination of the frequency response of inductive voltage transformers up to 20 kHz," in *In Proceedings of the IEEE Power & Energy Society General Meeting*, Vancouver, BC, Canada, 2013.
- [77] H. Seljeseth, E. Saethre, T. Ohnstad and I. Lien, "Voltage transformer frequency response. Measuring harmonics in Norwegian 300 kV and 132 kV power systems," in *In Proceedings of the 8th International Conference on Harmonics and Quality of Power*, Athens, Greece, 1998.
- [78] M. Klatt, J. Meyer, M. Elst and P. Schegner, "Frequency Responses of MV voltage transformers in the range of 50 Hz to 10 kHz," in *In Proceedings of the 14th International Conference on Harmonics and Quality of Power—ICHQP 2010*, Bergamo, Italy, 2010.
- [79] S. Zhao, H. Li, P. Crossley and F. Ghassemi, "Test and analysis of harmonic responses of high voltage instrument voltage transformers," in *In Proceedings of the 12th IET International Conference on Developments in Power System Protection (DPSP 2014)*, Copenhagen, Denmark, 2014.
- [80] M. Kaczmarek, D. Brodecki and R. Nowicz, "Analysis of operation of voltage transformers during interruptions and dips of primary voltage," in *In Proceedings of the 10th International Conference on Electrical Power Quality and Utilisation*, Lodz, Poland, 2009.
- [81] Y. Liu, F. Lin, Q. Zhang and H. Zhong, "Design and construction of a rogowski coil for measuring wide pulsed current," *IEEE Sens. J.*, vol. 11, p. 123–130, 2010.
- [82] I. 61869-6, Instrument Transformers-Part 6: Additional General Requirements for Low-Power Instrument Transformers, Swiss Standards: Winterthur, Switzerland: International Electrotechnical Commission, 2016.
- [83] G. A., M. A., P. L. and T. R., "Low-Power Voltage Transformer Smart Frequency Modeling and Output Prediction up to 2.5 kHz, Using Sinc-Response Approach," *SENSORS*, vol. 20, no. 17, p. 4889, 2020.
- [84] A. M. L. P. R. T. A. Ghaderi, "Fast Calibration Procedure for Low Power Voltage Transformers up to 2.5 kHz using Sinc response," in *24th IMEKO TC-4 international symposium*, Palermo, Italy, 2020.
- [85] P. H. P. M. J. Cardinaels, "Study of the Viscoelastic Behavior of Cold-shrinkable Joints for MV," in *IEEE Transmission and Distribution Conference*, New Orleans, 1999.